Semi-Automation in Image-guided Robotic Brain Surgery

Danying Hu

A dissertation
submitted in partial fulfillment of the
requirements for the degree of

Doctor of Philosophy

University of Washington

2017

Reading Committee:

Blake Hannaford, Chair

Howard J. Chizeck

Eric J. Seibel

Program Authorized to Offer Degree:
Electrical Engineering

University of Washington

Abstract

Semi-Automation in Image-guided Robotic Brain Surgery

Danying Hu

Chair of the Supervisory Committee:
Professor Blake Hannaford
Electrical Engineering

Surgical robots have been widely used to assist surgeons to carry out dexterous surgical procedures via various ways. Robotically assisted surgery allows surgeons to overcome the limitations in the minimally invasive surgery and thus to enhance the surgical performance. Most of the robotically assisted surgery require surgeon's operation directly or indirectly via a teleoperation station. A certain level of autonomy in robotic surgery could not only free the surgeon from some tedious and repetitive tasks, but also utilize the advantages of the robot: high dexterity and accuracy. This work considers the image-guided robotic neurosurgery, aiming to semi-automate a neurosurgical procedure for clean up the tumor residues after manual removal of the brain tumor using a surgical robot, where the manual operation is a tedious and time-consuming task for surgeons due to long time integration of the fluorescent signal. The entire medical procedure is modeled using behavior tree framework, and encoded and tested on RAVEN $^{\text{TM}}$ II surgical robotic platform using a simulated brain phantom. Furthermore, a path planner is developed that automatically synthesize different ablation path plans to cover the entire tumorous regions. At the current stage, the path planner is able to generate three types of path patterns for the surgeon to choose the most reliable plan before robotic execution. Along with the generated path plans, other computed metrics such as the total number of the via-points in each plan, estimated time for the robotic execution, will also be delivered to the surgeon for reference.

TABLE OF CONTENTS

LIST OF FIGURES

Figure Number Page

GLOSSARY

TUMOR ABLATION: is a surgical method to remove tumor tissue. Special probes are used to “burn” or “freeze” cancers.

TUMOR RESECTION: refers to the general surgical procedure of removing tumor tissue.

DEBULKING: is the reduction of as much of the bulk (volume) of a tumor as possible. It is usually achieved by surgical removal.

SURGICAL CAVITY: is a concave cavity that is exposed after the debulking of brain tumor, which can be up to a ping-pong ball size.

SURGICAL SITE: refers the part of the body where the surgery takes place. It also refers to the surgical cavity based on the context.

TUMOR RESIDUE / RESIDUAL TUMOR: refers the positive tumor margin that remains on the surface of the surgical cavity after surgical debulking. Tumor residues can be in any shapes and sizes.

CONTOUR: refers to the tumor boundary.

VIA-POINTS: refer to the intermediate points between the starting point and the destination in a resection path.

ACKNOWLEDGMENTS

Looking back over the past few years, I feel that I am fortunate enough to work with and learn from so many wonderful people, without whom my experience at the UW would never have been so enriching and rewarding.

First, I would like to thank my supervisor, Prof. Blake Hannaford, for his insightful guidance and invaluable advice in this research project and thesis completion. I am grateful for his patience, encouragement and academic freedom for allowing me to explore things of my interest. I wish to thank my major collaborator, Prof. Eric J. Seibel, who is like my second supervisor, for his active involvement, generous advice, inspiring guidance and encouragement throughout my research. I'm extremely lucky to have this research project, which was exactly what I want to explore when I came to the US. Thanks Eric for this great opportunity. I want to extend my gratitude to the committee members Prof. Howard J. Chizeck and Prof. Shan Liu for providing constructive comments and feedback about the thesis work and helping me keep sight of the big picture.

I am also fortunate to have the opportunities to work with many neurosurgeons and clinical scientists. I want to appreciate Prof. Dr. Laligam N. Sekhar and Prof. Dr. James M. Olson from the UW medical school, for providing insightful clinical advice and outline of the medical procedure in this research; Dr. Emily Girard at the Fred Hutchinson Cancer Research Center for preparing tissue samples for the research; Dr. Evgenii Belykh and Dr. Mark C. Preul from the Barrow Neurological Institute at St Josephs Hospital and Medical Center in Phoenix for the animal study of the tumor fluorescence imaging.

My appreciation also goes to my research collaborators Yuanzheng Gong and Yang Jiang at the Human Photonics Lab. Thanks for their devoted work in medical imaging. I want to thank engineer staff Richard S. Johnson for his detailed introduction and configuration of the SFE device.

All the members of the BioRobotics Laboratory are gratefully appreciated for creating such a joyful environment for both work and life. Particularly, I would like to thank Hawkeye King for his guidance and help with the RAVEN software, Sina Kosari for his help and advice when I first joined the group, Andrew Lewis for his help with the RAVEN hardware and Muneaki Miyasaka for his help in tool design and 3D printing.

Last but not least, I want to thank my mom and dad for their endless love and unconditional support. They are always the happiest people in the world for any of my accomplishments. I would like to thank Hao-Ming for always being supportive and encouraging me to follow my dreams. I also wish to thank my friends I've made throughout the graduate school for the support and friendship that I needed. The pursuit of Ph.D. has been a uniquely amazing and humbling experience, and I am very thankful to have it as a chapter of my life.

DEDICATION

to my beloved family.

Chapter 1

INTRODUCTION

Ever since the first documented robotic-assisted surgical procedure in 1985 [1], when an industrial robotic arm (PUMA 560) was used for neurosurgical biopsy, surgical robotics has been studied and developed for many medical applications by many research groups worldwide. In the last decade, new medical imaging and image-guidance technologies have been explored in combination with robotics to augment a variety of medical procedures by providing surgeons with accurate spatial information about the location and anatomical relationships of subsurface structures and instrument positions [2]. This integrated technology approach for medical imaging, image processing and segmentation, registration, tracking, and visualization, as well as human-robot interaction, offers potential benefits to both patients and physicians, and thus has been intensively studied and applied primarily in minimally invasive surgery. Clinical applications using image-guided robotic technology show enhanced dexterity and precision during the operation in the area of urology [3], orthopedics [4] and neurosurgery [5, 6], compared to the traditional open or laparoscopic surgery, although improved outcome of the robotic surgery has yet to be proven.

In the past few years, the development of molecular imaging technologies has greatly increased the visual information available to the surgeons during the operations. Near-infrared (NIR) fluorescence imaging has been shown feasible during cancer surgery (i.e. tumor ablation) using available imaging systems and contrast agents [7]. NIR fluorescence imaging makes the intraoperative tumor visualization and identification available to the surgeon, and therefore, has the potential to reduce the frequency of positive margins and the number of second surgeries [8].

1.1 Clinical Scenario

For patients with malignant gliomas, a safe maximal resection of the brain tumor is key to the higher survival rate. Clinical study of patients with glioblastoma showed significantly longer survival times for patients with 98% or more resection of tumor volume [9]. However, complete resection of the brain tumor at the margins is still a challenging task for surgeons due to the complex anatomic situations with high-risk structures in the cranial area and the lack of clear delineation between the tumor tissue and normal brain tissue. Therefore complete resection can only be achieved in a minority of patients. Fluorescence imaging techniques have shown great potential for improved surgical outcomes by providing surgeons intraoperative contrast-enhanced visualization of the tumor with modern contrast agents. One such agent, 5-aminolevulinic acid (5-ALA) has been assessed in many clinical studies [10, 11] but has limitations that the depth of imaging is reduced compared to NIR imaging, and the color rendering of the tissue reflectance image is distorted due to the absence of visible light within the fluorescence channel.

In the proposed clinical scenario, "Tumor Paint" [12] is considered for providing the molecular-specific imaging of brain tumors. "Tumor Paint" is a molecule derived from scorpion toxin, which is able to selectively bind to brain tumor cells and fluoresces in the NIR with the illumination of conjugated dye from red laser illumination as shown in Figure 1.1, or from NIR illumination in the BLZ-100 product [13]. The cancerous regions can be segmented in the NIR fluorescence image which is co-registered with reflectance full-color images. Because fluorescence responses of residual tumor cells remaining after the major debulking can be very weak, significant integration time may be required for a clear image segmentation. Due to this long integration time, manual treatment of the fluorescently labeled tumor residues is very tedious and nearly impossible. Thus, this procedure for tumor residue ablation is ideal for robotic automation with advanced multimodal laser-based imaging.

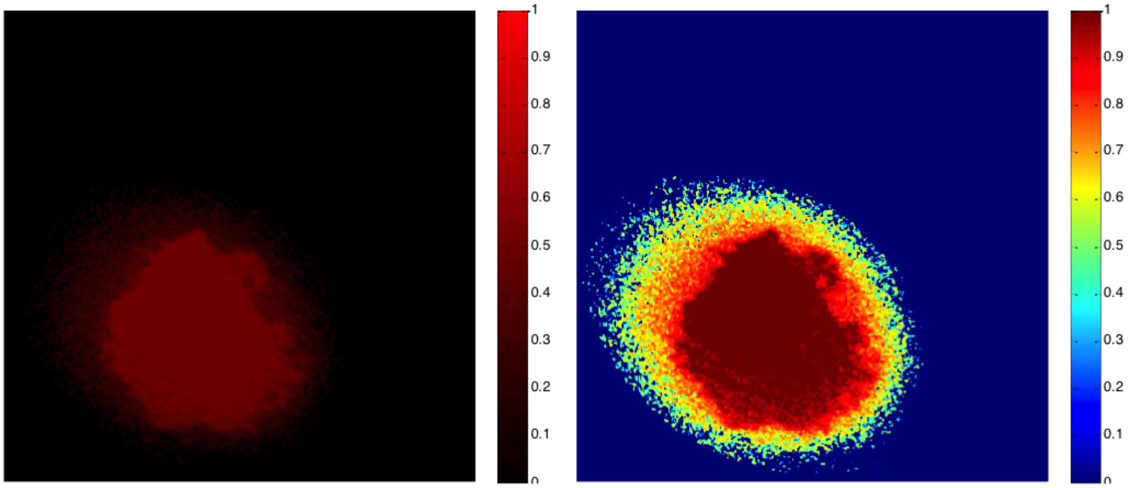

(a) (b)

Figure 1.1: Detection of mouse brain tumor injected with Tumor Paint in near-infrared fluorescence image captured by scanning fiber endoscope: (a) standard fluorescence image of a mouse brain. (b) post-processed image of the same mouse brain ex vivo.

1.2 Medical Robotic Problem Description

Based on the above clinical scenario, this thesis explores the feasibility for robotic automation of residual brain tumor ablation under surgeon's supervision. It is assumed that the bulk of the brain tumor will be removed through conventional surgery and a surgical cavity up to a ping-pong ball size will be exposed afterward. The goal is to automatically detect and clean up the tumor residues exposed and remaining on the wall of the surgical cavity using an intelligent robotic system, which is built with a RAVEN$^{\text{TM}}$ II surgical robot platform, a multi-modal Scanning Fiber Endoscope (SFE), a surgical suction tool and a stereo camera pair. The robotic system will first perform an initial scan of the surgical cavity to search for the fluorescence labeled tissues. A 3D model of the surgical cavity, labeled with the detected tumor residues, will be created from the scan. Then a motion planning module will automatically synthesize ablation plans based on the size and shape of the detected tumor residues. The surgeon will then authorize a subset of the plans for automatic ablation and visually monitor the progress.

1.3 Raven Surgical Robot

RAVEN^{TM} II (Figure 1.2) surgical robot is an open-source platform for medical robotics research [14]. RAVEN^{TM} II is a cable-driven mechanism and was originally designed as a robot for teleoperation, like the da Vinci® system. As medical robotics research explores increasing use of automation, limitations affecting positional precision, such as cable stretching and friction, mechanical backlash, and the imperfect kinematic model, which are not critical for teleoperation become significant obstacles for autonomous tasks. In the following sections, methods are discussed to mitigate these issues.

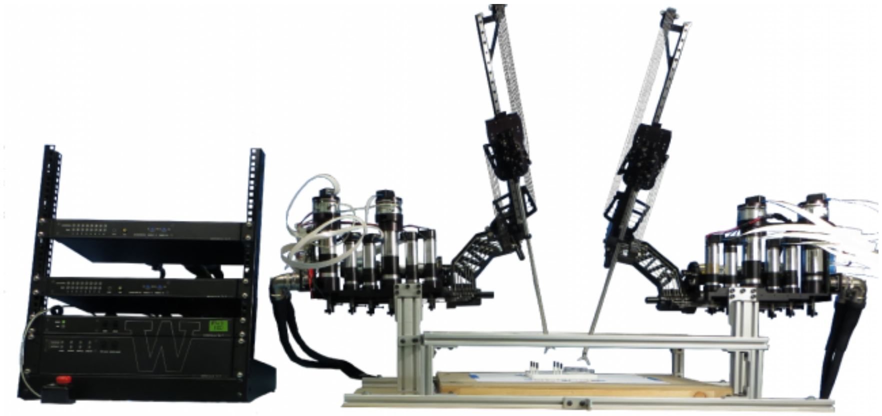

Figure 1.2: Overview of RAVEN^{TM} II surgical robotic system.

source: `http://applieddexterity.com/wp-content/uploads/2013/04/ravensys_lrg-644x320.png`

1.4 Medical Imaging System - Scanning Fiber Endoscope

Scanning Fiber Endoscope (SFE) [15] is a multimodal medical imaging system which is able to work in both reflectance and fluorescence video modes. The instrument consists of red-green-blue (RGB) laser illumination sources coupled into a single mode optic fiber that can be spiral scanned in 2D using a piezoelectric tube as an actuator (Figure 1.3). The small rigid tip (1.6 mm in diameter and 9 mm in length) on a highly flexible shaft allows unobtrusive optical guidance on small robotic end-effectors.

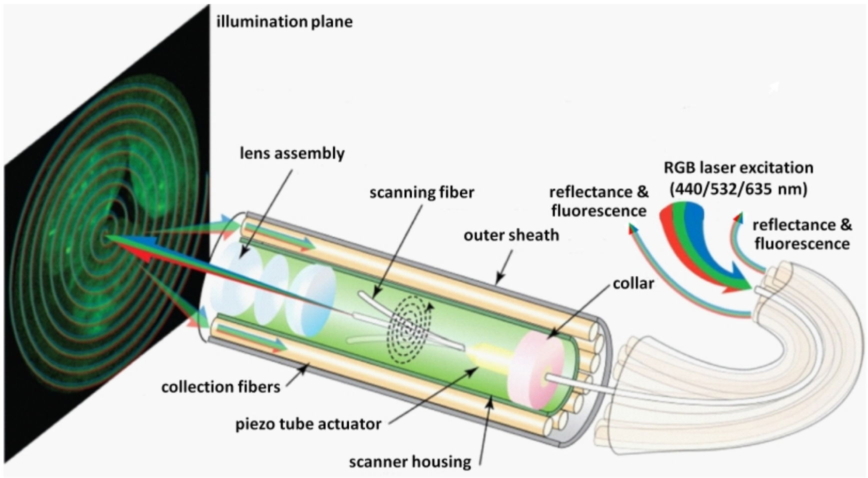

Figure 1.3: Schematics of the Scanning Fiber Endoscope.

source: `http://sitemaker.umich.edu/betrnet/files/schematic.jpg`

1.5 Technical Aspects and Research Aims

This work describes the bench-top implementation of the robotic automation of a neurosurgical procedure for clean-up the brain tumor residues under surgeon's supervision. The automated surgical procedure is divided into the following task sequence:

1. Collection of medical images: geometric scanning of the surgical cavity exposed after manual debulk

2. Medical image processing:

    - Specular reflection removal
    - 3D image reconstruction of the surgical cavity
    - Localization of the tumorous tissue inside the surgical cavity

3. Generation of one or more ablation plans
4. Plan selection by the surgeon
5. Plan execution by the surgical robot with vision feedback
6. Validation of the ablation outcome via SFE vision

These subtasks will be repeated until no cancerous tissue is detected in the last step. Algorithmic details of subtasks will be addressed in the following sections.

This thesis demonstrates the feasibility of modeling the ablation procedure using the Behavior Tree framework, creating a 3D model of the surgical cavity from a set of 2D reflectance and fluorescence SFE images, as well as the validity of a surgical coverage path planner based on the generated point-cloud of tumor residues. Furthermore, this work focuses on integrating an intelligent surgical robotic system on software and hardware levels, as well as development and validation of the algorithms for medical imaging and guidance of surgical instruments subject to medical procedure constraints and real-time endoscopy. This work aims to provide a pilot study of an integrated intelligent medical robotic system for semi-automation of a medical procedure in image-guided brain tumor ablation surgery with the following research aims.

Aim 1: Develop a framework for medical automation (Chapter 2)

Behavior tree is used to model the medical procedures and is implemented as the top-level of the control architecture for decision making and automatic coordination of each subtask with the surgeon in the loop. A new logic node (Recovery Node) is implemented to meet the requirements of this medical scenario.

Aim 2: Develop motion planning algorithms for image-guidance and robotic resection (Chapter 3 and Chapter 5)

Motion planning is highlighted in two key aspects of this research: 1) Guidance of the surgical instrument and imaging system to the target region and 2) generation and execution of the ablation plans in the target region. The first part addresses the motion planning and control of the vision system, which requires real-time feedback from the vision system and registers the robot pose with the vision frame. The second aspect focuses on trajectory planning of the surgical instrument based on detected tumor residues. Given the tumor segmentation map generated from 3D image reconstruction, the planner will synthesize paths which completely cover the segmented area subject to the following medical constraints:

- Complete removal of all labeled tissue. Minimize the removal of normal tissue.
- Imaging and planning must be repeated until no labeled material (cancerous tissue) is detected.
- Each residual tumor is assumed to be homeomorphic to a sphere (that is to have no holes) but is likely to have tendrils which will require specialized plans.
- A surgeon must have reliable control and choose the trusted plan for robotic treatment.

Aim 3: Integrate an interactive surgical robotic system of software, hardware, and SFE imaging (Chapter 4 and Chapter 5)

To achieve a fully intelligent surgical robotic system that is able to perform image-guided robotic surgery in an automated manner, system integration on both software level and hardware level are necessary. Mechanical parts are designed for assembling the imaging system and the surgical instrument as well as the robotic system. Significant software modules such as imaging, reconstruction, and planning are integrated with the robot control module for smooth and automatic functionality in demonstrations. A user interface is coded for displaying the corresponding information to surgeons.

Aim 4: Demonstrate the adaptability towards clinical experiments (Chapter 6)

The semi-automated image-guided robotic brain tumor ablation is performed on a brain phantom, glutinous “tumor” material, using visible light color segmentation. System performance is evaluated and analyzed for potential usage in the future clinical application. NIR imaging test with mouse brain tumor and NIR fluorescence marker is conducted to verify the feasibility of the algorithms.

In the long-term perspective, this research will contribute towards automating medical procedures that combine the techniques originating in the industry and the robotic AI community with the medical constraints for clinical applications.

Chapter 2

BEHAVIOR TREE FRAMEWORK FOR MEDICAL AUTOMATION

This chapter[1] describes a modeling framework for the automation of medical procedures. Behavior Tree is used as a top-level modeling language for describing of medical sub-procedures and transition between each subtask. A new node type specifically designed for handling medical outcome and a data storage structure is introduced.

2.1 Autonomy in Medical Robotics

As surgical robotics research progresses beyond teleoperation towards automation, there is a need to robustly represent high-level medical tasks and deliver intelligent surgical plans based on the decision-making of artificial intelligence. Autonomy in robotic surgery does not mean the absence of surgeon [17]. Instead, it involves the perception of the environment by the robotic system and a corresponding adaption of its behavior to the changing environmental parameters [18] under the supervision of the surgeon. Combined with advanced medical imaging technology and modeling techniques, as well as the traditional CAD/CAM related technologies from the industry, a certain degree of autonomy in robotic surgery may relieve the surgeon from tedious and receptive work and exhibit better overall precision and accuracy of the surgical intervention.

A few applications of autonomous medical robotics have achieved clinical approval over the last few decades. Most of these applications are related to orthopedic surgery, neurosurgery, and radiotherapy. ROBODOC$^{\text{TM}}$ was introduced into orthopedic surgery since 1992 [19], for execution of pre-planned cuts in total hip replacement [20]. NeuroMate$^{\text{TM}}$ is an

---

[1] Parts of this chapter are reprinted, with permission, from [16].

image-guided stereotactic robot that is able to automatically guide and perform neurosurgical procedures [21, 22], e.g., deep brain stimulation(DBS) and stereotactic electroencephalography(SEEG). Autonomous robotics has been applied to radiosurgery, such as the CyberKnife® system, which is able to track, detect and correct for even the slightest motion that might occur throughout treatment delivery in real-time [23], as well as the GammaKnife [24] for head positioning, planning, and treatment.

Recent academic research has demonstrated more intelligent behaviors in performing autonomous surgical sub-procedures. Knot tying in suturing is one automated surgical task studied by several researchers. [25] used a recurrent neural network to learn knot tying in robotic heart surgery, and [26] used iterative learning to automate the knot tying subtask in suturing at the superhuman performance. Robotic systems and methods for automatic needle steering have also been explored in [27, 28]. Other laboratory results include automated debridement [29] and cochlear implantation [30, 31].

2.2 Behavior Tree as A Multi-task Control Framework

Behavior Tree (BT) is a graphical modeling language which encodes the artificial intelligence (AI) behaviors into a tree. The traversal of the tree from the root node to leaf nodes realizes the decision-making and behavior execution of the AI. BT allows the graphic representation and formalization of complex action flows and thus facilitates the conversion into code and data streams [32]. BT architectures can be addressed in two types [33], i.e., event-driven BT and data-oriented BT. Event-driven BT attempts to minimize the amount of work done at each ticking frame, and thus guarantees the minimum computation and improvement on both performance and debugging. This type of architecture updates the tree only when an event occurs, e.g., when the state of a node changes. Data-oriented BT aims to boost the overall performance by optimizing the memory coherency. This type of architecture improves the cache performance by using a stack allocator for the whole BT.

While simple behaviors can be modeled using finite state machines (FSMs), and there are no claims that BTs are superior over FSM [34] from a theoretical viewpoint, BTs are starting to gain preference over FSMs in the AI community due to their flexibility, simplicity, and reusability. For large and sophisticated systems, BTs provide more scalable and modular logic [35]. In recent years, the BT notation has been extensively used for modeling the non-player characters (NPCs) in interactive video games, such as the Halo Series [36] and DEFCON [37]. In robotics, BTs have been recently tested as a multi-mission control framework for humanoid robot control [38–40] and unmanned aerial vehicle(UAV) control [41, 42].

This research explores the potential utility of BTs as a modeling language for intelligent robotic surgical procedures. The flexibility, reusability, and simple syntax of BTs will potentially help the surgeon and engineer model complicated surgical procedures and implement them in robotic surgery. To the best of our knowledge, this is the first time that BT is applied for modeling and control in medical robotics.

2.3 Medical Procedure Modeling using Behavior Tree

In robotics, classic motion planning from goal states and environmental feedback has for decades been considered as a general approach for automation. In the context of surgery, the robustness of the plans should be emphasized as the plans are only probabilistically successful. This thesis focuses on the development of a highly flexible framework using BT notation for the representation and sequencing control of automation in medical robotics.

2.3.1 Essence of the Behavior Tree

The BT notation models the system behaviors into a spanning tree via a set of hierarchical nodes. Transitions between nodes are specified by the several types of the parent node. A behavior tree consists of several types of nodes. All BT nodes can return one of three states: ‘running’, ‘failure’, and ‘success’. These nodes can be further grouped into three parts based on the functionality in the tree: root node, logic node, and leaf node. A root node is the top node of each BT. For each BT, there exists only a single root node. The logic nodes provide the transition logic between the different behaviors. The leaf nodes of a BT execute the actual action commands that control the AI entity. Listed below are five types of the most frequently used nodes and their symbols in the construction of a BT.

Root $\varnothing$ **:** generates enabling signal with a certain frequency.

Sequence $\rightarrow$ **:** enables and executes its children sequentially and returns success iff all children return success.

Selector (Priority) ? **:** enables and executes its children sequentially and returns success the first time a child returns success.

Parallel $\rightrightarrows$ **:** enables its children sequentially for parallel execution. It returns success iff the fraction of its children reporting success is greater than S, where $0 < S < 1$.

Decorator $\diamondsuit$ **:** executes its children until a certain condition is satisfied.

Action $\bigcirc$ **:** performs a certain subtask and at each frame, returns ‘running’, ‘failure’, or ‘success’. It belongs to the leaf node type.

The implementation of BT framework is based upon the work from [40]. The enabling methods of each node are modified such that the efficiency of the tree traversal is improved. Instead of executing all nodes at each ticking frame, the status of the currently active nodes is checked and updated if its children’s status is updated. A general BT for any medical procedure can be expressed in Figure 2.1. The treatment procedure takes place only after the disease is successfully diagnosed.

In addition, to meet the medical requirements and handle the uncertainty in robotic surgery, a new type of BT node and a data structure is implemented.

Recovery node

In robotic surgery, possible failures or incomplete results may occur during the robotic intervention. To deal with these imperfect outcomes, a **recovery** $\circlearrowright$ node type is implemented. This type of node is able to initiate a recovery procedure that brings the robot to a safety

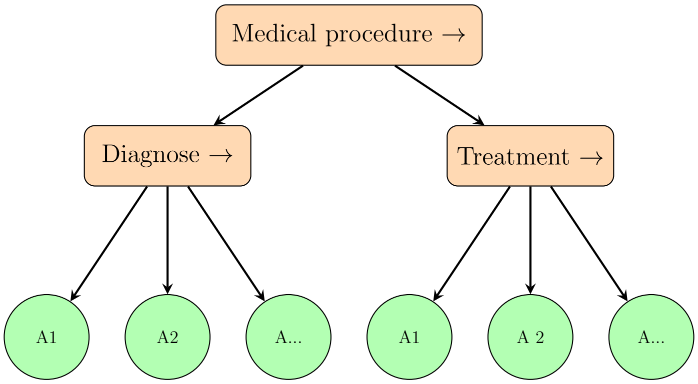

Figure 2.1: Generalized BT representation of medical behavior.

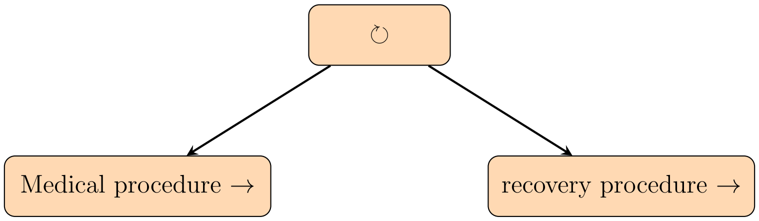

Figure 2.2: Generalized BT representation of medical behavior with recovery capability.

region in the surgical environment when the main treatment procedure is not successful, and then repeat the major surgical procedure until a specified status is reached.

A recovery node has only two children (Figure 2.2). The first child has a higher priority over the second child, and therefore usually represents the main surgical procedure. The second child represents the recovery procedure which usually resets the robot state and prepares for the next trial of a robotic intervention. The recovery node returns success if and only if the first child succeeds, otherwise the recovery procedure (second child) will be executed and then repeat the execution of the first child. This node returns failure if the first child fails after a certain number of repetitions C or the recovery procedure fails. The pseudocode is described below in Algorithm 1.

Algorithm 1 Recovery Node.execute()

```
if $getState(child(1)) = Success$ then
    return $Success$
else if $getState(child(1)) = Running$ then
    return $Running$
else if $getState(child(1)) = Failure$ then
    $execute(child(2)); counter{+}{+}$
    if $getState(child(2)) = Success$ and $counter \leq C$ then
        $execute(child(1))$
        return $Running$
    else if $getState(child(2)) = Failure$ or $counter > C$ then
        return $Failure$
    else if $getState(child(2)) = Running$ then
        return $Running$
    end if
end if
```

Blackboard

A shortcoming of the existing BT implementation [40] is the lack of a mechanism for data flowing between nodes. All data are encapsulated inside each individual node. However, medical procedures usually involve large data sets that need to be passed from one step to another, e.g., the CT scans took at the beginning needs to be referred later. To address this problem, a global **blackboard** data store is implemented. The blackboard contains a set of data generated and consumed by leaf nodes and provides a set of methods to manipulate the data, such as read, write, update and delete. A leaf node can link to the blackboard instance via pointer reference. Each BT contains single blackboard instance for shared data flow between leaf nodes.

Blackboard is implemented as a hash table, which maps each key (name of the data) to a block of memory for value storage. Each operation (insert, delete, search) yields on average $\mathcal{O}(1)$ time complexity. Figure 2.3 gives an example of how the data is stored internally alongside with the BT.

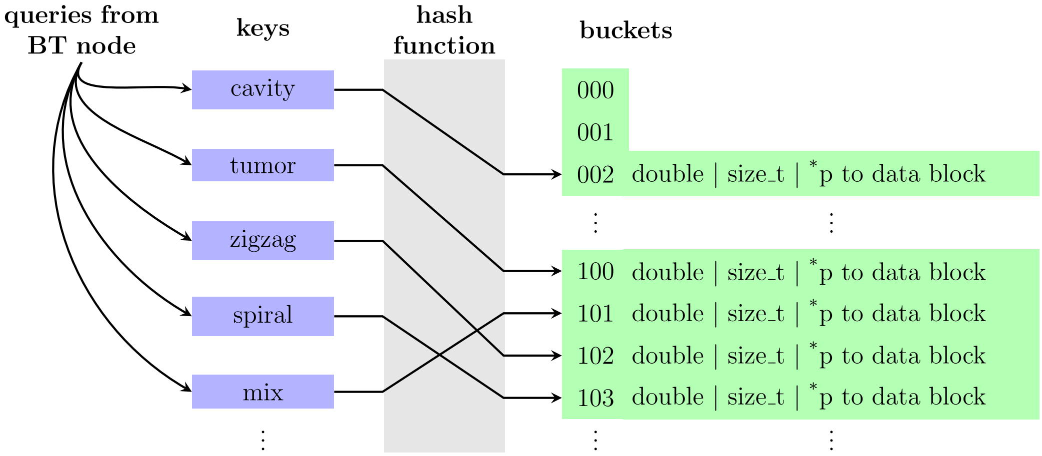

Figure 2.3: Blackboard implementation in semi-automated brain tumor resection.

2.3.2 Behavior Tree Representation of the Semi-automated Brain Tumor Ablation

In this study, the procedure for brain tumor ablation can be divided into six major steps sequentially: 1) scanning, 2) model creation 3) plan generation, 4) surgeon authorization, 5) plan execution and 6) examination. A sequence node is used to combine these major steps. Each step can be further divided into several subtasks. Each specific subtask is modeled as a leaf node - action node. As addressed above, a recovery node is used to handle possible incomplete or unsuccessful robotic intervention. The recovery procedure includes two steps. First, it will clear all the current generated plans in the blackboard and reset the BT. After that, it will start an initialization process to bring the robot to a known safety region. Figure 2.4 describes the BT representation of this semi-automated tumor ablation procedure.

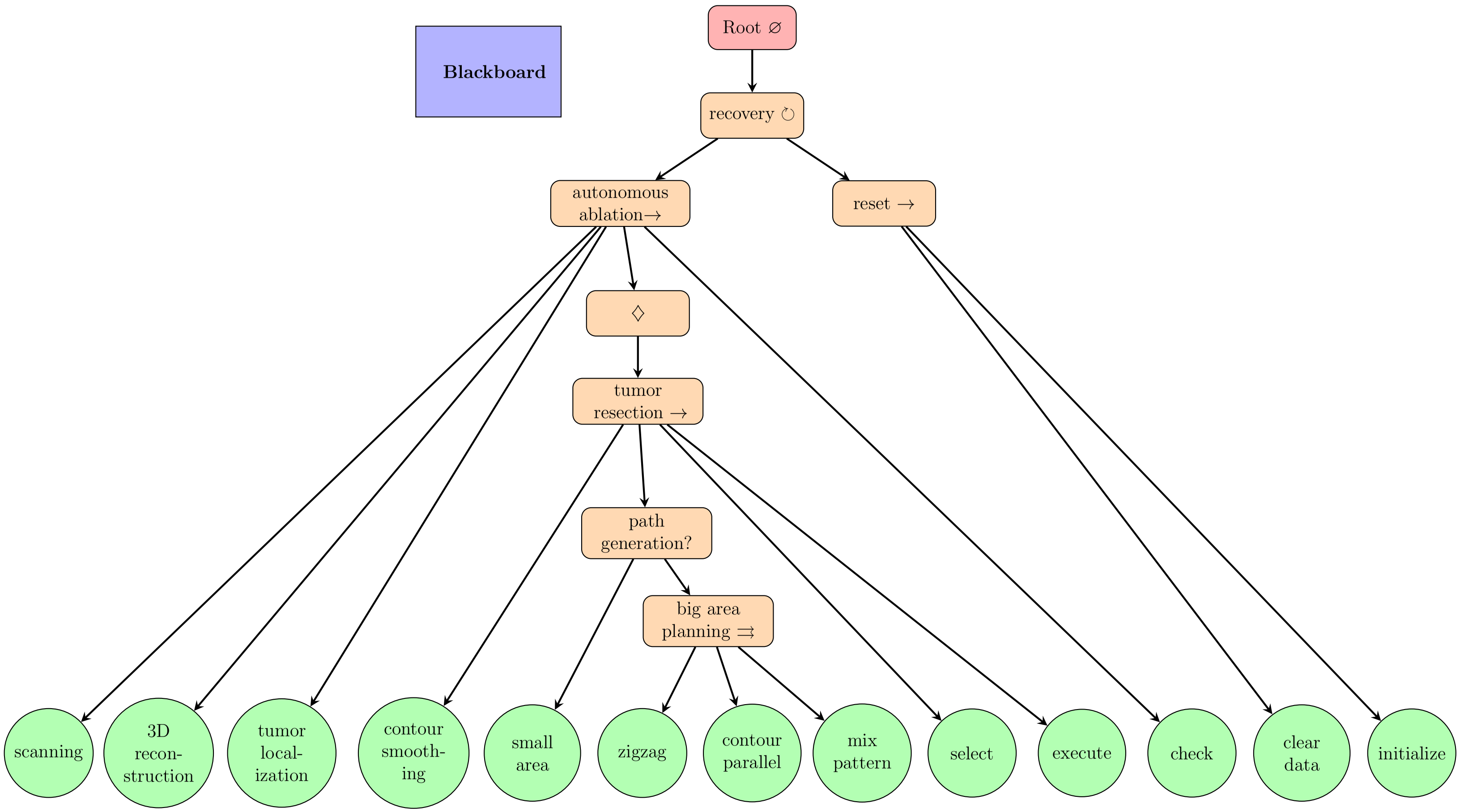

Figure 2.4: Behavior Tree representation of the semi-autonomous robotic ablation procedure. Action nodes are in green color. Logic nodes are in orange color.

Chapter 3

PATH PLANNING

This chapter[1] presents robust path planning methods for robotic ablation of tumor residues in various shapes, which are represented in point-clouds instead of analytical geometry. Along with the path plans, metrics are delivered to the surgeon for selecting the best plan for the automated robotic ablation.

3.1 Background and Related Work

3.1.1 Path Planning in Robot-assisted Medical Procedure

Most of the path planning in current robot-assisted surgery focus on 1) minimizing the tool path length and 2) avoiding the collision with the vital tissue when approaching the target. In recent years, motion planning for robotic needle steering is one of the most intensively studied examples for medical procedures including tissue biopsies, tumor ablation, and brachytherapy cancer treatment. Alterovitz et al. [44, 45] developed a motion planning algorithm for flexible needle steering that considers the uncertainty in robotic motion and maximizes the probability of avoiding collisions and reaching the target. Durham et al. [46] presented a 3D, constant time, motion planning algorithm for steerable needles using inverse kinematics. Jackson [47] proposed a path planner for autonomous robotic suturing that aimed to minimize the interaction forces between the tissue and needle. Bernardes et al.'s method [27] combined closed-loop feedback with intraoperative path replanning for dynamic scenes. Other related planning in medical fields includes minimally invasive surgery, where the optimal port placement and pose planning of the robot were discussed [48], and in virtual

---

[1] Parts of this chapter are reprinted, with permission, from [43].

endoscopy, where the optimal guidance path for endoscopic exploration of 3D medical images was computed [49].

3.1.2 Complete Coverage Path Planning

The intraoperative path planning in this study is related to the Complete Coverage Path Planning (CCPP), which requires the robot to visit each area in the target region, i.e., the residual tumor. Many algorithms based on a two-dimensional (2D) environment have been developed over the decades for applications in Computerized Numerical Control (CNC) machining, such as the generation of cutter paths in pocket milling [50–52], in which case the geometry of the target region is well defined a priori using a CAD model. Another heavily studied area of CCPP is in mobile robotics [53,54] such as cleaning robots [55], lawn mowers, underwater searching robots and automated farm machines [56], where the geometry of the target region is unknown, but robots are able to perform dynamic planning with the feedback from onboard sensors.

3.1.3 Analogy to the Industrial Task

In this project, the target regions (residual tumors) consist of a set of point-clouds generated from SFE image processing. The proposed CCPP is based on the point-clouds, which contain limited geometrical information. A similar approach is found from reverse engineering in rapid prototyping manufacturing. In that case, the point-cloud is obtained by a scanning system from existing physical profiles, such as sculptures. The traditional approach is to reconstruct the CAD model from point-clouds [57, 58] before the generation of the tool path. However, the reconstruction procedures are computationally inefficient and require interaction by users with advanced knowledge of surface modeling [59]. Alternative methods without the entire surface reconstruction include Z-map modeling [60], 3D biarc fitting [61] and moving least-square surfaces [62]. These methods are relatively fast but inaccurate due to the noisy points input.

In this thesis, the proposed path planning for generation of robotic ablation plans will need to combine the above-mentioned methods with the consideration of contour/shape irregularity as well as the surface uncertainty.

3.2 Planning Algorithms

3.2.1 Problem Definition and Assumption

Assumption

In this study, following assumptions are made:

1. All residual tumors are homeomorphic to a sphere, i.e., there are no holes in each residual tumor or only the outermost tumor boundary is analyzed.
2. All cancerous tissue remains on the surface of the surgical cavity, although it is possible in real clinical case that the tendrils may go deeply into brain tissue, in which case another scan - plan - ablation cycle will be initiated.
3. The surgical cavity is close to an inverted shallow spherical dome, but its inner surface can be rough. This assumption is based on the reachability of the currently available surgical tool.

Problem definition

The objective of the path planner is to find complete coverage path plans given a 3D segmentation map of each residual tumor detected in the surgical cavity. More precisely speaking, given a set of points $\boldsymbol{P_c}$ that represent the contour of a residual tumor and a set of points $\boldsymbol{P_s}$ that describe the inner surface geometry of that margin, as well as a minimum circular treatment area A_t of the surgical tool, the goal is to deliver a finite set of possible path plans $\boldsymbol{S}$ that cover the entire margin area for robotic ablation.

$$\boldsymbol{S} = Planner(\boldsymbol{P_c}, \boldsymbol{P_s}, A_t) \tag{3.1}$$

where $\boldsymbol{S} \neq \varnothing$, $0 < |\boldsymbol{S}| \leq n$, n is an integer as the maximal number of plans. ($n = 3$ for current version of the planner)

3.2.2 Complete Coverage Path Planning with Geometry Irregularity

Guidance plane and shape factor

The remaining residual tumors after the major removal could be represented in any arbitrary geometry and size. By assumption, the residual tumors stay on the surface of the surgical cavity, thus a guidance plane called $\boldsymbol{Pl_g}$ is defined such that the projection of the point-cloud $\boldsymbol{P_c}$ onto $\boldsymbol{Pl_g}$ preserves the shape similarity. In this study, to get the maximal shape similarity, the guidance plane is chosen as a plane perpendicular to the surface normal of each tumor residue. The surface normal is computed as the average of point normals using Point Could Library [63]. Figure 3.1 describes the guidance plane $\boldsymbol{Pl_g}$ of each tumor residue in the surgical cavity.

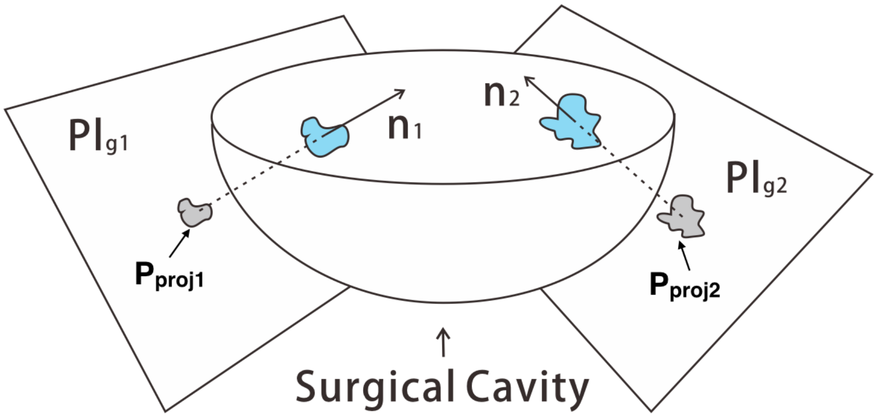

Figure 3.1: Illustration of the guidance plane and surgical cavity.

The projection generates a set of 2D points $\boldsymbol{P_{proj}}$ with respect to the plane $\boldsymbol{Pl_g}$. The shape analysis is performed upon the polygonal approximation of the point set $\boldsymbol{P_{proj}}$. Shape characterization [64, 65] is a large area of image analysis, even a brief review is beyond the scope of this work. This work focuses on the analysis of shape irregularity, i.e., shapes that have irregular, asymmetric and serrated edges, as do most of the brain tumor residues. **Circularity** is chosen for overall evaluation of the shape irregularity and is described by Equation 3.2.

$$f_{circ}(\boldsymbol{P_{proj}}) = \frac{4\pi A}{P^2} \tag{3.2}$$

where P is the perimeter of the polygon consisting of $\boldsymbol{P_{proj}}$, A is the corresponding area computed using Green's Theorem, derived as Equation 3.3. Appendix A gives the detailed derivation.

$$A(\boldsymbol{P_{proj}}) = \sum_{k=0}^{n-1} \frac{(x_{k+1} + x_k)(y_{k+1} - y_k)}{2} \tag{3.3}$$

where $n = |\boldsymbol{P_{proj}}|$, (x_k, y_k) is the k-th point of $\boldsymbol{P_{proj}}$ in counter-clockwise order.

It is obvious that the circularity of a circle is 1, and much less than one for an irregular shape. Circularity determines the path patterns that will be used in planning. Another key measurement is the enclosed area A of the boundary $\boldsymbol{P_{proj}}$, which determines the maximal number of plans delivered to the surgeon.

Planning flowchart

The flowchart of the plan generation is described in Figure 3.2. The approach is divided into five major steps:

- projection onto the guidance plane
- smoothing
- 2D coverage path planning on the guidance plane
- reverse projection onto the original 3D surface formed by point-cloud
- path interpolation on a 3D surface

The path planning algorithms are further divided based on the area of the shape into two basic groups for improving the efficiency of robotic execution and reducing the removal of healthy tissue.

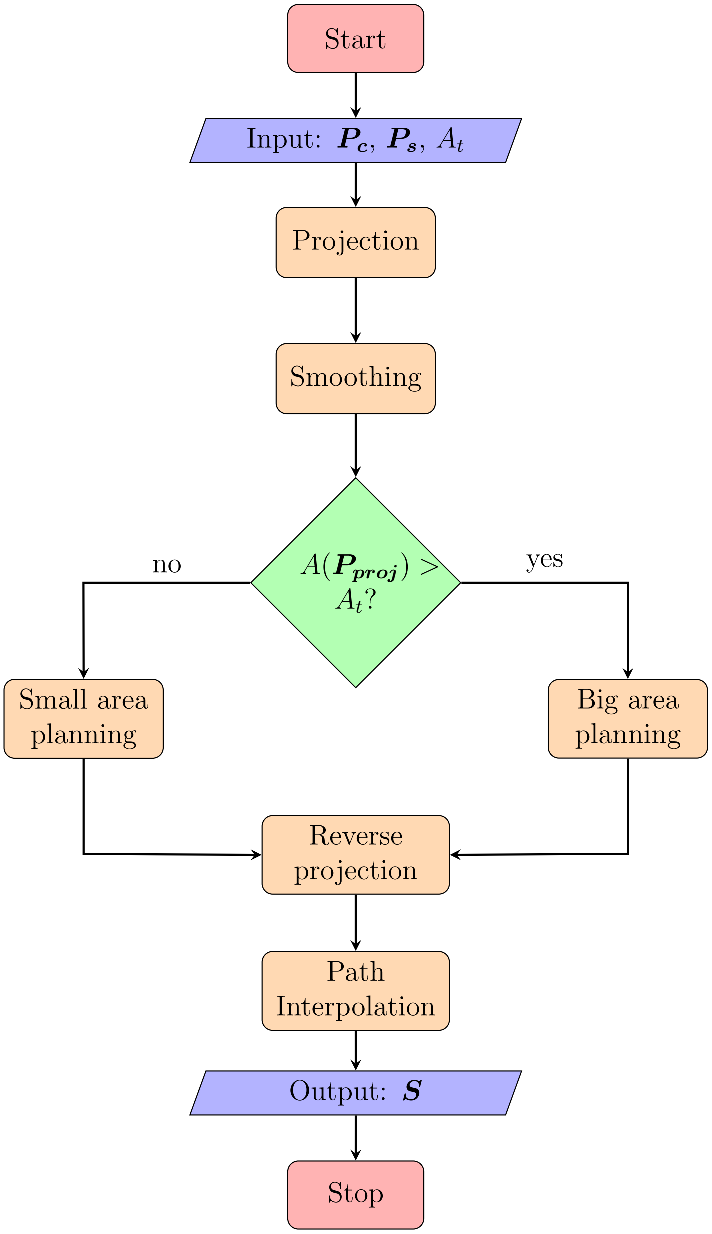

Figure 3.2: Flowchart of the path planner.

3.2.3 Algorithms

Planning with shape irregularity - small area

The small area shape is defined as a polygon consisting of $\boldsymbol{P_{proj}}$ whose area is no larger than the minimal treatment area, i.e., $A(\boldsymbol{P_{proj}}) \leq A_t$. A_t is defined as the minimum area cleaned by the surgical probe when approaching to the tissue surface, and is approximated as a circle in this study.

The coverage rate of a minimum treatment area is defined as the percentage of the $\boldsymbol{P_s}$ that is located within the minimum treatment circle co-centered with $\boldsymbol{P_{proj}}$. The path plan for the tumor residue with a small area is determined by the coverage rate as described in Algorithm 2.

Algorithm 2 Small area path generation

```
Require: $\boldsymbol{P_c} \neq \varnothing$ , $\boldsymbol{P_s} \neq \varnothing$, $A_t \geq A(\boldsymbol{P_{proj}}) > 0$
if coverage rate $\geq 95\%$ then
    $\boldsymbol{P_{small}} \leftarrow$ centroid of $\boldsymbol{P_{proj}}$
else
    $\boldsymbol{P_{small}} \leftarrow \boldsymbol{P_{proj}}$
end if
return $\boldsymbol{P_{small}}$
```

Planning with shape irregularity - big area

The big area shape is classified as a polygon consisting of $\boldsymbol{P_{proj}}$ that is larger than the minimal treatment area A_t, i.e., $A_{\boldsymbol{P_{proj}}} > A_t$. Three possible types of plan for each big area shape are explored: **zigzag**, **contour-parallel** and **mixed pattern** of both.

Zigzag and contour-parallel are very common path patterns used in industrial CNC pocket milling. Here, the similarity and difference compared to industrial applications is addressed. The major difference is that in CNC machining, pocket's contour is well defined as arcs, lines using CAD/CAM, while in this work, the tumor's contour is defined as a set of points derived from image processing. In this case, contours can be much noisier even after smoothing compared to the industrial case. Although a certain level of smoothing is performed before planning, it is not wise to filter out all noise that is potentially tumor cells. The proposed algorithms are able to robustly deal with edge noise and avoid numerical error.

1. Zigzag path planning is computationally the most efficient algorithm among abovementioned plans, although this plan sometimes generates inefficient paths for robotic execution. When dealing with very irregular shapes, such as shapes with tendrils, multiple tool retractions are required. The Algorithm 3 for zigzag planning is based on the traditional zigzag planning [52] with modifications to fit the medical application.

Algorithm 3 Zigzag path generation

```
Require: $\boldsymbol{P_c} \neq \varnothing$ , $\boldsymbol{P_s} \neq \varnothing$, $A(\boldsymbol{P_{proj}}) > A_t > 0$
$d_{offset} \leftarrow \sqrt{A_t/\pi}$
$\boldsymbol{Mc} \leftarrow$ construction of monotone chains along sweeping direction from $\boldsymbol{P_{proj}}$
$\boldsymbol{P_{inters}} \leftarrow$ intersection points between $\boldsymbol{Mc}$ and parallel offsetting lines.
$\boldsymbol{P_z} \leftarrow$ sorting of $\boldsymbol{P_{inters}}$ into zigzag pattern
return $\boldsymbol{P_z}$
```

According to the ray casting algorithm, the intersection points computation normally generates an even number n of points and n-1 path segments on each parallel offset line. The middle point of each path segment lies alternately inside and outside of the polygon. However, numerical problems may occur in finite precision arithmetics such that any of the above criteria are violated. Thus, the validity of the generated intersection points are checked and extra neighboring points are inserted if needed before the sorting algorithm starts.

In the sorting part, all intersection points are grouped into two parts: “in” and “out”. As illustrated in Figure 3.3, an “in” point has an odd index number and is the starting point for an imaginary ray entering into the polygon. An “out” point has an even index number and is where the imaginary ray leaving the polygon.

The sorting of intersection points follows five steps:

step 1: Find “in” point of the lowest row as the starting point of a sub-path.

step 2: If not found, stop, path generation finished.

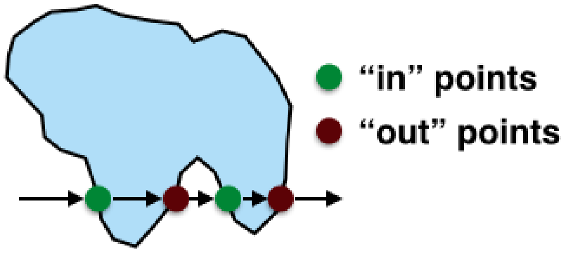

Figure 3.3: Definition of an “in” points and “out” point.

step 3: Append neighboring “in/out” point to form the zigzag pattern.

step 4: Find closest same group point of the next row and go to step 3.

step 5: Delete visited points, go to step 1 to create a new sub-path if there are points remaining.

2. Contour-parallel path planning uses a series of offsetting contours to cover the residual tumor. Although the computation time is longer than zigzag planning, the contour-parallel path cleans the serrated edges better. The computation of the offset contour is using the clipper library [66] which is based on Vatti's clipping algorithm [67]. The pseudocode is described in Algorithm 4.

Algorithm 4 Contour parallel path generation

```
Require: $\boldsymbol{P_c} \neq \varnothing$ , $\boldsymbol{P_s} \neq \varnothing$, $A(\boldsymbol{P_{proj}}) > A_t > 0$
$d_{offset} \leftarrow \sqrt{A_t/\pi}$, $\boldsymbol{P_p} \leftarrow \varnothing$
while $\boldsymbol{C_{offset}} \neq \varnothing$ do
    $\boldsymbol{C_{offset}} \leftarrow$ deflation of $\boldsymbol{C_{offset}}$ by $d_{offset}$
    $\boldsymbol{P_p} \leftarrow \boldsymbol{C_{offset}} \cup \boldsymbol{P_p}$
end while
return $\boldsymbol{P_p}$
```

3. Mixed pattern path planning combines the merits of zigzag and contour-parallel planning to deliver the most efficient ablation path for robotic execution: accurate contour following and fast ablation of inner material. The mixed pattern planning is designed to deliver the most efficient path for star-shaped tumor residues, e.g., tumor residue with tendrils. Although for some shapes, such as long ellipse-like shapes, the mixed pattern planning may result in the same path as the contour-parallel planning.

Algorithm 5 Mixed pattern path generation

```
Require: $\boldsymbol{P_c} \neq \varnothing$ , $\boldsymbol{P_s} \neq \varnothing$, $A(\boldsymbol{P_{proj}}) > A_t > 0$
$d_{offset} \leftarrow \sqrt{A_t/\pi}$
$\boldsymbol{C_{offset}} \leftarrow \boldsymbol{P_{proj}}$, $\boldsymbol{P_m} \leftarrow \boldsymbol{C_{offset}}$
while $\boldsymbol{C_{offset}} \neq \varnothing$ && $f_{circ}(\boldsymbol{C_{offset}}) < f_{circmin}$ do
    $\boldsymbol{C_{offset}} \leftarrow$ deflation of $\boldsymbol{C_{offset}}$ by $d_{offset}$
    $\boldsymbol{P_m} \leftarrow \boldsymbol{C_{offset}} \cup \boldsymbol{P_m}$
end while
if $\boldsymbol{C_{offset}} \neq \varnothing$ then
    if $A(\boldsymbol{C_{offset}}) > A_t$ then
        $\boldsymbol{P_{last}} \leftarrow$ zigzag path generation
    else
        $\boldsymbol{P_{last}} \leftarrow$ small area path generation
    end if
    $\boldsymbol{P_m} \leftarrow \boldsymbol{P_{last}} \cup \boldsymbol{P_m}$
end if
return $\boldsymbol{P_m}$
```

Figure 3.4 shows the generated 2D path plans on the guidance plane for an irregular shape. Both contour-parallel and mixed pattern cover the contour exactly. But for the zigzag pattern there exist over-cover and under-cover of the contour, which indicates more healthy tissue and not all tumor tissue will be removed.

3.2.4 Reverse Projection and Path Interpolation

Finally, the generated 2D path via-points are projected back onto the original surface of the point-cloud. For each 2D point, a search circle of radius 0.5 mm is used for computation of the depth using a weighted average of all points inside the circle. If no points in found inside the circle, the depth of the closest point is adopted. Linear path interpolation is performed

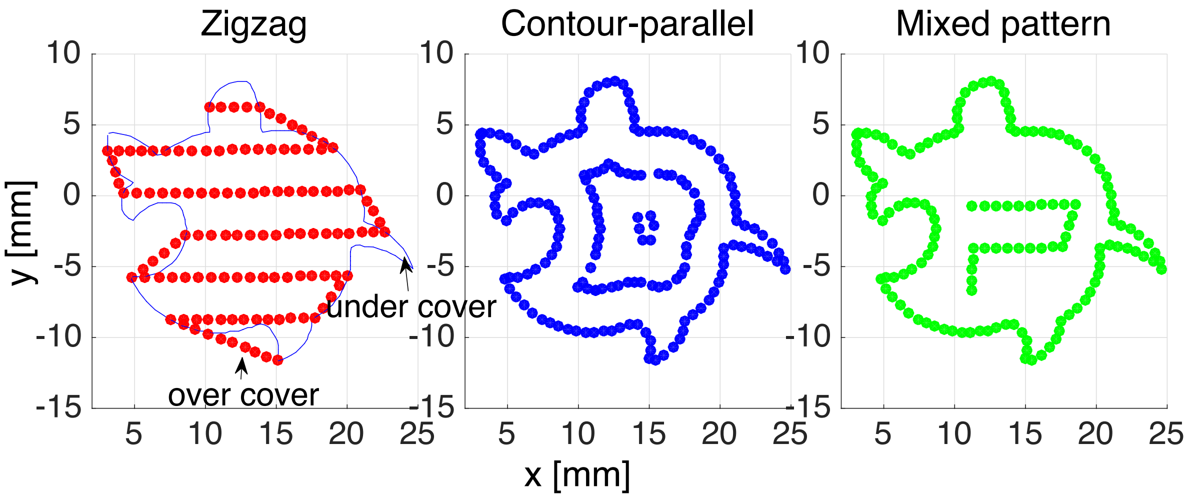

Figure 3.4: 2D path on guidance plane using three path patterns.

on the 3D surface such that the distance between each pair of neighboring points is no greater than 1 mm.

3.2.5 Planning Time Analysis

The computation time of each plan generation algorithm is analyzed using a simulated phantom with irregular shaped "tumor residues" as depicted in Figure 3.5.

The computation time of each plan based on an average of 30 runs on a machine with 4GB RAM and Intel Core$^{\text{TM}}$2 Quad cpu$^{\circledR}$ 2.5Ghz is compared in Figure 3.6. It indicates the computation complexity for each path pattern. The computation time using contour-parallel pattern increases dramatically with the increase of the number of vertices and shape complexity. The computation time of zigzag path is extremely fast and increases quasi-linearly with the number of vertices. For some margins with serrated edges, such as tumor residue 4, the mixed pattern planning is able to reduce the computation time remarkably compared to contour parallel planning (Figure 3.6-right), while for some margins with long and narrow shape like tumor residue 1, mixed pattern and contour-parallel planning result in the same plan (Figure 3.6-left).

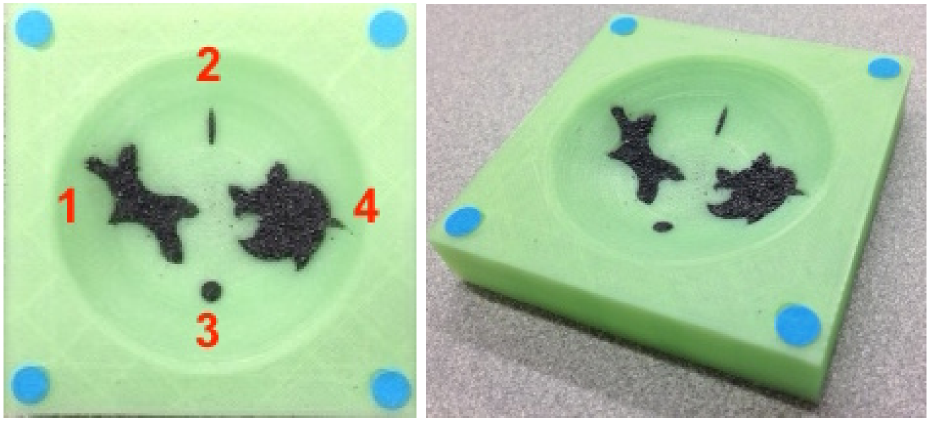

(a) (b)

Figure 3.5: Simulated phantom for performance analysis: (a) Top view with tumor indexing. (b) Perspective view.

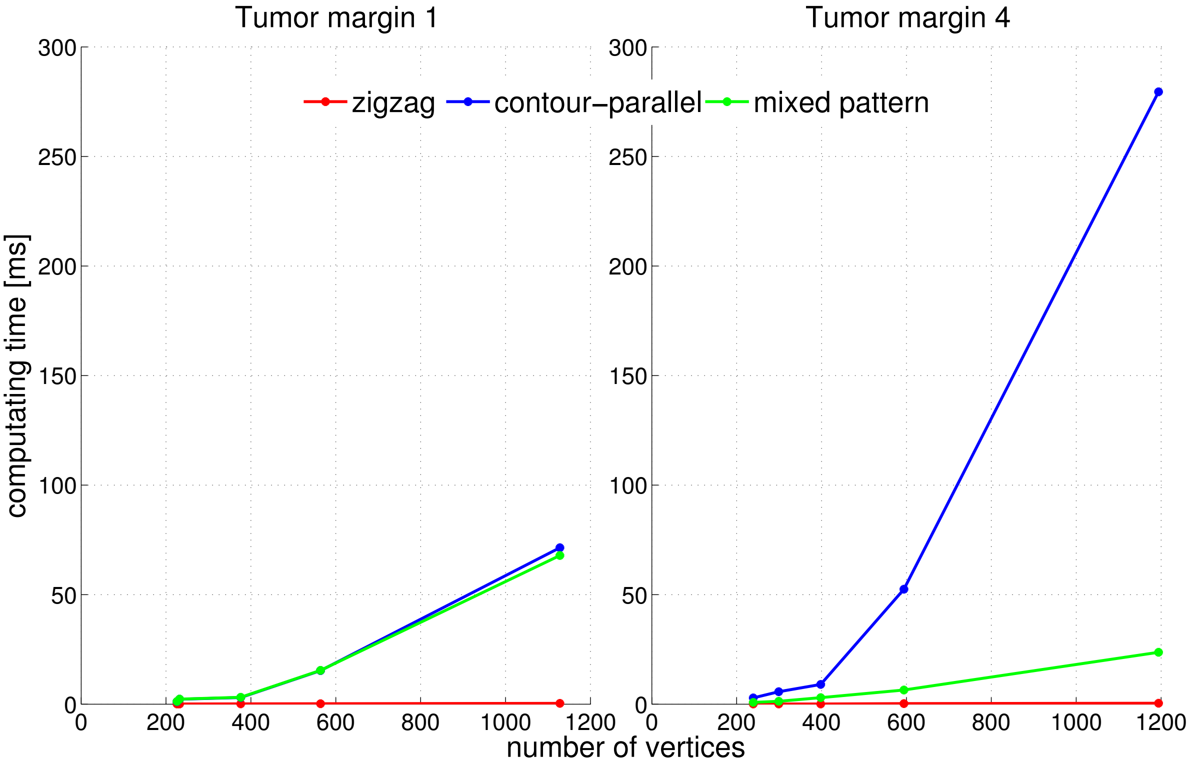

Figure 3.6: Computation time in millisecond using different path patterns of two bigger tumor residues.

3.2.6 Paths Plan Display

The final path plans $\boldsymbol{S}$ are represented by a set of via-points in 3D. Each plan is displayed on a terminal with the total number of via-points n_v for each plan, the number of tool retractions n_r and the estimated execution time which is roughly proportional to n_v.

Chapter 4

MEDICAL IMAGE PROCESSING

4.1 3D Image Reconstruction of the Surgical Cavity

4.1.1 3D Information Extraction from Endoscopic Images

Endoscopic imaging is an essential component of minimally invasive robotic surgery as it provides surgeons with visual information to precisely localize lesions in a complicated anatomic environment. Analysis of these diverse images for 3D information extraction requires sophisticated computerized quantification and visualization tools. Recent advances in computer vision and GPU computation techniques have enabled the creation of 3D and panoramic images from 2D medical endoscopic images at acceptable speed or even in real-time [68].

Image mosaicing [69] is an image fusion technique that has recently been applied in endoscopic image processing. It is a procedure of automatic alignment of multiple 2D images into a larger composition that expands the endoscopic view into a panorama. Studies have successfully applied image mosaicing to create a panoramic view of the tubular esophageal surface [70] and the cavernous surface of an entire bladder [71].

Stereo-endoscopes have been used in recent clinical applications to provide direct 3D information of a surgical scene. Algorithms with GPU or hybrid CPU-GPU enhancement have greatly improved reconstruction speed and allowed dense intraoperative surface reconstruction of soft tissue in real-time from stereo endoscopic images for minimally invasive surgery [68, 72]. An alternative approach based on structure from motion (SfM) techniques originating from robotic vision have given the conventional monocular 2D endoscopes 3D capabilities. Traditional feature detection algorithms have been applied to find the correspondence in an image pair. In [73], the authors used an optical flow algorithm to harvest 3D features from 2D endoscopic images; in [74], the Scale-invariant feature transform (SIFT) feature detector (computationally expensive but presumably with better performance) was used to find the vascular feature points in a surgical cavity.

In summary, the calibrated robotic motions of a single flexible endoscope can provide 3D surface models of complex surgical cavities with high accuracy, allowing guidance through small openings in the body.

4.1.2 Structure from Motion

Structure from motion is a computer vision technique that estimates the 3D model from a 2D images sequence sensed over time which may be coupled with location information. This process of 3D information recovery involves major tasks and algorithms including:

- Feature detection in each image
- Feature matching and validation between image pairs
- Depth recovery from triangulation
- Optimization and smoothing of the generated 3D model

Research work demonstrated in [74] showed the feasibility of creating a virtual 3D model of a spherical surgical cavity from a set of 2D SFE images using the conventional structure from motion technique in MATLAB. However, the MATLAB implementation had slow runtime and difficulties to integrate with autonomous plan execution. Moreover, the number of extracted feature points was limited and therefore resulted in a sparse point-cloud for surface reconstruction. This led to missing geometrical details in the case of a non-smooth surface.

To overcome the above limitations and improve the overall computational performance, the 3D reconstruction process is rewritten in C++ using alternative feature detection and matching algorithms, different triangulation orders as well as different optimization strategies. Additionally, SFE imaging in the wet surgical environment usually results in strong specular reflections in the image, which degrade the reconstructed 3D model due to the false detection and matching of these saturated points as feature points. To improve the robustness of reconstruction procedure, these saturated reflection points were removed in the SFE images before feature detection.

Reflection removal

The specular reflection in the SFE images is displayed as bright and saturated pixels. A binary mask is created from these saturated pixels through thresholding of the intensity. The color information in the mask is then restored from the neighboring pixels based on image inpainting method [75], which uses level sets to describe the missing regions and propagates the image information inwards along the image gradient. Figure 4.1 compares the same SFE image before and after reflection removal.

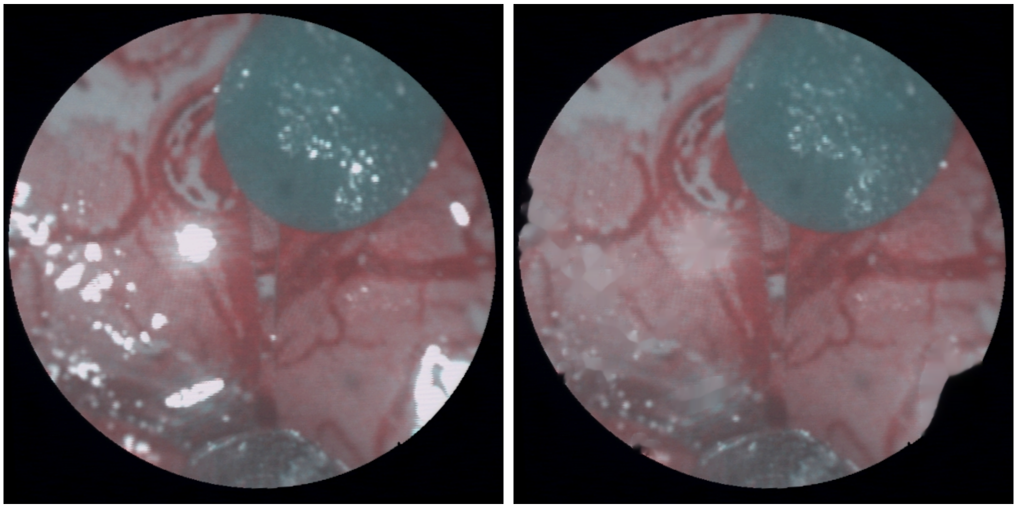

(a) (b)

Figure 4.1: Reflection removal: (a) Original SFE image. (b) Reflection removed in the same image.

It is noticed that in Figure 4.1(b), the saturated pixels are removed successfully, such that these points will not be classified as feature points in the reconstruction process. The color information of the small regions and central regions are recovered better compared to the large regions and edge regions, which are seen in the incomplete round boundary of the image.

3D reconstruction pipeline

Figure 4.2 describes the pipeline of the reconstruction process. This module executes the reconstruction procedure when requested by an action client node in the BT using ROS Action protocol and sends the generated point-cloud of the surgical cavity back to the client node. The details of software architecture implementation will be addressed later in Chapter 5. Here, the overall data flow in the reconstruction module is given in Figure 4.2.

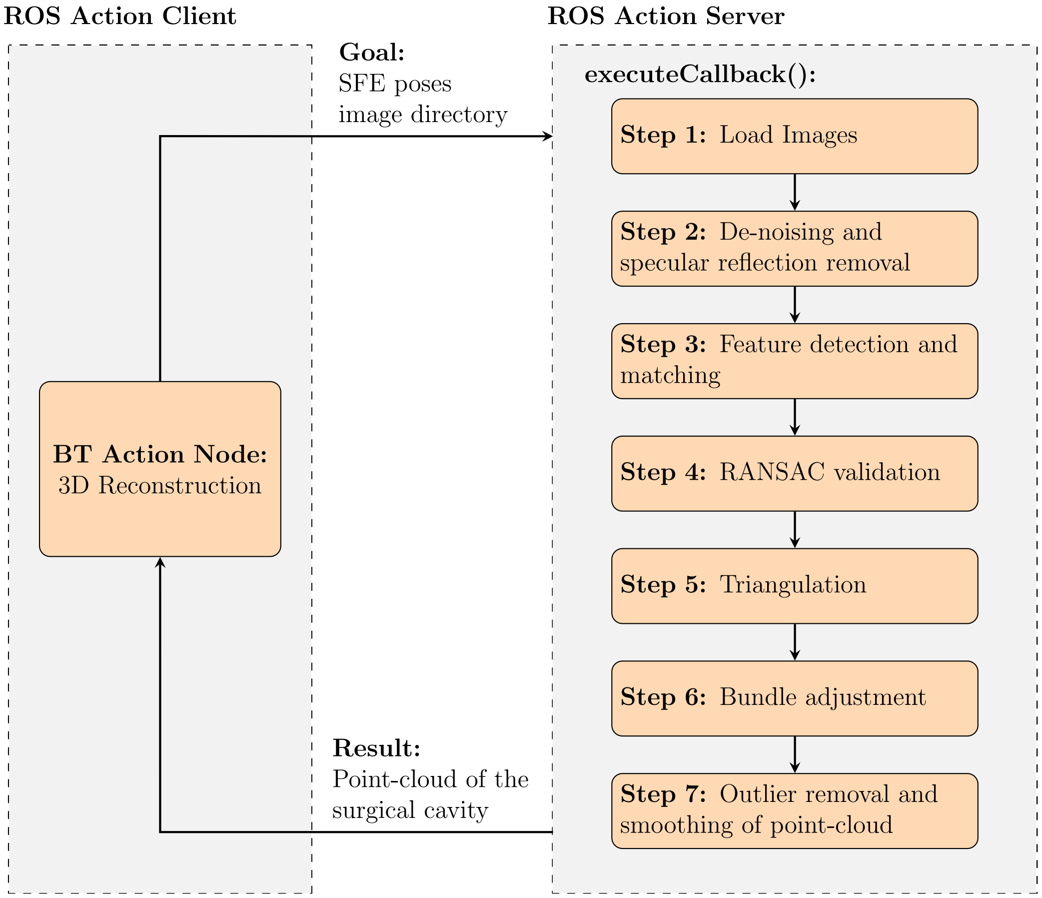

Figure 4.2: 3D reconstruction pipeline.

This new implementation is based on the OpenCV library [76] for image processing and the SSBA library [77] for bundle optimization. Oriented FAST and Rotated BRIEF (ORB) [78] feature descriptor is used in the new implementation. ORB uses FAST (Features from Accelerated Segment Test) in pyramids to detect the key points in each image and extracts the feature vectors from these key points using rotated BRIEF (Binary Robust Independent Elementary Features). The ORB descriptor uses an orientation compensation mechanism for key points detection and feature vector extraction. Compared to the previous implementation using SIFT feature descriptor, ORB yields more reliable features points in the SFE images at a much faster speed when testing the same SFE image set as listed in Table 4.1. Test in [78] also shows that ORB is less sensitive to the Gaussian noise in the image.

Performance improvements

Performance comparison between the old [74] and new implementation, based on the same SFE image input consisting of 30 frames, is given in Table 4.1.

Table 4.1: A comparison between the old and new implementations

	`old method`	`new method`
`Language`	MATLAB	C++
`ROS and BT Integration`	no	yes
`Reflection Removal`	no	yes
`Feature Descriptor`	SIFT	ORB
`Depth Recovery Order`	add frame in time sequence	add frame with the best triangulation
`Bundle Adjustment Order`	incremental	global
`Runtime (CPU)`	>200 s	≈ 10 s
`Point-cloud Size`	≈ 200	1999

It is shown that the performance of the reconstruction algorithm was significantly improved in the new implementation. The runtime is about 20 times faster based on solely CPU computing, and this speed can be further improved by enabling GPU computing capability. Furthermore, the recovered point-cloud of the surgical cavity is about 10 times denser compared to the previous result [74].

4.2 Toward Real-time Tumor Identification in Fluorescence Images

[1]For patients with malignant brain tumors (glioblastomas), a safe maximal resection of the tumor is critical for an increased survival rate. However, complete resection of the tumor is hard to achieve due to the invasive nature of these tumors, where the margins of the tumors become blurred from tumor to more normal brain tissue, but in which single cells or clusters of malignant cells may have invaded. Recent developments in fluorescence imaging techniques have shown great potential for improved surgical outcomes by providing surgeons intraoperative contrast-enhanced visual information of tumor in neurosurgery. The current near-infrared (NIR) fluorophores, such as indocyanine green (ICG), cyanine5.5 (Cy5.5), 5-aminolevulinic acid (5-ALA)-induced protoporphyrin IX (PpIX), are showing clinical potential to be useful in targeting and guiding resections of such tumors. Real-time tumor identification in NIR imaging could be helpful to both surgeons and patients by reducing the operation time and space required by other imaging modalities such as intraoperative MRI, and has the potential to integrate with robotically assisted surgery. In this section, a segmentation method based on the Chan-Vese model was developed for identifying the tumor boundaries in an ex-vivo mouse brain from relatively noisy fluorescence images acquired by a multimodal scanning fiber endoscope (mmSFE). Tumor contours were achieved iteratively by minimizing an energy function formed by a level set function and the segmentation model. Quantitative segmentation metrics based on tumor-to-background (T/B) ratio were evaluated. Results demonstrated feasibility in detecting the brain tumor at quasi-real-time and has the potential to yield improved precision brain tumor resection techniques or even

---

[1] Parts of this section are reprinted, with permission, from [79].

robotic interventions in the future.

4.2.1 Introduction and Background

Clinical background of fluorescence imaging in brain tumor resection

In resection of malignant gliomas (e.g. glioblastomas) and other brain tumors, an important aim is the near complete resection of the tumor without damaging the healthy tissue, because the extent of removal (EOR) is a critical factor for tumor progression and survival. However, this goal is challenging for surgeons as the tumor boundaries are often not well delineated because of the invading front of tumor cells. In cases of tumor recurrence, tumor tissue at the margin of a surgical cavity is often hard to distinguish from other treatment effects such as radiation using conventional imaging and surgical techniques. Therefore, imaging modalities such as MRI and ultrasonography are being configured for intraoperative use to locate tumor tissue or residual, recurrent tumor. However, these imaging modalities are expensive and require significantly modified instrumentation and operating room design, and therefore have not found broad acceptance. While these modalities may reveal the shift of the brain after opening the cranium, they do not provide imaging at cellular resolution.

Recently, imaging techniques based on fluorescence contrast agents for tumor visualization have been explored for neurosurgery to intraoperatively identify tumor tissue. Such imaging techniques allow the surgeon to image the fluorescent signal that correlates in most instances to the tumor tissue with capabilities of real-time, non-contact and preservation of background view. Clinical developments in imaging systems and biomarkers have made progress towards clinical application [80, 81]. Tumor Paint$^{\mathrm{TM}}$ (Blaze Biosciences, Seattle, WA), a molecular biomarker conjugated with ICG, has shown potential for delineating the brain tumors in real-time [8]. 5-ALA, another widely studied contrast agent which is approved by European Medicines Evaluation Agency for tumor visualization based on the accumulation of PpIX, has been used in multiple clinical trials for resection of malignant gliomas [10, 82, 83]. The reported results [11, 82, 83] indicate an improved rate of gross total resection (GTR), which may assist surgeons in near-complete brain tumor resection to increase survival and reduce neurological deficits. Fluorescence imaging of brain tumors in real time at cellular resolution (confocal laser endomicroscopy (CLE)) during surgery with comparable diagnosis results to conventional pathology techniques is of particular neurosurgical interest in that it can identify metastasizing tumor cells invading the brain at the tumor border [84]. The high resolution of confocal imaging comes with a very limited real-time visual field (sub-millimeter range) which add inefficiencies and complexities that can be overcome by reducing the resolution to multi-cellular and expanding the visual field to the millimeter range.

Tumor detection in fluorescence images

Fluorescence-guided surgery has shown potential in improving the clinical outcome. Although results of surgery using 5-ALA have been generally positive, exact identification of cells with 5-ALA signal at near cellular resolution remains elusive. A technical difficulty in tumor visualization, especially for thinner regions of residual tumors, is that the fluorescence signal becomes very weak due to the lower indicator concentration and photo-bleaching, e.g. with 405 nm laser excitation of low concentrations of PpIX from 5-ALA. Since cancer cells essentially disappear among the healthy brain tissue when photo-bleaching occurs, keeping laser power levels low will help avoid this permanent loss of signal during surgery. Therefore, a longer integration time is required for capturing image frames in order to achieve an acceptable signal-to-noise (S/N) ratio for the detection of the residual or infiltrating tumors at low laser power. Many developments in the design of imaging systems, such as the mmSFE [15], have been made to improve their S/N ratio and image quality with a reduced integration time, light exposure, and auto-fluorescence background subtraction [85]. In addition, algorithms for medical image processing can provide reliable tumor segmentation in an automated manner despite the relatively noisy and low-contrast images.

In the context of semi-autonomous robotic neurosurgery

Another need for automated tumor detection in fluorescence images arises from the exploration of robotic neurosurgery. Since the acquisition of fluorescence images might be slowed for the improved residual tumor visualization, manual removal of residual tumors can be a slow, repetitive, and tedious procedure for surgeons. Thus, this procedure might be automatically guided by a robot that removes fluorescent cell clusters by extremely precise surgery or ablation in the debulked tumor cavity. With this background, a reliable and fast tumor detection method is required for medical planning and intervention by a surgical robot with automation. In the following sections, methods for reliable tumor detection in the presence of clinically significant levels of fluorescence will be addressed and the performance of tumor recognition and segmentation algorithms will be analyzed.

4.2.2 Methods

Segmentation is an important procedure in medical image processing to extract useful information for medical planning, diagnostics, and treatment. Many research studies on the segmentation of various image modalities e.g. MRI [86], CT [87] have been published. Because fluorescence tissue images display high noise levels at the background and various signal intensities due to the uncontrolled imaging distances, the traditional thresholding and edge detection methods show poor segmentation results of these types of images. An alternative approach for segmenting the images with low-contrast edges is to use region-based active contour models, which are known for the robustness but high computational complexity. Region-based active contour models use a certain region descriptor to guide the curves evolving towards the boundary of each region of interest, thus to detect the objects in the images. The Chan-Vese model [88] is one prominent variation of the region-based active contour models that is applied for this fluorescence image-guided robotic surgery. This algorithm can be used in a repeated and automated manner during residual tumor clean up, as each time the top layer of fluorescence cells are removed, a new underlying layer is revealed and its boundary needs to be automatically demarcated to guide the robot with surgeons monitoring.

Segmentation problem and active contour model

The basis of the proposed segmentation method is a Mumford-Shah model [13], which approximates a general grayscale image into a piecewise smooth function. Let the domain Ω be a bounded subset of R^2 and function $f(x, y) : \Omega \to R$ be a given grayscale image to be segmented, and $u(x, y)$ be the piecewise approximation of the original image, it is smooth within each connected region in the image domain Ω separated by the contour C , i.e. in region $\Omega \backslash C$, the problem is to find such contour $C \subset \Omega$, which segments the image $f(x, y)$ into non-overlapping regions. The Mumford-Shah energy functional is defined as follows:

$$\begin{aligned} F_{MS}(u(x,y),C) &= \mu \boldsymbol{Length}(C) \\ &\quad + \lambda \int_{\Omega} (f(x,y) - u(x,u))^2 \, dx \, dy + \int_{\Omega \backslash C} |\nabla u(x,y)|^2 \, dx \, dy \end{aligned} \tag{4.1}$$

where $\mu > 0$, $\lambda > 0$ are fixed weighting parameters.

A special case of the Mumford-Shah energy function is given by the Chan-Vese model [88], which assumes the image approximation $u(x, y)$ to be a piecewise constant function allowed to have only two values with respect to the contour C (Equation 4.2).

$$u(x,y) = \begin{cases} c_1 & (x,y) \text{ is inside } C, \\ c_2 & (x,y) \text{ is outside } C. \end{cases} \tag{4.2}$$

The Chan-Vese energy function further adds an additional area penalizing term and is modified as Equation 4.3.

$$\begin{aligned} F_{CV}(c_1, c_2, C) = \mu \boldsymbol{Length}(C) + \nu \boldsymbol{Area}(C) + \\ \lambda_1 \int_{\text{inside } C} |f(x,y) - c_1|^2 \, dx \, dy + \\ \lambda_2 \int_{\text{outside } C} |f(x,y) - c_2|^2 \, dx \, dy \end{aligned} \tag{4.3}$$

where $\mu > 0$, $\nu \geq 0$, $\lambda_1 > 0$, $\lambda_2 > 0$, are pre-tuned weighting parameters for penalizing the length of the C, the enclosed area of C as well as the difference between the piecewise constant model $u(x,y)$ and the input image $f(x,y)$. Image segmentation can be obtained as the best two-phase piecewise constant approximation u of the image f by finding a minimizer of the problem (4.3).

However, in practice, it is difficult to minimize both of the energy functions Equation 4.1 and Equation 4.3 due to the non-convexity, although theoretical existence and regularity of the optimal results were proved in [89] and [90]. Therefore, the Chan-Vese algorithm proposed a level set formulation [91] for convex approximation to solve the optimization problem.

Level set formulation of the model

Instead by explicitly searching over all boundary sets C, the Chan-Vese algorithm uses a level set function to minimize the energy function. The boundary sets $C \subset \Omega$ is obtained by zero-crossing of a level set function $\Phi(x,y) : \Omega \to R$ as in Equation 4.4.

$$C = \{(x,y) \in \Omega : \Phi(x,y) = 0\} \tag{4.4}$$

The inside and outside of the contour C are distinguished by the sign of $\Phi(x,y)$.

$$\text{inside } C = \{(x,y) \in \Omega : \Phi(x,y) > 0\} \tag{4.5}$$

$$\text{outside } C = \{(x,y) \in \Omega : \Phi(x,y) < 0\} \tag{4.6}$$

In general, there exist multiple representations of level set function for a given C. With the assistance of the Heaviside step function H for numerical computation, which is defined as:

$$H(s) = \begin{cases} 1 & s \geq 0, \\ 0 & s < 0. \end{cases} \qquad \delta(s) = \frac{d}{ds} H(s) \tag{4.7}$$

Each term of the Equation 4.3 can be expressed in the level set function as below:

$$\begin{aligned} \boldsymbol{Length}(C) &= \boldsymbol{Length}(\Phi = 0) \\ &= \int_\Omega |\nabla H(\Phi(x,y))|\, dx\, dy = \int_\Omega \delta(\Phi(x,y)) |\nabla \Phi(x,y)|\, dx\, dy \end{aligned} \tag{4.8}$$

$$\boldsymbol{Area}(C) = \boldsymbol{Area}(\Phi = 0) = \int_\Omega H(\Phi(x,y))\, dx\, dy \tag{4.9}$$

$$\int_{\text{inside } C} |f(x,y) - c_1|^2\, dx\, dy = \int_\Omega |f(x,y) - c_1|^2 H(\Phi(x,y))\, dx\, dy \tag{4.10}$$

$$\int_{\text{outside } C} |f(x,y) - c_2|^2\, dx\, dy = \int_\Omega |f(x,y) - c_2|^2 (1 - H(\Phi(x,y)))\, dx\, dy \tag{4.11}$$

Combining Equations 4.8, 4.9, 4.10 and 4.11, the level set formulation of the Chan-Vese model is derived as:

$$\begin{aligned} F_{CV}(c_1, c_2, \Phi) = \mu &\int_\Omega \delta(\Phi(x,y)) |\nabla \Phi(x,y)|\, dx\, dy + \\ \nu &\int_\Omega H(\Phi(x,y))\, dx\, dy + \\ \lambda_1 &\int_\Omega |f(x,y) - c_1|^2 H(\Phi(x,y))\, dx\, dy + \\ \lambda_2 &\int_\Omega |f(x,y) - c_2|^2 (1 - H(\Phi(x,y)))\, dx\, dy \end{aligned} \tag{4.12}$$

After initializing a level set function $\Phi(x,y)$ which is smooth enough, the minimization problem is solved numerically by evolving the function Φ in each iteration. In this study, a circular function and a chessboard function as initial level set functions (shown in Figure

4.3) were tested. Results showed that both types worked well for the given images as long as enough iterations were provided.

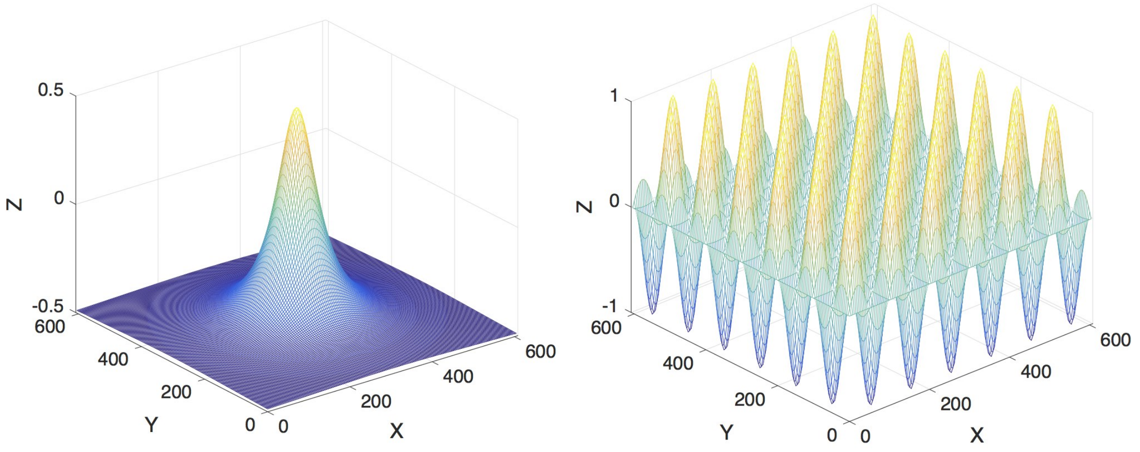

(a)

(b)

Figure 4.3: Two types of the initial level set function used in this study with their zero-crossing as (a) a circle of radius 50 pixels, and (b) a chessboard with a square width of 50 pixels.

Fluorescence image processing routine

The entire processing routine for each raw fluorescence image is divided into five major steps as illustrated below in Figure 4.4.

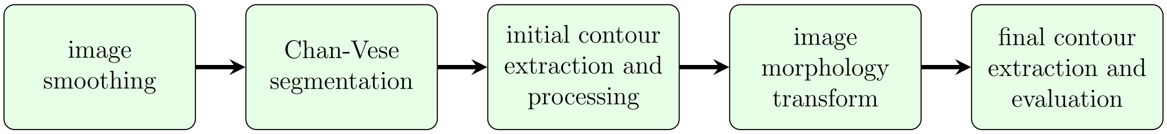

Figure 4.4: Fluorescence image processing routine.

Smoothing: For reducing the pixel noise, an initial image-smoothing step is performed using a median filter of a window size 3x3 pixel. Because the fluorescence image taken by the mmSFE contains a significant amount of salt and pepper noise (impulsive noise), and median filtering is less sensitive than linear techniques to extreme changes in pixel values. The median filter is relatively effective when removing such type of noise while still preserving the edge information of an image. The smoothed intensity image serves an input to the next step of the Chan-Vese segmentation.

Segmentation: The segmentation procedure starts automatically with a predefined level set function Φ_0 with its zero-crossing as the initial guess of the contours. In this study, the initial contour is either a circle of radius 50 pixels at the center of the image or a chessboard with a square width of 50 pixels. At each iteration step k, the algorithm updates $c_1(\Phi_k)$ and $c_2(\Phi_k)$, and solves the partial differential equation to obtain Φ_{k+1}. The iteration terminates until the minimum is found (i.e. the L^2 distance between Φ_{k+1} and Φ_k is below a tolerance) or the maximum allowed loop number is reached.

Contour Extraction: The resulting level set function Φ is zero-crossed to achieve gross contours, which might still be noisy due to the insufficient number of iterations. A binary image is created by the extracted contours.

Outlier Removal: Morphology transformations (an opening operation of size 7x7 pixel followed by a closing operation of size 15x15 pixel) are applied to the generated image for outlier removal and final smoothing of the segmented area.

Evaluation: The final contour is extracted from the segmentation image. The average intensity of the area enclosed by the final contour and the average intensity of a 20 pixel-wide contour band outside the contour is computed in the original fluorescence image for T/B ratio evaluation.

4.2.3 Experiments Setup

Mouse brain tumor model

Animal experiments were performed according to the protocol approved by the IACUC of the St. Josephs Hospital and Medical Center (Phoenix, AZ). The mouse brain tumor model was created by injecting GL261-luc2 mouse glioma cells beneath the brain surface of C57bl6 mice [84]. Animal surgeries and mmSFE tumor imaging were carried out on the 15th through the 18th day after implantation allowing the tumors to grow. 5-ALA hydrochloride was injected intraperitoneally 2-6 hours or 24 hours prior to surgery to induce PpIX accumulation in the tumor. Tumor imaging using the mmSFE was performed in-vivo and rapidly after brain removal.

Configuration of the mmSFE system

The mmSFE system uses a short wavelength 405 nm laser for the excitation of the 5-ALA-induced PpIX with a 2.1 mm diameter forward-viewing scope probe. The reflectance and fluorescence light was collected and isolated into three different channels (red, green, blue) of the SFE using different photomultiplier tubes (PMTs). The red channel captures the emission light of 5-ALA-induced PpIX near the main emission peak (634 nm) and out to the minor near-infrared emission. The blue and green channels mainly collect the reflectance and any auto-fluorescence of the scene. The segmentation is performed on the red/fluorescence channel of the mmSFE image. It was noticed that in the collected images, the red spectral channel interfered with the overlapping auto-fluorescence and reflectance in various levels, leading to the low signal to noise ratio in most of the raw fluorescence images.

4.2.4 Results and Discussion

Segmentation of tumor region in fluorescence images

Two types of level set function (a circle and a chessboard, see Figure 4.3) were used as the initial guess. Both approaches worked well if enough iterations were given. The circular level set function converged slightly faster compared to the chessboard function in most of the images. The segmentation routine terminated in this experiment with an L^2 error tolerance of 0.1 or the maximum iteration loop of 50 was reached. The speed of evolution mainly depends on the noise level of the raw fluorescence image (i.e. the SNR in the raw gray image). More iterations are required to reach the same desired error tolerance when segmenting images with lower SNR. Figure 4.5 illustrates partial results starting from an initial input of an RGB mmSFE image.

As shown in Figure 4.5(b), the raw fluorescence image displays relatively high SNR, and thus the segmentation procedure is fast and straightforward, and the segmented region has high confidence for tumor tissue. However, most of the SFE images taken from the mouse brain model in this experiment contained different levels of background fluorescence, which could not be simply filtered by a median filter. In the next part, the noise compensation method to improve the overall SNR of the image before applying the median filtering will be discussed.

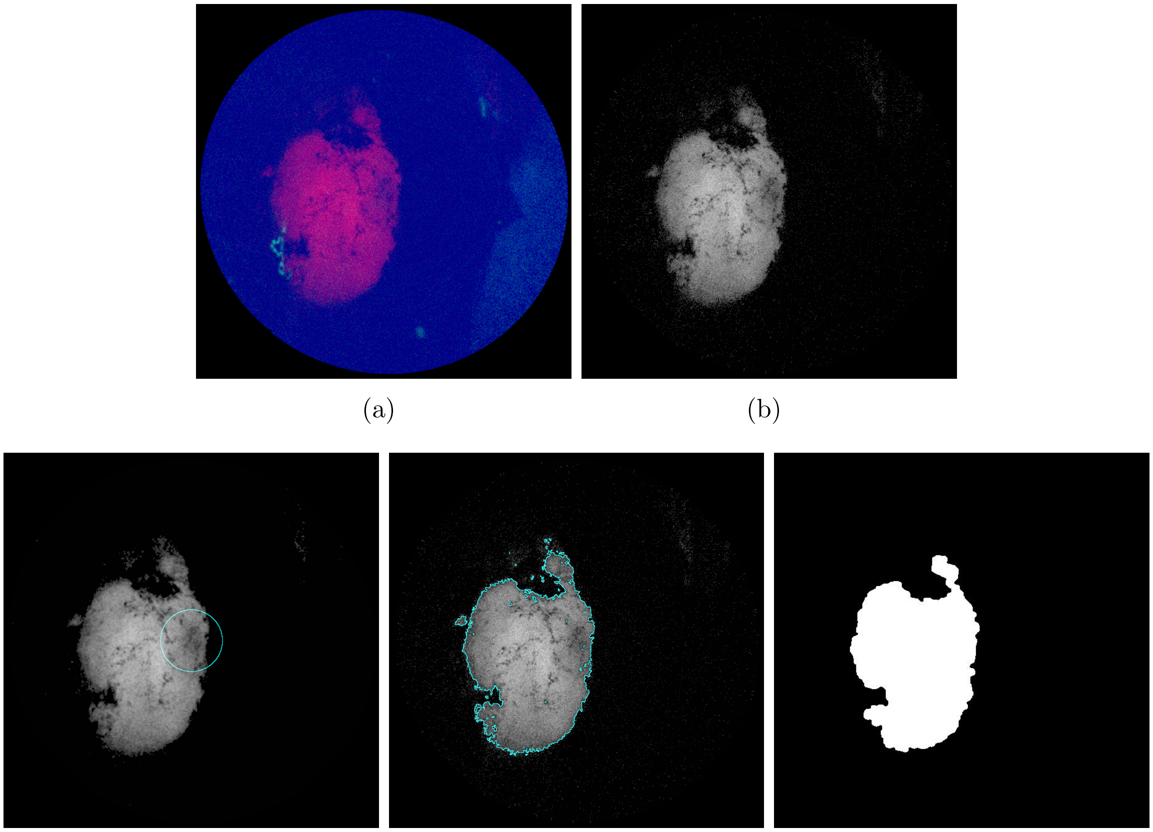

(a) (b)

(c) (d) (e)

Figure 4.5: (a) Initial RGB image from SFE. (b) Red Fluorescence channel of the image. (c) The initial guess of the boundary derived from a circular level set function(4.3(a)). (d) Boundary found after 4 iterations of segmentation algorithm with parameters of $\mu = 1$, $\nu = 125$, $\lambda_1 = 2.0$, $\lambda_2 = 2.1$, $dt = 0.1$, $h = 1$. (e) Further smoothed contour and highlighted tumor region after morphology transformations.

Rejection of light disturbance and enhancement of the signal to noise ratio

Background fluorescence in medical imaging comes from a variety of sources. The major external source is related to the imaging instrument setup and imaging parameters, such as the light from the excitation source, imaging distance, camera noise and environmental light. Another source is mainly due to the auto-fluorescence of the tissue samples or the fluorescence resulting from the fluorophores not bound to specific targets. In this experiment, we observed both types of background fluorescence in the SFE image data. An artificial source of fluorescence noise is from strong spectral fluorescence that occurs when the scanning laser illumination strikes the wet and shiny surface of the brain and reflects directly onto the six 0.5 mm diameter optical fibers. These fibers collect and return the light to the color separation system and fluorescence filters used in the green and red channels. The more intense excitation light does produce a higher number of photons leaking through the laser rejection filters, resulting in an apparent fluorescence signal (Figure 4.7).

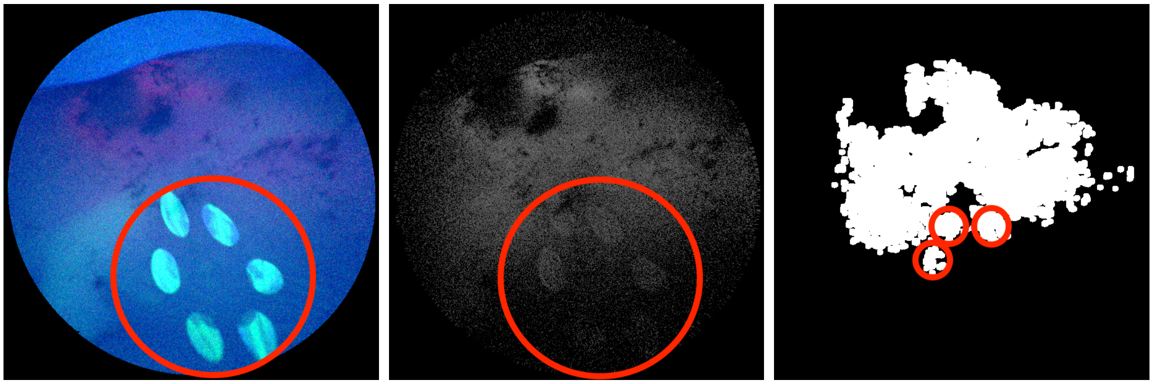
(a) (b) (c)

Figure 4.6: (a) RGB SFE image with light disturbance from the excitation source (marked by the red circle). (b) Red channel fluorescence image with background fluorescence from the excitation source. (c) The segmented region contains the inaccurate classification of the target. Red circles denote the segmentation from background fluorescence.

Figure 4.6(a) and 4.6(b) show that both the original RGB SFE image and the red fluorescence image contain the reflection from the laser source, which leads to the inaccurate identification of the tumor region in the segmentation step as indicated in Figure 4.6(c). It is observed that both the blue (Figure 4.7(a)) and green channel (Figure 4.7(b)) of Figure 4.6(a) contain the saturated reflection of the laser light, which is also partially collected by the red channel (Figure 4.7(c)).

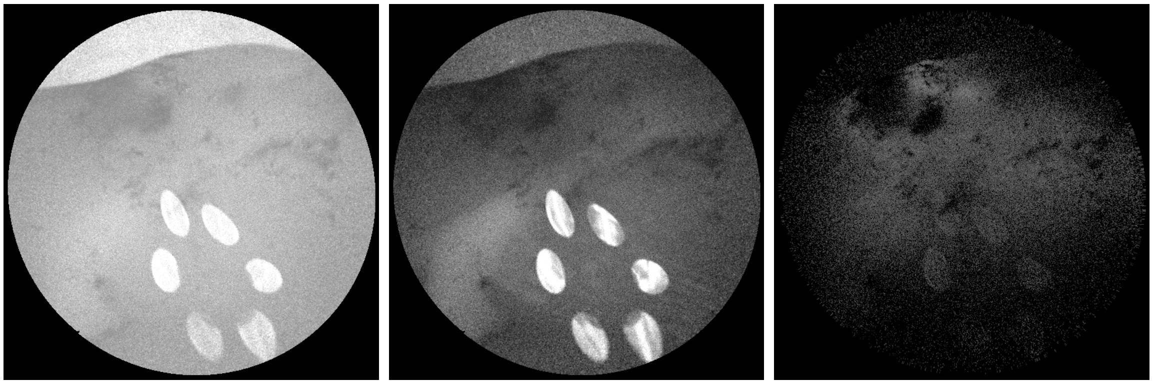
(a) (b) (c)

Figure 4.7: Signal intensity of Figure 4.6(a) in each channel: (a) Blue channel, (b) Green channel, (c) Red channel.

To mitigate the signal crosstalk between different channels, a correcting factor is derived for enhancing the image contrast and mitigating the reflection and auto-fluorescence in the red channel. The correcting factor is defined as the intensity ratio between the red channel and the other channels, given as follows:

$$hannf_{CF} = \frac{f_R(x,y)}{bf_B(x,y) + gf_G(x,y)} \tag{4.13}$$

where b and g are weighting factors for the signal intensity in the blue and green channel, $f_B(x,y)$ and $f_G(x,y)$ respectively. This study empirically picks $b = 0.7$ and $g = 0.3$. The red spectral signal is the multiplied by this correction factor, given as:

$$f_R(x,y) = f_R(x,y) \cdot f_{CF} \tag{4.14}$$

Figure 4.8 below shows the processed fluorescence image (Figure 4.8(a)) and its segmentation (Figure 4.8(b)) of the target region indicating more confident identification compared to the previous result (Figure 4.7(c)). The ratio between the average intensity of the fluorescence and standard deviation of the background improved from 5.89 dB in Figure 4.7(c) to 7.50 dB in Figure 4.8(a) based on the industry standard 10 log rule.

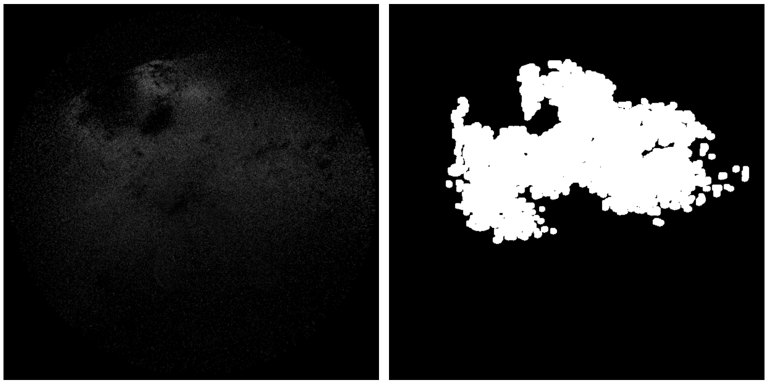
(a) (b)

Figure 4.8: (a) Red fluorescence image after correction. (b) Segmentation of the improved image.

Target to background ratio

The background region size is set as 20 pixels outwards from the presumable tumor contour [92]. The ratio between the average tumor intensity and background intensity in the corrected red channel is computed as T/B ratio. Figure 4.9 illustrates the mask of the target (white region) and background (gray region, 20 pixels in width) from the segmentation.

T/B ratio was analyzed in 30 images of mouse tumors taken by SFE, the average and standard deviation of the T/B ratio of 30 image segmentations were 2.87 ± 1.08 (range of 1.95 - 6.92). This result approaches the T/B ratio observed in a commercial bench-top animal in-vivo spectral imaging instrument IVIS® (PerkinElmer, MA) for PpIX in the mouse brain tumor, average and standard deviation are 4.81 ± 0.92 [93]. A direct comparison of the

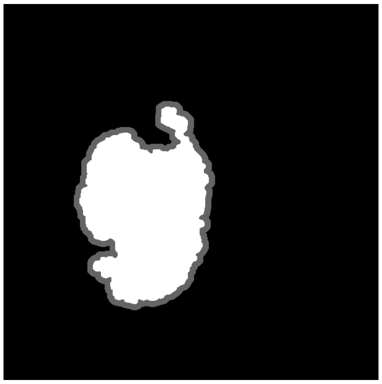

Figure 4.9: Mask of the target (white) and background (gray) used for T/B ratio computation.

tumor/background (T/B) ratio is difficult since the experiment setups were different, and the reported T/B ratio was calculated for the standard ROI versus contralateral brain, as opposed to the nearby brain in this study. Nonetheless, the results indicated a certain level of reliability of the segmentation.

As found in the previous section, the red fluorescence channel is often confounded with auto-fluorescence and strong reflections, which reduces the overall image quality. The compensation method proposed above not only improved the over all SNR of the image but also improved the T/B ratio of the segmented region as the target signal was enhanced while the background noise was suppressed. The T/B ratio from 5 tumor-specific fluorescence images showed an average of 17% improvement after applying the image correction.

The segmentation and noise reduction methods discussed in this section for T/B ratio classification are solely based on the captured light signal. However, in clinical settings, the T/B ratio also highly depends on the concentration level of PpIX, which correlates with histologic grades of malignancy in human gliomas [94]. It is found that in the mouse brain model used in this experiment, the accumulation level also varies in different regions of the brain. Some brain areas showed increased amount of non-specific accumulation of PpIX in normal brain tissue. Such areas were detected in the SFE image as well, with a T/B ratio as high as 2.94 for the areas with the highest intensity. Figure 4.10 shows the detection of the non-specific accumulation of PpIX in normal brain tissue. The segmentation results of this study need to be further confirmed by surgeons and validated with histology to provide correlation with verified tumor cells versus normal brain cells.

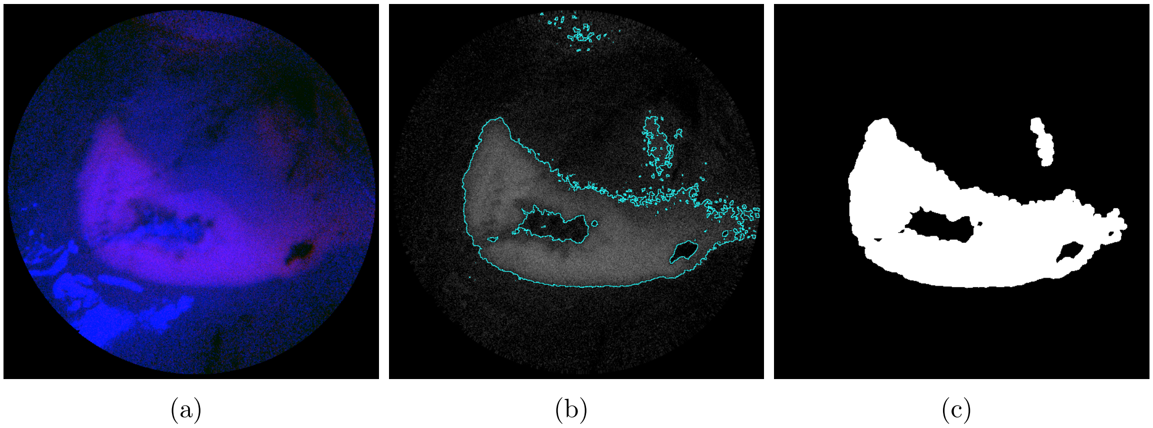
(a) (b) (c)

Figure 4.10: Detection of the non-specific accumulation of the PpIX. (a) Initial RGB SFE image indicating non-specific accumulation. (b) Segmentation of the red/fluorescence channel. (c) Finalized segmentation mask.

Processing speed

The processing algorithm is implemented in C++ using the OpenCV library [76]. For noisy images, a larger number of iterations are required to get reliable segmentation, which is linear with the total processing speed. The average processing time of 30 images with an image resolution of 608 x 608 pixel is ca. 0.65s/image when allowing maximal 10 iterations. The speed was measured on a Windows 10 system of 16 GB Memory and Intel i7-2.8GHz-CPU. This speed can be further improved by enabling GPU computation at each numerical iteration, which is linear with the size of image pixels (608 x 608 pixels for the SFE images).

4.2.5 Conclusion and Future Work

This section demonstrates that the proposed algorithms can be used for tumor boundary identification in 5-ALA-induced-PpIX fluorescence images with quasi-real-time performance. Strong reflections and auto-fluorescence are mitigated in the fluorescence image to achieve robust automatic extraction of the fluorescence boundary. Both the processing speed and the robustness when dealing with low SNR images indicates the potential to integrate with automatic robotic residue brain tumor resection. T/B ratio as a threshold value has reliably marked the tumor tissue boundary in both animal tumor models [93] and early stage human cancers [92] with a strong histopathological correlation. As follow-up work, the histopathology testing will be conducted as ground truth for validating the reliability of the segmentation for the purpose of residual brain tumor clean-up. Moreover, imaging with NIR biomarkers such as “Tumor Paint” will be tested and compared.

4.3 Tumor Localization in 3D Space

In the previous steps, a set of points that represents the surface geometry of the surgical cavity is created and segmentation of the tumor region in the 2D fluorescence images is achieved. The goal of this step is to recover 3D point-clouds, $\boldsymbol{P_t}$, that represent the tumor residues, from SFE poses, 2D pixel segments, $\boldsymbol{P_{pixel}}$, and a 3D point-cloud of the surgical cavity, $\boldsymbol{P_s}$ from the last step. The physical relationship of these input parameters is depicted in Figure 4.11.

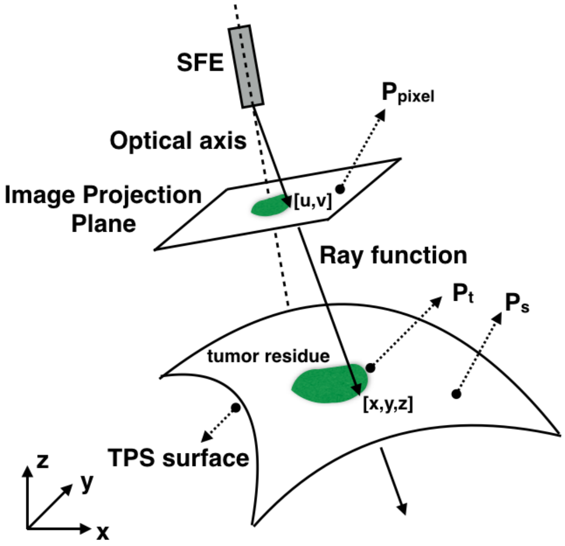

Figure 4.11: SFE pinhole camera model and relationship to the 3D objects.

This procedure is further divided into four steps: 1) create the mathematical surface model from $\boldsymbol{P_s}$ using Thin Plate Spline (TPS) interpolation. 2) determine the ray function for each segmented tumor pixel. 3) compute the intersection point between the ray function and surface model. 4) cluster point-clouds from each image segment. Figure 4.12 describes the block diagram of tumor residue localization. In the following, details of each step are explained.

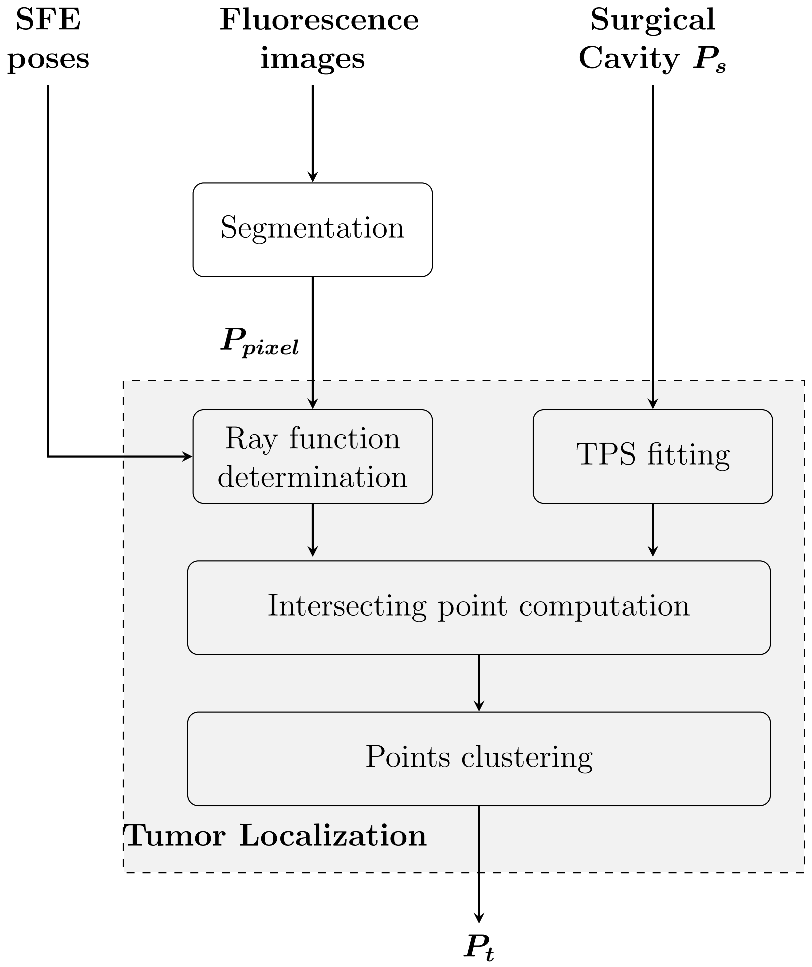

Figure 4.12: Block diagram for tumor residue localization.

Thin Plate Spline based surface model

Thin Plate Spline (TPS) [95] is a spline-based surface fitting technique. It has been widely used as a non-rigid transformation for shape warping because it is insensitive to the noise of the data set. A physical analogy of TPS is to bend a piece of thin sheet metal. TPS fitting uses a set of weights to describe the smoothness of the fitted surface by minimizing the bending energy. More precisely, the goal is to find a mapping function $\boldsymbol{f} : (x_i, y_i) \mapsto z_i$ from the point set $\boldsymbol{P_s}$ by minimizing the following energy function (Equation. 4.15) such that any arbitrary point on the fitted surface can be computed from the projection on the world X-Y plane of the same point.

$$\begin{aligned} E_{tps}(\boldsymbol{f}) = & \sum_{i=1}^{n} \|z_i - \boldsymbol{f}(x_i, y_i)\|^2 + \\ & \lambda \iint ((\frac{\partial^2 \boldsymbol{f}}{\partial x^2})^2 + 2(\frac{\partial^2 \boldsymbol{f}}{\partial x \partial y})^2 + (\frac{\partial^2 \boldsymbol{f}}{\partial y^2})^2)\, dx\, dy \end{aligned} \tag{4.15}$$

where $\lambda \geq 0$ is a pre-defined regularization parameter that measures the goodness of the fitting. For $\lambda = 0$, the TPS surface is reduced to a plane using least square fitting indicating zero bending energy. λ is empirically set to 1 based on the overall smoothness and fit of the original point-cloud $\boldsymbol{P_s}$.

The coefficients of the mapping function can be solved uniquely in closed-form by inverting a nonsingular matrix of size $(n+3) \times (n+3)$, where n is the number of the points in $\boldsymbol{P_s}$. This operation leads to a complexity of $\mathcal{O}(n^3)$ and becomes slow when the point-cloud $\boldsymbol{P_s}$ gets large. Many studies have reduced the computation cost by different methods, e.g. [96] used a preconditioned conjugate gradient method to solve the system of equations; [97] proposed optimal low rank approximations to TPS that were both computationally efficient and stable. In this study, the QR decomposition in Eigen library [98] is used to perform the matrix inversion. The computation time is about two seconds when solving for about 2000 points, which is still tolerable when compared to executing time of the entire medical procedure.

Determination of the ray function

The physics of SFE imaging is approximated as a pinhole camera model for simplification. Each 3D point in space is projected uniquely on the projection plane at a certain pixel location. From the mathematical relationship, a 3D point representing the tumor cell must lie on the line which connects the camera optical center and the corresponding pixel point on the projection plane as shown in Figure 4.11. The mathematical representation of this line in world frame is defined as a ray function in Equation 4.16.

$$f_{ray}(t) \triangleq \begin{bmatrix} x \\ y \\ z \end{bmatrix} = \begin{bmatrix} x_c \\ y_c \\ z_c \end{bmatrix} + t\boldsymbol{R} \begin{bmatrix} \frac{u-c_x}{f_x} \\ \frac{v-c_y}{f_y} \\ 1 \end{bmatrix} \tag{4.16}$$

where $[x_c, y_c, z_c]^T$ is the location of SFE optical center in world frame. Rotation matrix $\boldsymbol{R}$ transforms a point in SFE frame to world frame. $[u, v]^T$ is the pixel location on the image and $[c_x, c_y]^T$ is the principal point. $[f_x, f_y]$ are the focal lengths along the camera x and y axis respectively.

Computation of the intersection point

The location of a tumor cell in space must satisfy two constraints: 1) ray function and 2) TPS mapping function. For each pixel segmented from the fluorescence image, there is a unique corresponding 3D point in space representing the tumor cells, i.e. the intersection point between the ray function and TPS surface determines the 3D location of tumor cells detected in the endoscopic image. A numerical method is used to search for the intersection point iteratively. The algorithm starts with two initial points on the ray function: SFE position $p_1 = [x_c, y_c, z_c]^T$ and the intersection point between the ray and the world X-Y plane $p_2 = [x', y', 0]^T$. Note that p_1 must not be on the TPS surface while p_2 could be on the surface, in which case the iteration finishes in one loop with p_2 as the result. There are two possible relations regarding the location of these two initial points when not on the TPS surface. A simplified 2D illustration is given in Figure 4.13.

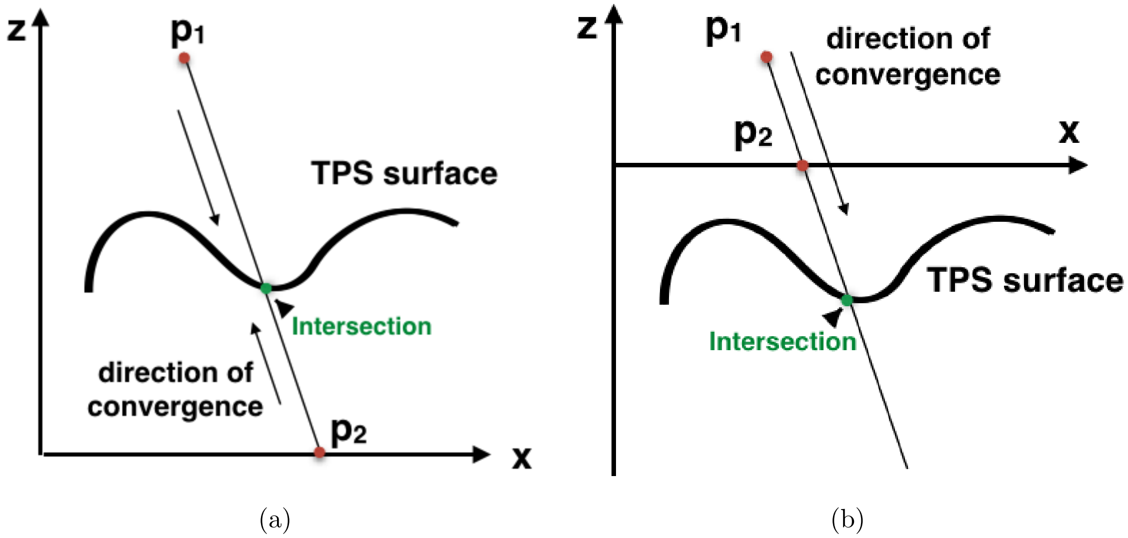

(a) (b)

Figure 4.13: Two possible cases of points p_1 and p_2 with respect to the TPS surface. (a) Case A. (b) Case B.

- **Case A:** two points are located on different sides of the TPS surface (Figure 4.13(a)). In this case, the intersection point is computed by sliding p_1 and p_2 towards each other. The convergence is bidirectional along the ray function. The middle point of p_1 and p_2 will be the intersection point at convergence.

- **Case B:** both points are located on the same side of the TPS surface (Figure 4.13(b)). In this case, the intersection point is found by sliding both p_1 and p_2 towards the TPS surface for one directional convergence at the point p_2. Case B can turn into case A after several iterations if $f'_{ray}f'_{TPS}$ is smaller than zero when evaluated at the intersecting point.

The pseudocode for this iteration algorithm is given in Algorithm 6. The iteration is guaranteed to terminate within a maximal allowed number of loops.

Algorithm 6 Calculation of Intersection Point

```
Require: $p_1 = [x_c, y_c, z_c]^T$ , $p_2 = [x', y', 0]^T$, $\boldsymbol{f_{TPS}}$, $\boldsymbol{f_{ray}}$
if $p_2(z) \approx \boldsymbol{f_{TPS}}(p_2(x), p_2(y))$ then
    return $p_2$
else
    while Case B$(p_1, p_2)$ do
        if $p_2(z) \approx \boldsymbol{f_{TPS}}(p_2(x), p_2(y))$ then
            return $p_2$
        else
            $p_1 \leftarrow p_2$
            $p_2 \leftarrow \boldsymbol{f_{ray}}\Big|_{z=\boldsymbol{f_{TPS}}(p_2(x),p_2(y))}$
        end if
    end while
    while Case A$(p_1, p_2)$ do
        $p_3 \leftarrow (p_1 + p_2)/2$
        if $p_3(z) \approx \boldsymbol{f_{TPS}}(p_3(x), p_3(y))$ then
            return $p_3$
        else
            $p_1 \leftarrow$ Case A$(p_1, p_3)$ ? $p_2$ : $p_1$
            $p_2 \leftarrow p_3$
        end if
    end while
end if
```

Points clustering

From the previous steps, a point-cloud of tumor pieces is obtained in each 2D image if tumor residues are detected through segmentation. Each residual tumor may be scanned multiple times in a sequence of SFE images, and thus multiple point-clouds are generated for the same residual tumor. In this step, these point-clouds of the same tumor piece are clustered into a single point-cloud and the ordered contour of the clustered point-cloud is extracted for the automatic generation of ablation plans afterward. First, a 2D grid map is created on the X-Y plane of the world frame from the point-cloud of the surgical cavity $\boldsymbol{P_s}$. Each point-cloud $\boldsymbol{P_t}$ generated from single fluorescence image is then projected onto the grid map with each grid cell marked as 1 for tumor and 0 for non-tumor. This step can be interpreted as adding a small tumor patch to the 2D binary map frame by frame. A 2D binary map is created after all point-clouds of the tumor are projected (Figure 4.14). The outer contours are extracted since any holes inside each tumor residue will be treated as well. Finally, the generated contours and corresponding grids inside each contour which represent the tumor cells are projected back onto the TPS surface of the surgical cavity. In this step, the number of total tumor residues, the contour and the internal points in 3D space of each tumor residue are retrieved, which are the inputs for the following planner.

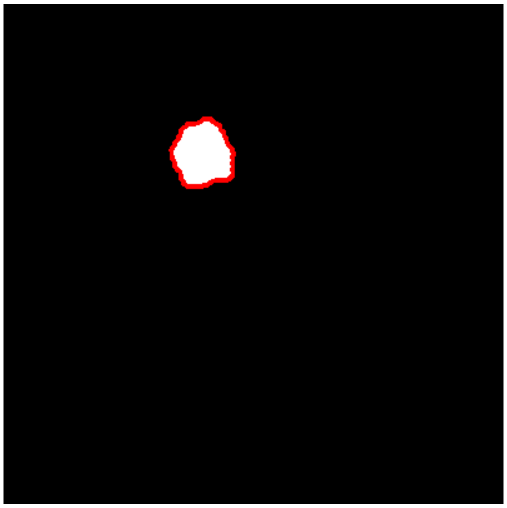

Figure 4.14: 2D binary map of the cavity on the X-Y plane (white pixels represent the tumor) and contour extraction from the binary map.

Chapter 5

AN INTEGRATED ROBOTIC CONTROL FLOW FOR IMAGED-GUIDED BRAIN TUMOR ABLATION

5.1 Control Architecture

The entire software framework for the semi-automated and image-guided residual brain tumor ablation surgery is implemented using the Robotic Operating System (ROS) API [99] on Linux systems. The top layer is a BT that models the medical procedure for brain tumor resection. The middle layer consists of functionality modules that prepare and process the corresponding data requested by the BT. The bottom layer contains a set of control modules which directly control the driver of each hardware system. The three-layer control architecture is depicted in Figure 5.1.

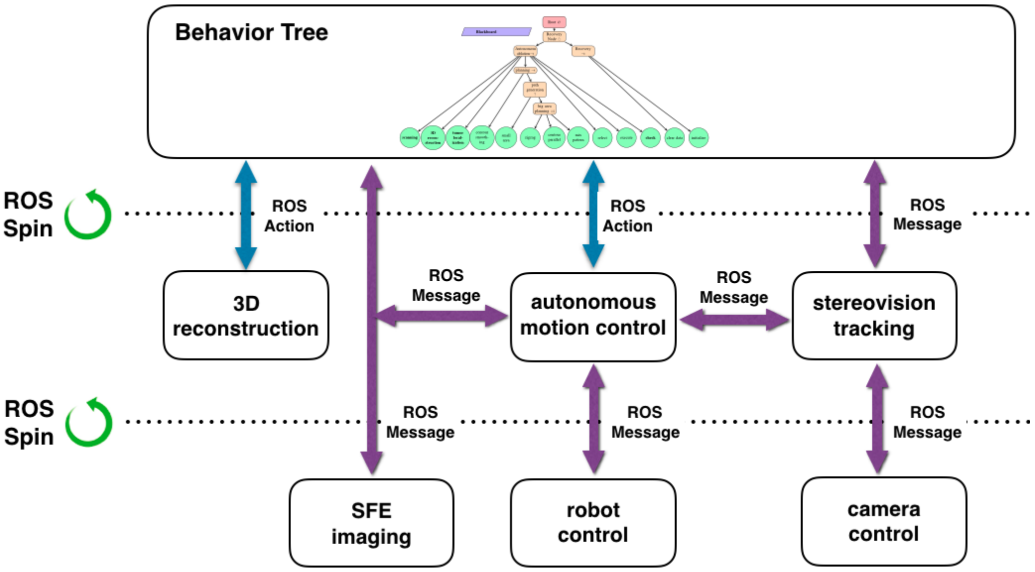

Figure 5.1: Three-Layer Control Architecture: Top layer - BT; Middle layer - functionality modules; Bottom layer - control modules.

The communication among different Linux machines and across different layers is established based on ROS Message and Action protocols. Each module represents one or multiple executables running on three Linux machines. In this study, the SFE imaging module and the robot control module runs on a laptop and a real-time patched Linux machine respectively. The remaining modules run on a third Linux computer. All Linux computers are synchronized in time via the local network with Network Time Protocol (NTP) such that information from different computers can be sorted and handled in time sequence. In the following sections, each module will be discussed in detail from bottom up, except the 3D reconstruction module which is already addressed in the above chapter.

5.2 Hardware Control Modules

The control modules operate on the hardware devices directly. These modules read the devices' sensory information and publish it onto the ROS network, as well as receive messages from upper-level modules and generate corresponding motion/control commands to operate the drivers of the devices. Three modules are implemented/modified for control of the three major devices in this research: the mmSFE imaging system, the stereo camera system, and the RAVEN II$^{\mathrm{TM}}$ surgical robot system.

5.2.1 SFE Imaging

The mmSFE system is controlled from a LABVIEW® interface in a Windows PC. Data transfer between PC and the SFE control box is based on the PCIe serial protocol. In the previous work, manual operations were required on the LABVIEW® interface to save the endoscopic images into the local disk and transfer them later to another computer for further image processing. The SFE imaging module is implemented to overcome this limitation so that all image data processing operation is automated for the medical procedure. This module grabs the SFE images at a certain frame rate using the Epiphan® framegrabber as an intermediate for image data conversion and publishes the pre-processed images onto the ROS network. Figure 5.2 shows the control flow among the different devices such that the

SFE images can be accessed seamlessly by other software modules anytime when needed without manual operation.

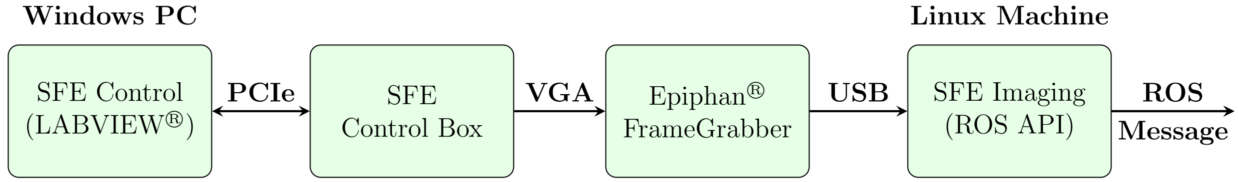

Figure 5.2: Data flow pipeline for automatic image acquisition.

The SFE imaging module reads the raw data from the digitizer via a USB connector and converts the data into an image for further processing. The initial image processing follows five steps:

1. data conversion: This step converts the raw USB data grabbed from the VGA into the OpenCV image matrix format.

2. image cropping: The raw VGA displays each frame at a resolution of 800x600, while each SFE image contains pixel information only in a central circle due to its spiral scan of the illumination optical fibers. To reduce the data size sent to the ROS network, and thus the lower the network latency. The original frame is cropped to the fit a resolution of 600x600.

3. image rotation: The mmSFE system scans the imaged object in a spiral pattern and then maps the collected reflection light into a circular image. The starting scanning point varies randomly every time when the system powers up, and thus, the camera XY coordinates rotate accordingly, causing an undetermined rotation in the image frame. This rotation is compensated every time at the power-up cycle by introducing a rotation matrix along the camera Z axis, which is determined manually after power-up using a reference board.

4. undistortion: The intrinsic parameters of the SFE imaging system are determined using the conventional pinhole camera calibration method, which estimates the focal lengths, principal point, and the distortion parameters (up to the 4th order) using a set of 2D images of a chessboard of known size from different view angles. The SFE image is then undistorted using the estimated distortion parameters.

5. image publishing: This step converts the processed SFE image into a ROS image message and sends the image data together with a timestamp onto the ROS network at approximately 30 fps. This speed is determined by the SFE hardware.

5.2.2 Stereo Camera Control

The stereo camera is a custom built camera pair consisting of two identical low-cost Logitech QuickCam® Communicate Delux webcams. Each camera has a lens with manual adjustable focal length. The maximal resolution of the camera is 1280x960 pixel at 7.5 fps. Both webcams are snapped into a 3D-printed base that can be mounted on an aluminum bar with an adjustable base distance as shown in Figure 5.3. The optical axes of the two webcams are approximately aligned in parallel to provide a reasonable field of view based on the robot workspace.

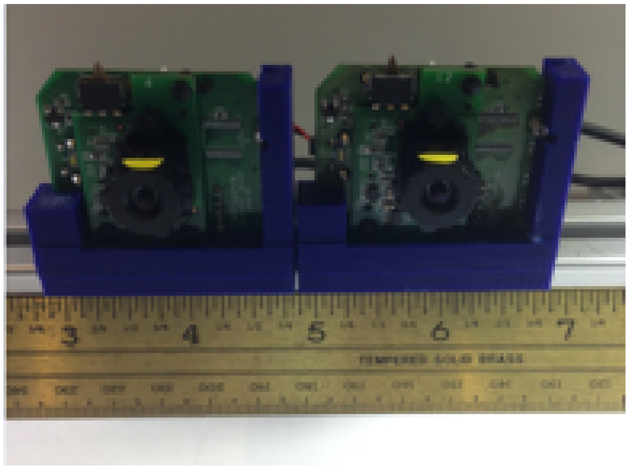

Figure 5.3: Stereo camera system consisting of two webcams and an adjustable mounting.

Each camera is controlled individually by a ROS node using the USB Video Class (UVC) driver. Two ROS nodes for video streaming execute in parallel and the image pairs are approximately synchronized in software using the ROS message filter by grabbing two images from the camera pair which are closest in the timeline. An image rectification is performed to project the two images onto the common image plane using the extrinsic parameters of the camera pair. The rectified image pairs are then published into the network for the tracking algorithm in the vision feedback control. A conventional stereo camera calibration method using a chessboard of known sizes is applied to estimate the camera intrinsic parameters and the extrinsic parameters of the camera pair. The data flow of the camera control module is depicted in Figure 5.4.

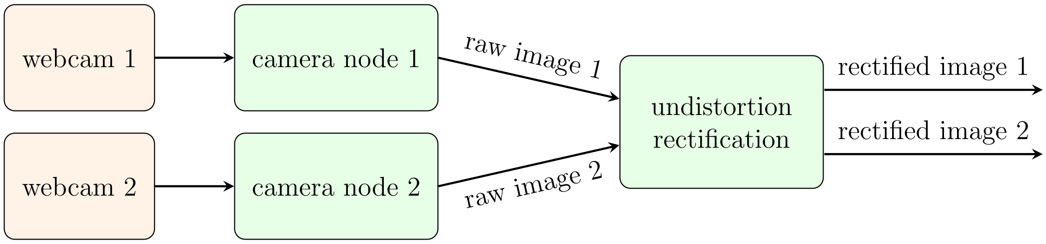

Figure 5.4: Stereo camera control pipeline. Each green node represents an independent ROS node.

.

Although this is a straightforward implementation for multiple camera device control, limitations were found that the ROS image messages take too much network bandwidth causing network congestion or delay, because both the raw images and rectified images are published to the network (1280x960 pixels). Future work on the stereo camera system should investigate the possibility of hardware synchronization and/or multi-thread computing for software synchronization to reduce the ROS network latency.

5.2.3 Robot Control

The Raven II$^{\text{TM}}$ surgical robot is an open-source research platform. The robot consists of two arms which can be teleoperated separately in the master/slave mode by a user from a remote operation station via UDP network packets. To allow the robot to receive motion commands from the ROS network, a ROS message subscriber is added to the robot control. Keyboard operation is added for the convenient switch of the robot runlevels. The received motion increment commands are converted to the desired motion trajectory of the robot end-effector if enabled by the keyboard, otherwise, this increment information will be discarded. Figure 5.5 illustrates the modification of the RAVEN^{TM} II software.

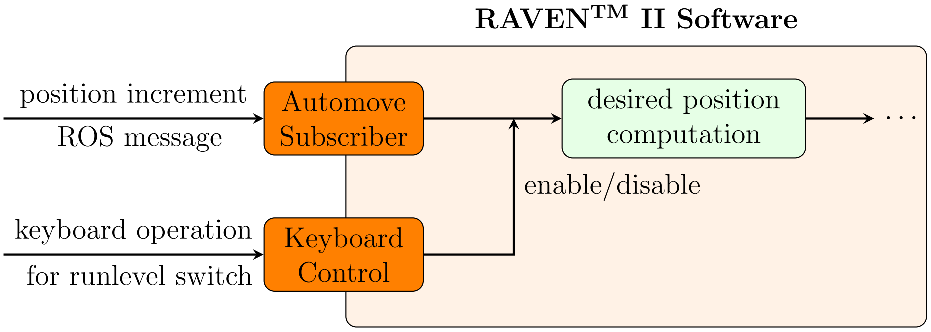

Figure 5.5: RAVEN^{TM} II software modification (orange modules).

5.3 Motion Control with Vision Feedback

From the achieved point-clouds of tumor residues, corresponding ablation plans are generated using the path planner described in Chapter 3. The robot will then execute one of the plans approved by the user (surgeon) through a terminal input. To improve the overall ablation accuracy, two types of vision sources are combined as the feedback to robotic motion control:

1. Stereo-vision for tracking of the robot end-effector position to overcome robot motion inaccuracy.
2. SFE vision for fine adjustment of the ablation path during robotic execution.

This section describes the functional modules of image processing and machine vision as well as the robot motion control with vision information.

5.3.1 Stereo-vision Feedback

Stereo-tracking module

The stereo-tracking module tracks a set of color markers related to the robot position, SFE camera position as well as the ablation tool position using the video images published from the camera control module at the bottom level. Each image pair is synchronized via ROS message filter. The tracked objects are smoothed using two identical Kalman filters in the image pair. The system model is approximated as a linear dynamic model and is given as below:

$$\begin{aligned} \boldsymbol{x_{k+1}} &= \boldsymbol{A}\boldsymbol{x_k} + \boldsymbol{w_k} \\ \boldsymbol{y_k} &= \boldsymbol{H}\boldsymbol{x_k} + \boldsymbol{v_k} \end{aligned} \tag{5.1}$$

where the state vector $\boldsymbol{x_k} = [u, v, \dot{u}, \dot{v}]^T$ with u and v representing the pixel location of the object in the image at time step k. Matrix $\boldsymbol{A}$ is the system matrix and derived as:

$$\boldsymbol{A} = \begin{bmatrix} 1 & 0 & 1 & 0 \\ 0 & 1 & 0 & 1 \\ 0 & 0 & 1 & 0 \\ 0 & 0 & 0 & 1 \end{bmatrix} \tag{5.2}$$

The measurement matrix $\boldsymbol{H}$ is a 4×2 matrix with 1s at its first 2×2 diagonal. $\boldsymbol{w_k}$ is the process noise and is assumed to be zero mean normal distribution ($\boldsymbol{w_k} \rightarrow \mathcal{N}(0, \boldsymbol{P_k})$) with covariance $\boldsymbol{P_k}$ is given as ${\sigma_p}^2\boldsymbol{I}$, where ${\sigma_p}^2 = 0.0001$. $\boldsymbol{v_k}$ is the measurement noise which is assumed to be zero mean gaussian white noise ($\boldsymbol{v_k} \rightarrow \mathcal{N}(0, \boldsymbol{Q_k})$) with the measurement covariance $\boldsymbol{Q_k}$ is given as ${\sigma_m}^2\boldsymbol{I}$, where ${\sigma_m}^2 = 0.1$.

The Kalman filtering works in three steps at each imaging frame cycle. Starting with an initial estimation of the tracked target position $\boldsymbol{x_0}$ in the image, the filter predicts the target position at time step k from k-1, denoted as $\boldsymbol{x_k}|\boldsymbol{x_{k-1}}$. When the image pair arrives at time step k, the target position is measured from the image segmentation, which is denoted as

$\boldsymbol{y_k}$. The system state $\boldsymbol{x_k}|\boldsymbol{x_k}$ is then updated with the measurements and an optimal Kalman gain $\boldsymbol{K_k}$ at time step k. The first two terms of the updated states u_k and v_k are then used for disparity computation. The workflow of the stereo-tracking system is depicted in Figure 5.6. Note that the left and right image processing are synchronized in software using ROS message filter.

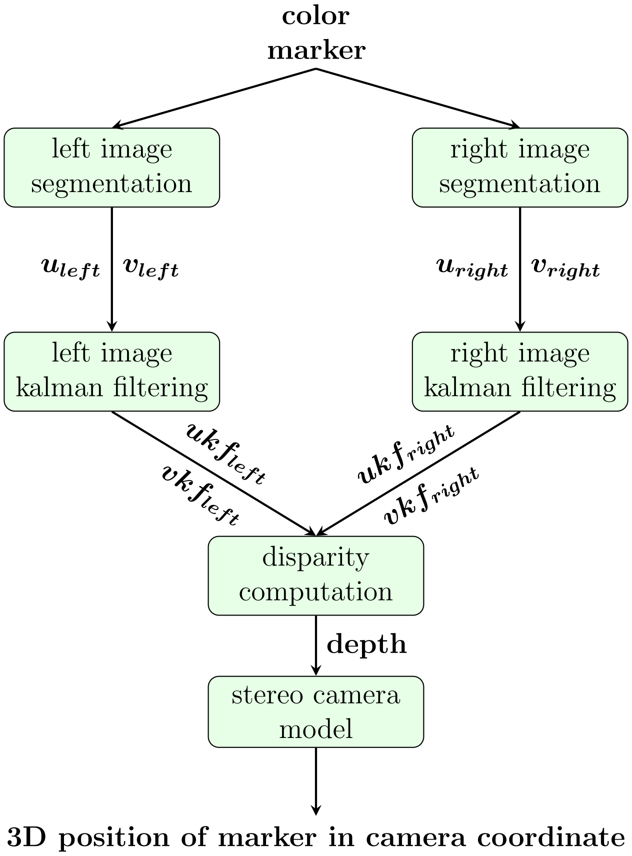

Figure 5.6: Workflow of stereo-tracking module.

This custom tracking system is able to reach an accuracy of ± 0.5 mm when provided with proper light. The performance of the stereo camera is measured by tracking a stationary color marker in 3D space. The position of the marker is recorded using the stereo camera over time and the noise of the tracking system is derived in Table 5.1.

Table 5.1: Noise of the stereo-tracking system

	`x axis`	`y axis`	`z axis`
`Noise [mm]`	±0.05	±0.05	±0.3

Motion with stereo-vision augmentation

The motion control with stereo-vision augmentation is performed in three steps: move, check, correct (Figure 5.7). Robot motion is verified with the stereo-tracking system and corrective incremental movements are generated until the robot accuracy is reached within a defined threshold.

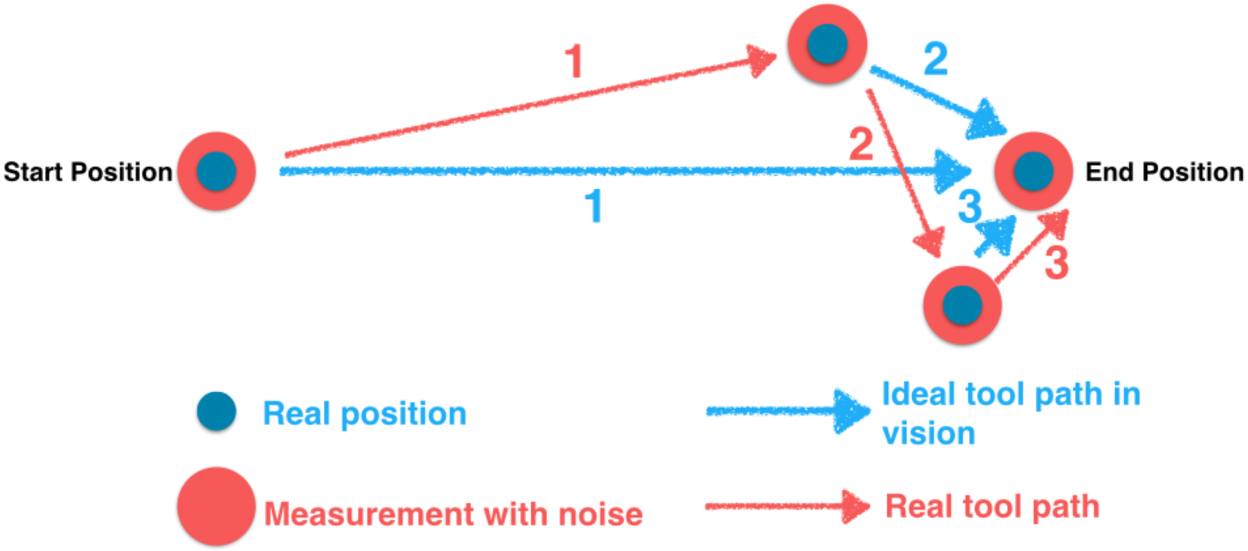

Figure 5.7: Robot position control with stereo-vision augmentation: the actual path deviates from the ideal path due to imprecise angle information of joints. Motion commands continue updating until the end-effector reaches within the tolerance of the destination.

Performance measurement is conducted by commanding the robot tip moving in random directions with random distances. The average of absolute error in the vision system is measured from 40 trials and is listed in Table 5.2.

Table 5.2: Motion accuracy in the stereo-vision system

	`x axis`	`y axis`	`z axis`
`Absolute Error [mm]`	0.248	0.198	0.333

The autonomous motion with stereo-vision is able to control the robot end-effector to move into a small desired region with the target position. Considering the noise distribution of the vision system, the desired region can be narrowed down to the shape of an American football. In this study, a spherical threshold of radius 0.5mm is used for simplicity. Once the end-effector is found inside the desired region, it is hard to differentiate whether the error is caused by control or by vision noise, thus, further motion command stops. Moreover, motion stability is highly related to the noise of the vision system and minimum threshold of the motion control. In some areas of the working space where the lighting is not perfect, the robot may move back and forth and take a longer time to stabilize.

5.3.2 SFE Vision Feedback

The obtained 3D model of the surgical cavity might not be accurate enough due to reconstruction errors in the previous step, which sometimes cause over resection observed in the experiment. Moreover, a slight tissue motion might occur anytime during the ablation. In these cases, the generated ablation path becomes inaccurate. Therefore, fluorescence image based feedback is introduced in the ablation procedure for fine adjustment of the robot trajectory to overcome small model inaccuracy and slight tissue motion. Since the SFE is a 2D imaging device, the path adjustment is performed in the lateral plane such that each via-point in the ablation path is constrained within the tumor area in the 2D image. Figure 5.8 illustrates the process of fluorescence image guided path correction during the ablation.

Before the motion command is sent to the robot, the fluorescence image is analyzed. Path correction is only performed when there is a significant amount of tumor visible in the segmented fluorescence image. The target position of the robot end-effector in world

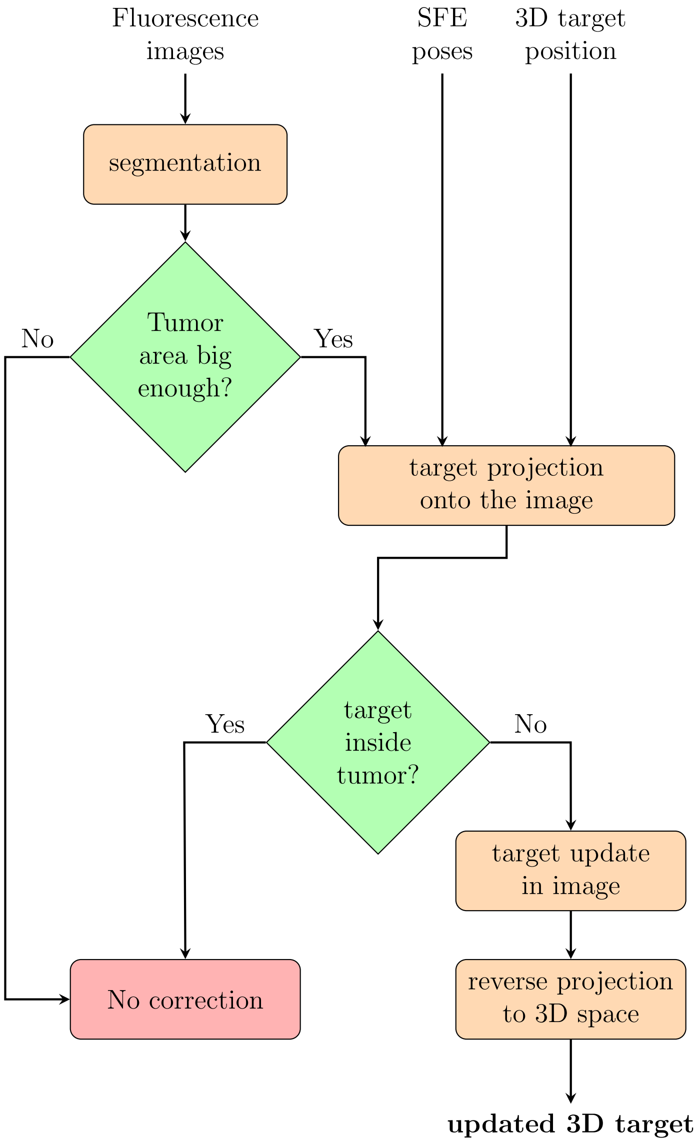

Figure 5.8: Path correction using fluorescence image as feedback.

coordinate system is projected to the current 2D fluorescence frame to check whether the destination is located within the tumor. All targets which are located away from the tumor area will be corrected towards the tumor. Figure 5.9 depicts the three-step correction: 1) project the target 3D point onto fluorescence frame based on the pinhole camera model. 2) compute the centroid of the visible tumor area. 3) compute the intersecting tumor pixel on the line consisting of the centroid and the target pixel. This step is solved by binary search along the line.

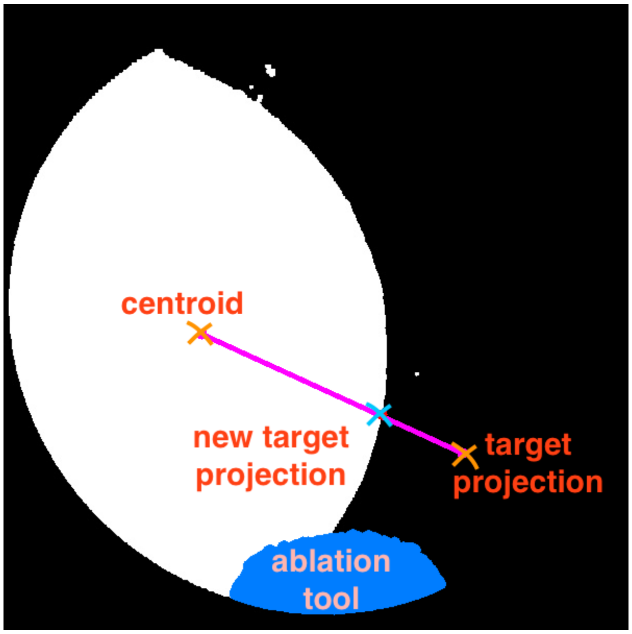

Figure 5.9: 3D target projection and its correction in the segmented SFE fluorescence image. The ablation tool is 7 French ($\approx \varnothing 2.3$ mm) in size.

The intersecting pixel is considered as the adjusted target projection and is reverse-projected back into the 3D world space while preserving the same depth as the old target. Figure 5.10 shows the original ablation path and updated path during the execution when treating a round simulated tumor of $\varnothing 6.35$ mm. Due to the reconstruction error, the generated 3D tumor model is slightly larger ($\approx \varnothing$ 7.21mm) than the actual one, as is indicated in the figure that the original ablation path (red line) covers a larger area than the actual simulated tumor area (green area). The robot adjusts the ablation path during the execution based on the proposed visual servoing algorithm. The updated path (blue line) shows a more accurate coverage of the tumor area compared to the original path, meaning less normal tissue is removed during the ablation.

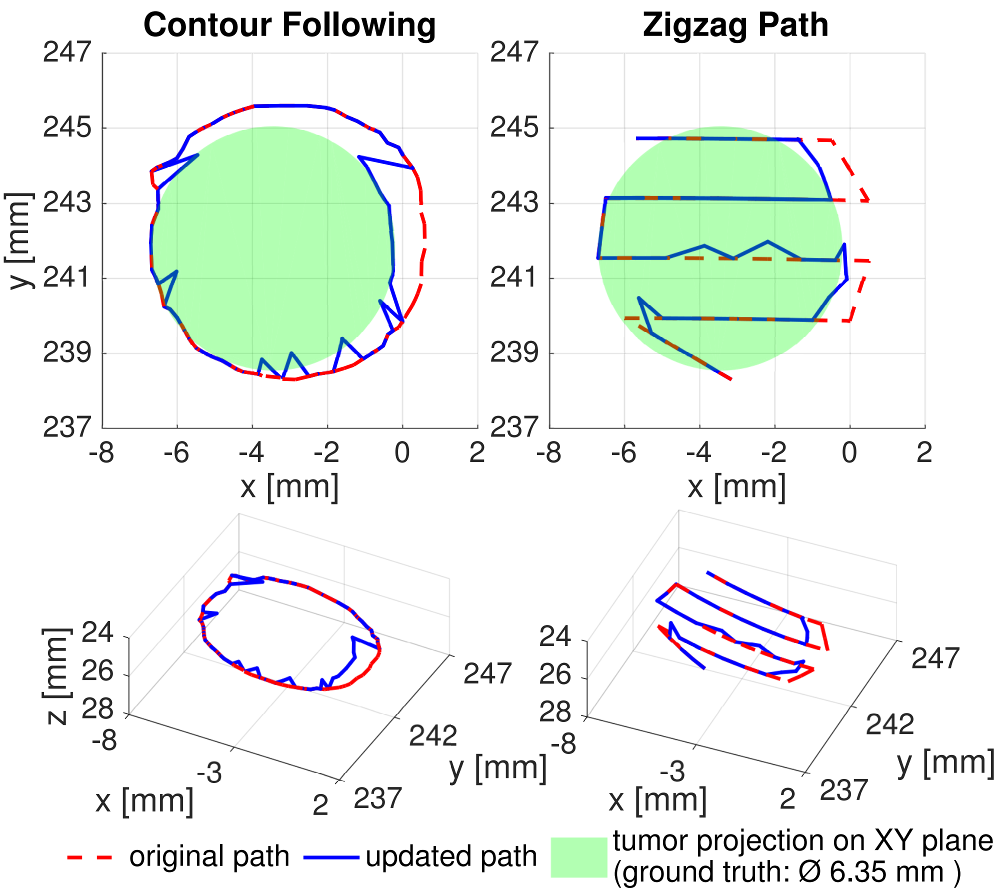

Figure 5.10: Path correction based on real-time SFE vision feedback. Left: Contour following, Right: Zigzag path

It is noticed in Figure 5.10 that the top part of the path is not corrected due to the lack of visual information because the SFE view of the tumor at this region was blocked by the ablation tool. This problem can be solved if using a higher DOF surgical tool at the robot end-effector to guarantee the SFE vision all time.

5.3.3 Autonomous Motion Control Module

This autonomous motion control module in Figure 5.1 combines the two types of vision feedback discussed above and is implemented as a ROS action server, which can be automatically activated when requested by the BT action node from the top control layer. Figure 5.11 describes the scheme of the autonomous motion control with vision feedback incorporated with the BT.

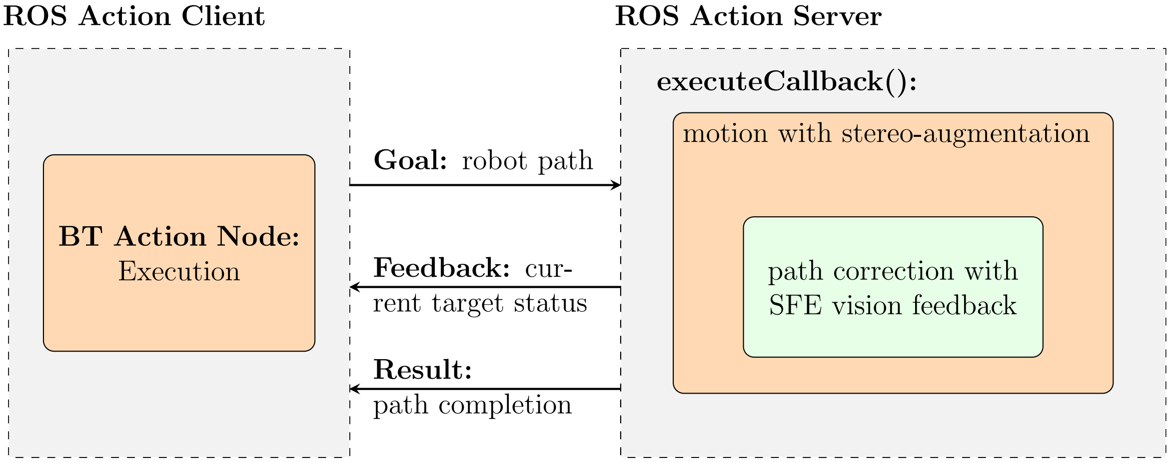

Figure 5.11: Structure of the autonomous motion control module with vision feedback.

The action server starts to execute the task automatically when it receives a goal from the client. Each action goal is a set of points representing a robot path in 3D space to be executed. For each target point in the path, the SFE vision feedback algorithm denoted in Figure 5.8 first checks whether the current target needs to be corrected and updates the target if needed. Then the robot end-effector will be commanded to move to the updated target under stereo-vision augmentation as illustrated in Figure 5.7.

5.4 Action Node Implementation

The BT representation in Figure 2.4 gives an overview of the task flow of this semi-automated medical procedure for residual brain tumor ablation. In this section, the details of each action node implementation and how the information flows between the nodes as well as across the modules will be addressed. Figure 2.4 lists 13 actions in total: **scanning**, **3D reconstruction**, **tumor localization**, **contour smoothing**, **small area planning**, **zigzag planning**, **contour-parallel planning**, **spiral planning**, **select**, **execute**, **check**, and two recovery actions including **blackboard cleaning** and **robot initialization**. The action nodes can be divided into two groups based on the task they carry.

The first type of action node does not perform the task directly within the node, instead, it sends the command/task goal to other modules, and waits for results sent back from other modules when the actual task completes. The BT nodes **scanning**, **3D reconstruction**, **execute** belong to this type and are implemented in the client-server mode using ROS Action Protocol. The action nodes are implemented as a ROS Action Client and the corresponding actual task executors are implemented as a ROS Action Server. The tasks carried out by these action nodes usually take a long time to complete (often hundreds of ticking cycles) and require communication with the hardware. Advantages of this implementation include separating the possible hardware failures from the higher lever decision-making control loop to improve the robustness of the BT. With ROS Action Protocols, the action node receives real-time feedback of the current status of the task from the server, such that the action node can react fast and accordingly if an imperfect sub-result occurs.

The second type of action nodes is mostly data processing nodes or nodes with tasks that can be completed in a single ticking cycle. All the remaining nodes fall into this category. This type of the node executes the task within the node directly, which usually includes three steps: fetching the data from the BT blackboard, processing the data, and updating the blackboard after the processing is done. Special care is taken at each step such as memory checking and pointer verification to avoid a sudden crash of the BT and therefore to improve the overall robustness.

Chapter 6

EXPERIMENT AND RESULTS

This chapter demonstrates the applicability of the algorithms and methods proposed in the previous chapters towards the real clinical application. Laboratory setups are built to validate the algorithms for the automated medical procedure of residual brain tumor ablation. Performance of the integrated surgical robotic system and experiment results are analyzed and evaluated.

6.1 Experiment Setup

6.1.1 Design of A Surgical Phantom

In many medical cases, due to vague symptoms at the early stage, patients are diagnosed with brain cancer only when the tumor is very big - similar to a ping-pong ball size. Therefore, a concave phantom in similar size was handmade from layers of paper to simulate the debulked surgical cavity. A high-resolution brain image from the craniotomy was printed and pasted on the internal surface of the paper cavity. The maximal depth is about 7 mm with a spherical surface curvature of about 20mm as depicted in Figure 6.1. A protective film was then applied to the surface of the phantom to create moisture resistance. To simulate the tumor residues, transparent lotion was mixed with green fluorescence powder, such that this jelly-like mixture can be segmented in visible light, can stick to the wall of the cavity, and can be removed through vacuum suction. In this experiment, the SFE produces images in 3-channel RGB format for 3D reconstruction and tumor segmentation in color space.

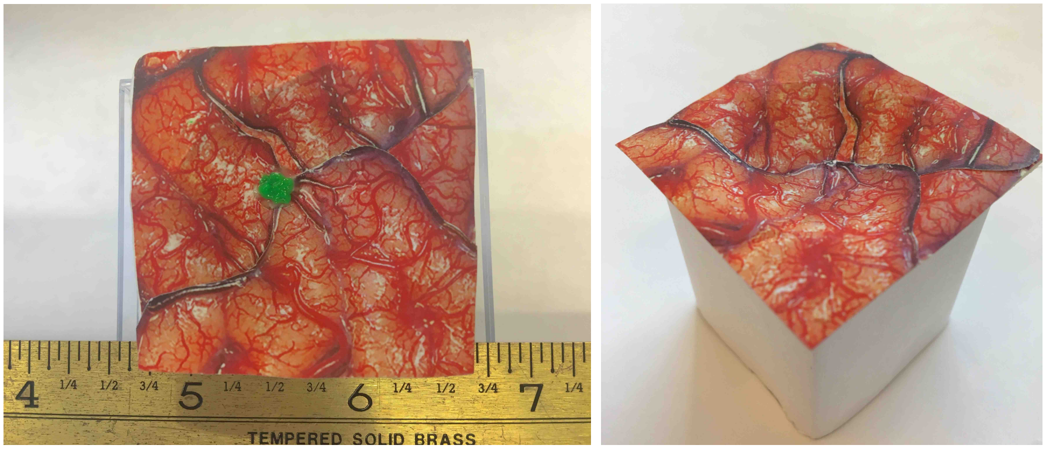

(a)

(b)

Figure 6.1: Simulated surgical phantom. (a) Top view with a simulated tumor residue (green). (b) Perspective view without tumor.

6.1.2 Design of A Tool Adapter

A tool adapter (Figure 6.2) was 3D-printed for attaching a suction ablation tube and the SFE to the robot end-effector. Two types of setups (parallel and angled placement of ablation tool and SFE) were tested. Two set screws were placed perpendicularly for each cylindrical hole to fix the position and orientation of the suction tool and SFE to achieve a minimum bending of the flexible optical fiber. The suction system is able to clear a $\varnothing$3mm circle when placed perpendicularly 1mm above the simulated tumor tissue. The ablation system is depicted in Figure 6.3. For stereo tracking purpose, three blue markers were placed on a planar surface of the tool adapter such that the poses of the suction tool and SFE can be computed through rigid transforms of the markers. This design allows continuous and robust pose acquisition of the tool and SFE when they are deep within the surgical cavity during the treatment process.

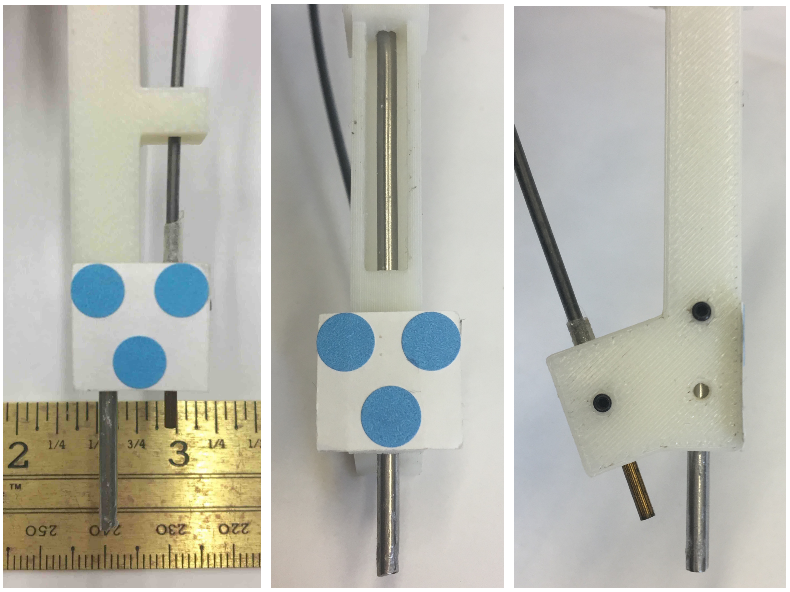

(a) (b) (c)

Figure 6.2: Design of the tool adapter with two setups. (a) Parallel placement design. (b) Angled placement design - front view. (c) Angled placement design - side view.

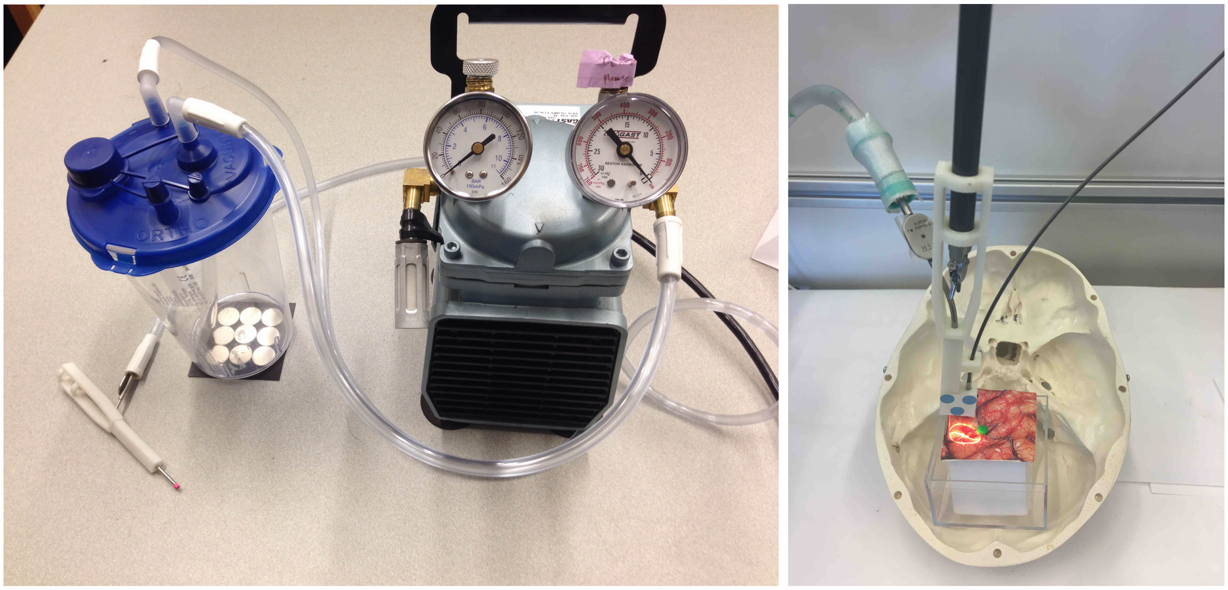

(a) (b)

Figure 6.3: (a) Ablation system overview (from left to right): suction tip with tool adapter, filter, and vacuum. (b) Robot end-effector mount with the simulated surgical phantom.

6.1.3 *Test Platform*

A simulated surgical scenario was built upon the RAVEN$^{\mathrm{TM}}$ II surgical robotic research platform (Figure 6.4). A simulated surgical phantom is placed in the robot workspace. The left arm of the robot is used for the simulated residual tumor resection operation and holds a 7 French suction tool and a ⌀1.6 mm SFE. A stereo camera pair is mounted on the base of the robot to provide color-based tracking of the markers, and hence the pose of tool and SFE. Two LED lights are mounted symmetrically around the workspace to create evenly distributed light for reduction of the tracking noise.

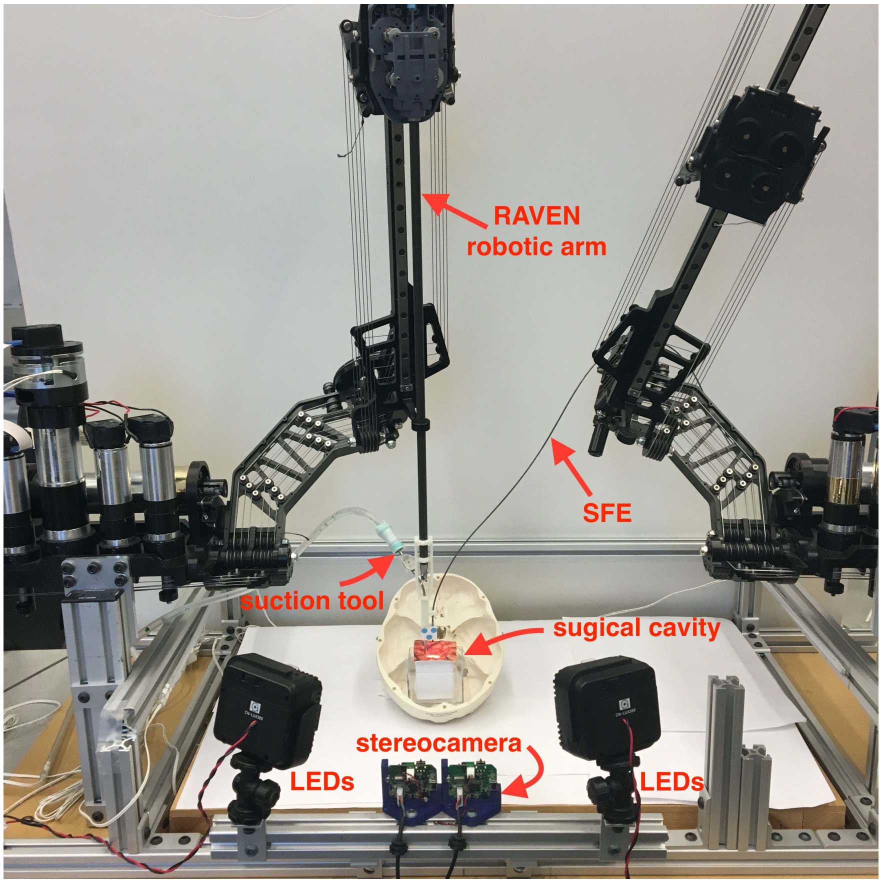

Figure 6.4: Experiment setup with a RAVEN surgical robot, multi-modal SFE, suction tool, simulated surgical phantom and stereo-tracker as well as lighting systems. Ablation system and mmSFE control system are behind whiteboard in this photo.

6.2 Results and Discussion

6.2.1 3D Reconstruction

The proposed ORB feature descriptor in section 4.1.2 was able to match a sufficient number of vascular features between the adjacent scans (Figure 6.5), although the Epiphan® digitizer reduces the image quality significantly. Hence, the generated point-cloud of the simulated surgical cavity was sparse (about 1000 points from 49 images), but dense enough to create a reasonable model of the surface.

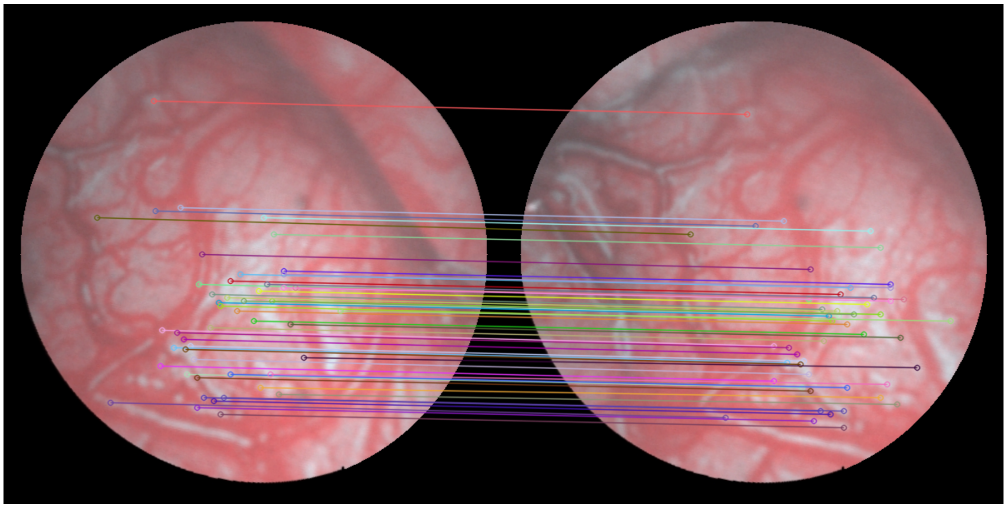

Figure 6.5: Feature extraction and matching between two SFE images.
(Displayed: matching between image index 22 and 23 out of a total of 49 images.)

Figure 6.6 illustrates the point-cloud of the surgical cavity along with the detected tumor residue, marked in green color. The shape and size of the tumor residue in Figure 6.6 match well with the original tumor residue as depicted in Figure 6.1(a). An average tumor size was computed as $\varnothing$ 7.23 ± 0.441 mm from 10 successive trials when using a $\varnothing$ 6.35 mm dot as ground truth.

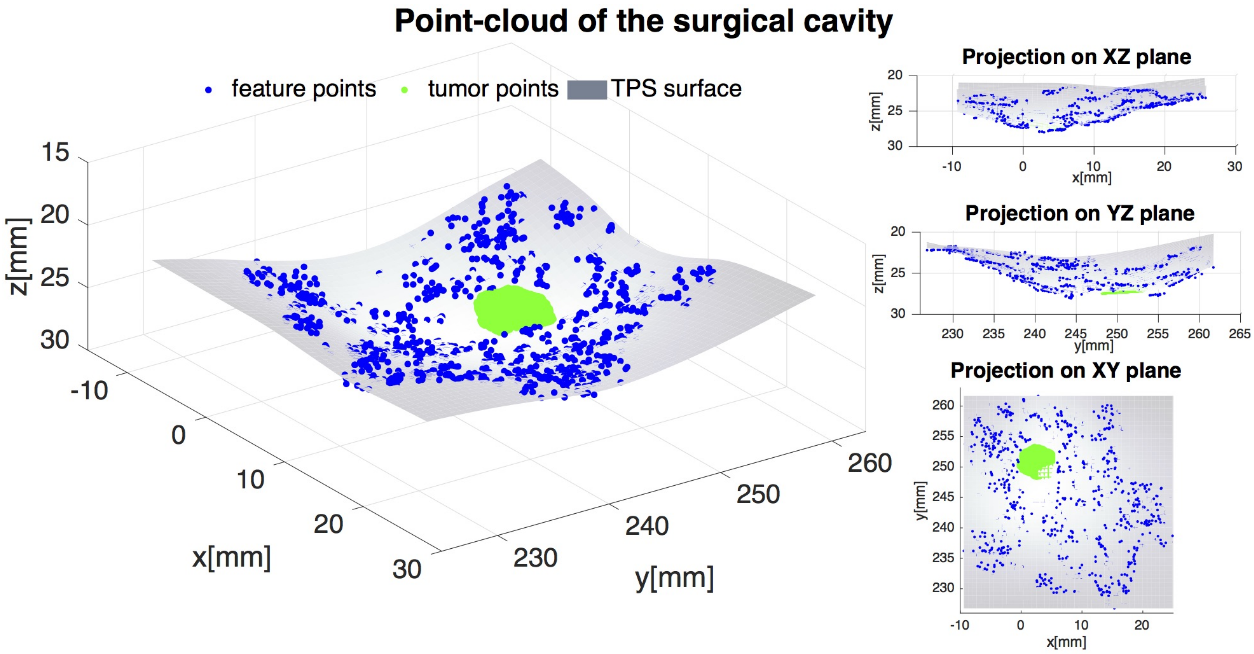

Figure 6.6: The generated point-cloud and the TPS surface of the surgical cavity with the residual tumor.

From a set of test trials, it is noticed that the size error of the tumor residue increases with increasing distance between SFE and surgical cavity due to the increasing triangulation error. Therefore, to achieve a relatively small triangulation error and a robust baseline triangulation, The spacing between each SFE scan was empirically set to 4mm and the distance between SFE tip and the surgical cavity was limited to 15 mm. Moreover, the SFE intrinsic camera parameters play a significant role in the accuracy of the 3D model. Due to the high sensitivity of the SFE, the intrinsic parameters may vary with the force applied on the SFE from set screws and the internal parameter drifting of electronic elements. Hence, at power-up cycle of the SFE system, a manual calibration was executed using SFE control software to reduce the observable central distortion. Multiple conventional calibrations using a checkerboard were performed later and averages of the intrinsic parameters were computed. Radial and tangential distortion of the SFE images was corrected partially using the calibration results. Some of these average values were then fine-tuned based on a set of test runs. Finally, these refined parameters were used for the 3D reconstruction algorithms.

6.2.2 Navigation and Execution Accuracy

The motion control of the suction tool tip and SFE is based on vision feedback and robot inverse kinematics. Direct PID control of desired motor angles is not accurate enough to perform tasks which require sub-mm accuracy. Therefore, the stereo-tracking system consisting of two webcams was introduced to provide the ground truth of tool and SFE poses within half mm precision. Figure 6.7 plots the position of the SFE and suction tool tip together with the generated 3D point-cloud of the surgical cavity during the execution of a planned resection. The suction tool tip was programmed to move 1.5 mm above the phantom surface to avoid direct contact with the phantom surface.

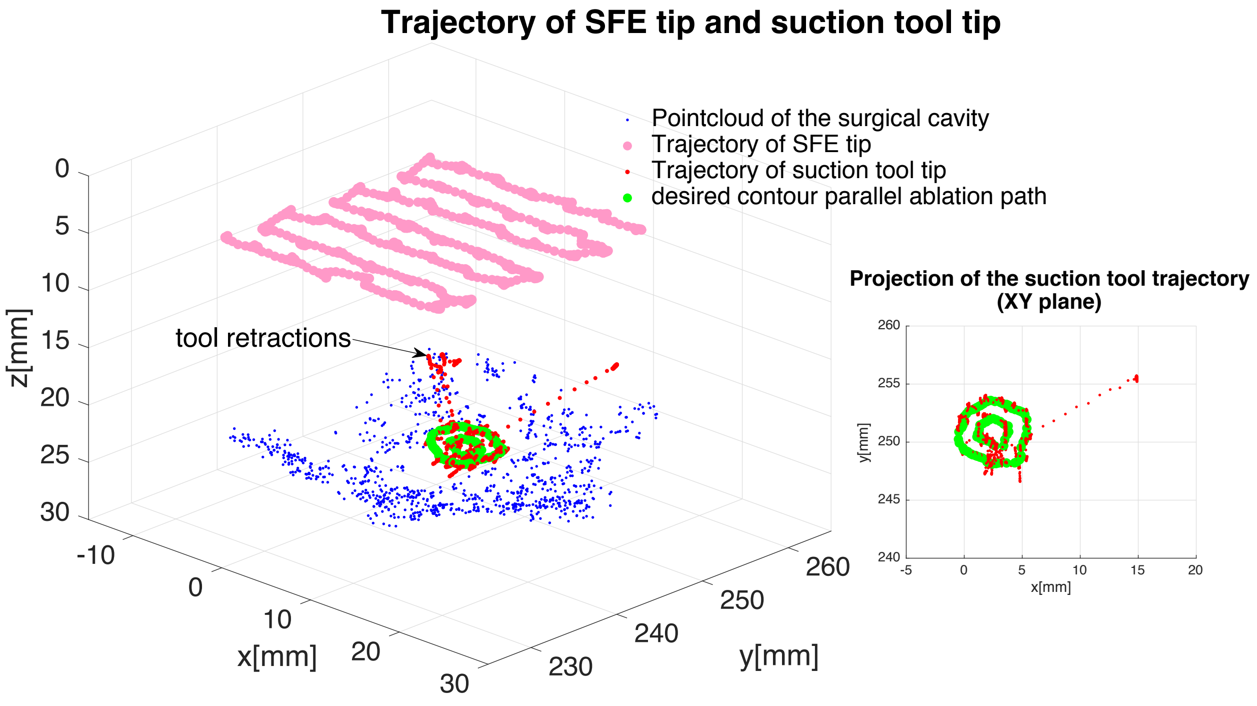

Figure 6.7: Trajectories of suction tool tip (red) and SFE tip (pink) with respect to the 3D model.

It is shown in Figure 6.7 that the tool tip was able to follow the desired treatment path within sub-millimeter accuracy. An enlarged display of each via-point (green) and the robot tip position (red) is presented in Figure 6.8. The spatial root-mean-square (RMS) error between the actual robot motion path and generated path is computed as 0.207 mm in the stereo-vision frame.

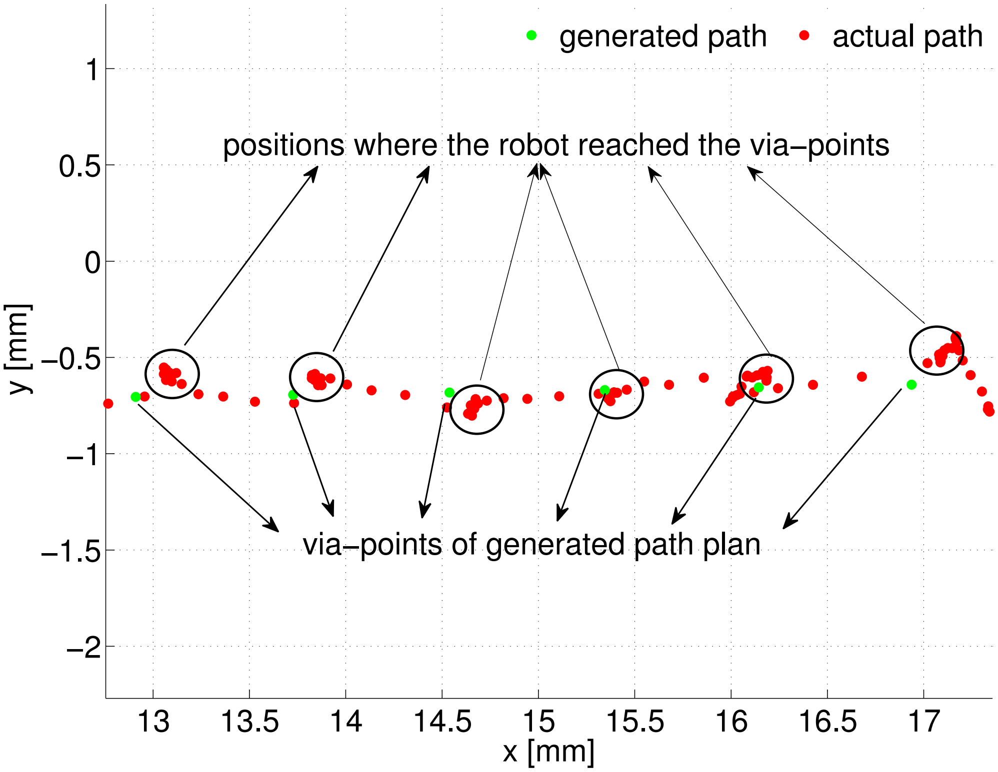

Figure 6.8: Motion error analysis of the robot motion (red) vs. via-points (green) on the X-Y plane of surgical field frame.

6.2.3 Procedure Duration

The total duration of the entire semi-autonomous procedure was about 6 minutes. Table 6.1 lists cpu time used for each subtask, which is run on a Intel® Core™ i7 processor Linux computer with 8 GB RAM.

Table 6.1: Time of each subtask

`Subtask`	`Approx. Time [sec]`
`7x7 raster scanning in 4mm spacing`	196
`3D image reconstruction of 49 frames`	2
`Tumor localization`	3
`Generation of ablation plans`	1
`Plan execution (contour parallel path)`	136
`Result verification via SFE image`	2

Note that most of the time was used for the two robotic interventions: scan and ablation. Due to the motion blur caused by the video digitizer, extra waiting time is required at the point where the SFE saves an image during the scanning procedure. The physical scanning speed can be further increased by upgrading to a high frame rate stereo pair. The current frame rate is 7.5 Hz due to camera hardware limitation. However, the tissue removal process is preferred to keep slow. Slow ablation speed helps the suction tool to remove the tissue thoroughly. Secondly, a slower motion of the tool tip prevents big contact forces to the tissue which may cause tissue damage and other unexpected damage in case of accidental contact on tissue motion. For the surgeon, monitoring a slowly moving ablation process with enough time to fine-tune the automated surgical procedure or halt an undesired procedure with a foot pedal would be advantageous.

6.2.4 Success Rate

A successful trial is defined as when the integrated system detects all tumor residues, cleans them and passes the visual validation. Table 6.2 lists the results from 10 consecutive trial runs. Each trial used one of the four path patterns to ablate the tumor residue based on its size and shape: zigzag, contour parallel, a mix of the both patterns as well as spot-wise suction of small tumors. 7 out of 10 trials were successful. The unsuccessful trials were mainly caused by inaccurate 3D model creation. This is due to several possible reasons. First, the tumor residue is located in a feature-sparse area, which leads to partially inaccurate surface model(#7). Second, the drifting of SFE internal parameters such as the field of view(#9), as well as the error in bundle adjustment lead to the position error of the 3D model, and hence of the tumor residues. Trial #4 and #7 cannot be considered as total failures because the remaining tumor material can be removed in further multiple passes as long as there is no damage to the surrounding healthy brain tissue.

Table 6.2: Results for 10 Trial Runs

`trial #`	`# of residues`	`path pattern`	`S/F`	`fail reason`
1	1	zigzag	✓	
2	1	contour parallel	✓	
3	1	mix	✓	
4	1	mix	✗	residue remained partially uncleaned
5	1	contour parallel	✓	
6	2	contour parallel / small	✓	
7	2	mix / small	✗	smaller residue remained uncleaned
8	2	mix / mix	✓	
9	2	contour parallel / mix	✗	tool tip bumped into the phantom
10	2	contour parallel / zigzag	✓	

6.2.5 *Experiment using Wet Phantom*

To validate the algorithms under a more realistic surgical environment, the phantom was sprayed with water to form a wet surface with strong specular reflections in the SFE imaging (Figure 4.1(a)). A round simulated tumor of ⌀6.35 mm was used as ground truth for comparison. Experiments were performed with and without the specular reflection removal technique described in section 4.1.2.

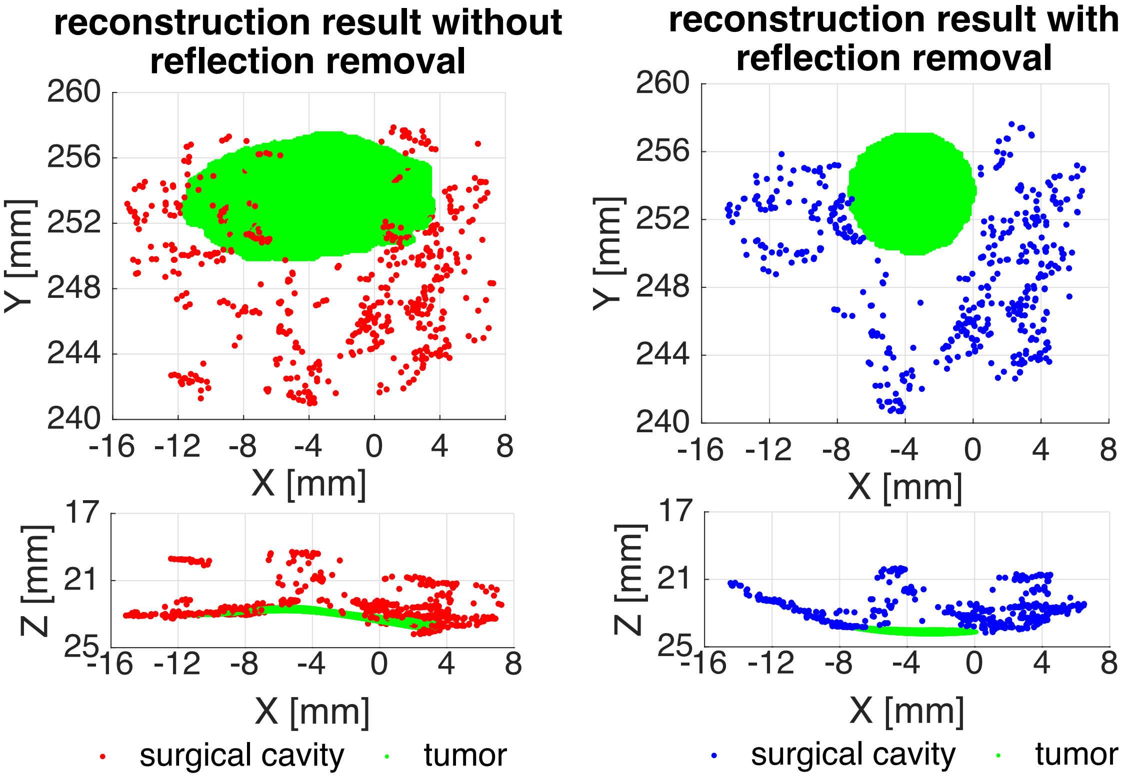

Figure 6.9: 3D reconstruction under specular reflection.

Figure 6.9 shows a significant improvement in the reconstruction accuracy after removal of specular reflection when using the same set of SFE images. The basic shape of both tumor and surgical cavity is more accurately recovered with reflection removal.

6.3 Conclusion and Future Work

This pilot study of the integrated medical robotic system demonstrated the feasibility of supervised automation for brain tumor residue ablation in a simulated surgical cavity. The overall spatial accuracy can be controlled within 1mm with fine tuning of the system parameters. One key function of the described system is its modularity in control architecture, which allows easy modification and integration of sensors and actuators if required for more complex intervention. Although in clinic, neurosurgeries quite often are more sophisticated and require sub-millimeter precision over a long duration, the methods described in this study can serve as an entry point for the further endeavor.

One limitation in the current design of the phantom is that the tumor residues cover some tissue features, which causes small holes in the generated point-cloud of the surgical cavity and therefore may cause partial inaccuracy in the 3D model. However, this limitation may not be expected in the clinical setup using real brain tissue with fluorescence markers, because the vascular features of the tissue with the fluorescence contrast agents can still be detected under multimodal SFE imaging. In the follow-up work, tests with real brain tissue with the fluorescently labeled tumor will be performed to verify this hypothesis. Moreover, another important step towards clinical experiment will be tool interaction with soft tissue. Thresholds such as maximum safe contacting force need to be determined in future exploration. Further developments of the SFE need to be implemented for more robust tissue imaging experiments. These include design improvements, automated feedback control of scanner distortion due to clamping the resonant SFE imager [100], and lossless rejection of specular reflection using spatially separated light collection and detection [101].

Future work also includes design and implementation of an interactive graphical user interface that will visualize the ablation plan. This clinical interface will allow the surgeon to select and define regions, such as a forbidden zone in the 3D model. This zone would be designated to preserve tissue function, which is extremely important to preserve for the patient, and thus the robotic intervention will be prohibited inside these regions.

Chapter 7

FUTURE EXPLORATION OF ROBOTIC SURGERY

This thesis demonstrated a successful laboratory implementation of a semi-automated robotic medical procedure - residual brain tumor resection. The ideas and methods proposed in this thesis contribute directly or indirectly to the development of the image-guided robotic surgery that aims to provide a better or comparable treatment and/or faster recovery time than the conventional surgery. This chapter discusses the open questions for the future exploration of robotic surgery and possible efforts required for moving from the laboratory results towards real clinical applications.

7.1 Supervised Autonomy in Robotic Surgery

During the past decade, tremendous advances in technologies have occurred in the field of surgery. One such technology is the use of surgical robots in medicine. The goal of surgical robots is not to replace the surgeon, but rather, they are designed to assist the surgeons at various levels during the medical operation to provide more accurate diagnoses, more precise intervention, shorter operation duration and faster recovery time in post-surgery. A higher level of robotic assistance is the introduction of a degree of medical automation combined with artificial intelligence and robotics, which might help to provide the patient with better surgical outcomes. It is important to view surgeon's role in autonomous medical procedures not as obsolete, but to see the potential enhancements that the surgical robots together with the surgeon will bring for medicine and science. The surgeon is still required to monitor each aspect of the robotic intervention and be ready to take over anytime if necessary. The autonomy in medical procedures can be presented in various ways, but not limited to:

Semi-Autonomy: Semi-autonomy refers to partial autonomy in medical procedures with surgeon's supervision in the loop as presented in this thesis. In this type of autonomy, the surgeon and the robot work non-concurrently. The surgeon detects the irregular robotic interventions if not detected by the robotic system, and is prepared to take over immediately if such scenario occurs.

Shared Autonomy: In shared autonomy, surgeon operation and robot autonomy are combined concurrently to achieve a certain medical goal together. This can be realized in multiple ways, e.g. the robot and the surgeon work independently or the surgeon teleoperates the robot with a certain degree of autonomy. Shared autonomy requires the autonomous systems to fully understand the surgical site and goal, as well as the operations carried out by the surgeon. It is critical in shared control that the robotic system needs to be able to evaluate/estimate the confidence and danger of the current operation, and even be capable of an automatic takeover. In addition, it is essential that these autonomous systems need to be cognitive, transparent, fluent and smooth in human-robot interaction such that the transition between different operation modes can be seamlessly realized, and thus to reduce the risk during the surgery. All these factors pose unique challenges due to the increased complexity in controls.

Before the actual clinical deployment of the autonomous medical robotic systems, a few open issues of robotic automation in general surgical scenarios are addressed. Possible solutions are discussed.

7.1.1 Bleeding

Bleeding is a general risk for anyone going through a surgery. Blood obscures the surgical cavity intermittently and therefore makes the robotic intervention barely possible in this case. One possible solution would be introducing another robotic tool for blood detection and suction or even manual cleaning by the surgeon in the context of shared autonomy. Such operations may slow down the main robotic intervention but will significantly increase the robustness of the surgical system overall and reduce the risk of surgery. In [102], the authors proposed algorithms based on color information and continuous blood colored regions for automatic bleeding detection in endoscopy video frames in diagnosing gastrointestinal (GI) diseases. Of course, more robust and faster algorithms will need to be explored for real-time blood detection during the surgery, in which case there is a much higher volume of blood. Due to the modular design of the BT based control architecture proposed in this thesis, the integration of such technology and robotic systems is considered straightforward.

7.1.2 Tissue Deformation and Motion

Tissue deformation and motion during the surgery is another common problem occurring during surgery and is considered to be a critical issue in medical automation. Estimation and compensation of periodic tissue motion have been studied by various research groups in beating heart surgery [103,104] and in image-guided radiotherapy of respiratory tumors [105]. Detection of soft tissue deformation has also been intensively studied for surgical simulation and in the laboratory using various signal modalities, such as ultrasound feedback [106], optical feedback [107] and haptic feedback [108]. Challenges still exist for real-time detection of tissue deformation and non-periodic tissue motion in the actual clinical environment, as well as the corresponding robot responses in the presence of such tissue deformation and/or motion. One method proposed in this thesis, introducing the real-time imaging feedback to correct the robotic intervention, might help to mitigate the problem caused by small tissue motion but cannot solve the general problem thoroughly - immediate surgeon's intervention is required in general case.

7.1.3 Emergency Handling

Surgical operations sometimes involve complications that cannot be automatically detected and handled by autonomous systems. Therefore, the surgeon is expected to have full control over the automation and realize the complications soon enough to reduce the risks. Although the proposed BT framework is able to handle possible non-critical outcomes with a recovery node introduced in this thesis, it is not yet programmed to handle most of the emergent complications during the surgery. It is essential in the future to have robotic systems that are able to predict and alert possible complications before they happen based on a large set of vital data collected from the patient and a population of similar patients, and thus allow the surgeon to have enough time to deal with the complications.

7.1.4 Safety Analysis in Robotic Surgery

Probabilistic risk assessment (PRA) is a systematic and comprehensive methodology for evaluation of the risks associated with a complex engineered technological entity, e.g. a power plant or an aircraft [109]. In robotic surgery, a probabilistic risk analysis can be used to predict the uncertainty and severity of the possible unsuccessful robotic interventions during the surgery in terms of probability and magnitude, so that the surgeon can be aware of the possible failures and make decisions about the future robotic interventions based on these quantities. It can also help to establish the safety margin of a robotic medical procedure. Literature in medical risk management [110, 111] discusses the process for conducting the risk assessment using inductive event trees and/or deductive fault trees, which are tree-like structures for risk modeling. An event tree analysis of a robotic medical procedure can be partially incorporated into the BT framework adaptively, by extending each BT node to report the probability of failure occurrence [112] and the severity level of the failure. A comprehensive risk assessment of the autonomous medical system needs to be established in the future work.

7.2 Haptic Feedback

Haptic feedback is another essential aspect in robotic surgery although it is not discussed in this thesis. Current designs and systems for haptic feedback in surgical simulation and telerobotics allow the users to indirectly feel the objects when being manipulated, but are still far from providing the real sense of touch. This remains a significant problem in real clinical applications. Commercial surgical robotic systems focus on providing vivid 3D vision to compensate for the lack of touch, such as the latest da Vinci Xi$^{®}$ surgical system which uses magnified 3D high resolution stereo-vision to allow the surgeon to see anatomical structures in crystal clear definition.

Many research groups have proposed methods to generate the virtual force from visual information [113, 114] and from tissue models [115, 116]. However, haptic feedback is especially critical for surgeons in the absence of good visual information. Further, complete tissue modeling is probably more beneficial for surgical simulation than for real surgery. A considerable amount of research has also focused on designing of force-sensing surgical instruments [117, 118] and force feedback instruments [119]. But the cost of force sensing tends to be high, and other issues such as size, sterilizability, reusability, water resistance, and robustness make the current existing designs hard to meet the surgical requirements. Therefore, force sensing surgical instruments have not yet been seen in the operating room.

Future work in integrating haptic feedback with surgical robots would be easier with a continuous reduction in the cost of force sensing. More studies are needed with efforts from both surgeons and engineers together to contribute for optimal and ergonomic haptic systems in robotic surgery.

7.3 Intraoperative Fluorescence Imaging in Robotic Surgery

Tumor-specific fluorescence-imaging is a rapidly emerging technology in cancer surgery and has shown the potential for accurate visualization of tumors and even residual tumor cells marked by the fluorescence dyes such as ICG or 5-ALA-induced PpIX. Despite the rapid advances in such technology in robotic surgery, e.g. a near-infrared camera was integrated into the da Vinci® Xi System for visualizing blood vasculature in real-time, intraoperative fluorescence imaging is still challenging especially in robotic brain surgery. Such challenges include quantitative identification of the tumor target with respect to the background normal tissue, as the malignant brain tumors are invasive and thus contain diffusive tumor boundaries. The high noise level in fluorescence imaging makes the quantitative analysis even more challenging. The study in this thesis demonstrated that such identification can be measured by T/B ratio, although a threshold of the T/B ratio needs to be further determined alongside with pathology test in the future work. Photobleaching is another critical issue when imaging with fluorophores. Initial studies in imaging of the ex-vivo mouse brain tumors indicated that the 'Tumor Paint' molecular indicator with ICG dye showed a much slower photobleaching rate (ca. 4-5 times slower) compared to the 5-ALA-induced-PpIX as a much lower power excitation laser is required for the ICG to fluoresce. A detailed study regarding the photobleaching rate of the 'Tumor Paint' with respect to the imaging distance, the excitation laser power needs to be conducted in the future for estimating an optimal operation time window. Another challenging aspect is the multimodal display of the fluorescence signal and the reflectance background. The current Firefly Fluorescence Imaging system provided by the da Vinci® Xi Surgical System is able to visualize the target by overlaying the green fluorescence signal on top of gray reflectance images. However, critical color information is missing from the background. In the future work, different methods for multimodality medical image fusion [110, 120] should be investigated for vivid and informative image display. Furthermore, intraoperative imaging in robotic surgery, especially in minimally invasive robotic surgery, requires high camera dexterity, a small camera size and a wild field of view. All these factors result in increasing challenges in designing of medical imaging systems.

7.4 New Designs of the Surgical Robotic Systems

Considering the factors in designing surgical robots, it is a wide field in general which includes but is not limited to the following aspects:

- **procedure-specific robotic systems for different requirements and constraints in different medical procedures as well as improved transparency in human-robot systems.**

  There are some technical factors which need to be considered when designing a surgical robot. Factors related to the systematic design of the robots to fit different operating areas in different medical procedures are of great importance, e.g. design of collision-free mechanisms and safe control for operating in narrow regions. System latency is also a critical factor for safety control especially for robots that can be teleoperated by the surgeon.

- **secure networked robotic systems.**

  With the increased growth of networked systems appearing in the operating room, a crucial problem becomes the security of the cyber-physical systems. Research has shown that a teleoperated surgical robot can be hacked via the network [121], although such potential threat has yet to receive big attention. More security and privacy related issues might appear when the systems are connected to the outside network, e.g. with the increasing deployment of cloud computing for cloud diagnosis or even for online treatment by other experts. Such issues need to be addressed in the future development of surgical robotics.

- **cost-effective robotic systems and smart surgical components.**

  Along with the goal of improved patient care, another important aim of surgical robots would be to reduce costs so that they can benefit more patients over the world. Most of the robotic surgical systems in today's market cost over $1 million for installation plus a considerable amount of maintenance fees yearly, which leads to the fact that lots of patients are not able to receive such medical benefit due to the financial issue. Future development of surgical robotics should focus on cost-effective robotic systems as well as smart accessory instruments that integrate with the surgical robots and extend their functionalities.

BIBLIOGRAPHY

[1] Y. S. Kwoh, J. Hou, E. A. Jonckheere, and S. Hayati, "A robot with improved absolute positioning accuracy for ct guided stereotactic brain surgery," *IEEE Transactions on Biomedical Engineering*, vol. 35, no. 2, pp. 153–160, 1988.

[2] S. D. Herrell, R. L. Galloway, and L.-M. Su, "Image-guided robotic surgery: update on research and potential applications in urologic surgery," *Current opinion in urology*, vol. 22, no. 1, pp. 47–54, 2012.

[3] J. Finkelstein, E. Eckersberger, H. Sadri, S. S. Taneja, H. Lepor, and B. Djavan, "Open versus laparoscopic versus robot-assisted laparoscopic prostatectomy: the european and us experience," *Reviews in urology*, vol. 12, no. 1, p. 35, 2010.

[4] A. M. DiGioia III, B. Jaramaz, and B. D. Colgan, "Computer assisted orthopaedic surgery: Image guided and robotic assistive technologies." *Clinical orthopaedics and related research*, vol. 354, pp. 8–16, 1998.

[5] G. Widmann, "Image-guided surgery and medical robotics in the cranial area," *revolution*, vol. 17, p. 18, 2007.

[6] C. S. Karas and E. A. Chiocca, "Neurosurgical robotics: a review of brain and spine applications," *Journal of robotic surgery*, vol. 1, no. 1, pp. 39–43, 2007.

[7] A. L. Vahrmeijer, M. Hutteman, J. R. van der Vorst, C. J. van de Velde, and J. V. Frangioni, "Image-guided cancer surgery using near-infrared fluorescence," *Nature reviews Clinical oncology*, vol. 10, no. 9, pp. 507–518, 2013.

[8] P. V. Butte, A. Mamelak, J. Parrish-Novak, D. Drazin, F. Shweikeh, P. R. Gangalum, A. Chesnokova, J. Y. Ljubimova, and K. Black, "Near-infrared imaging of brain tumors using the tumor paint blz-100 to achieve near-complete resection of brain tumors," *Neurosurgical focus*, vol. 36, no. 2, p. E1, 2014.

[9] M. Lacroix, D. Abi-Said, D. R. Fourney, Z. L. Gokaslan, W. Shi, F. DeMonte, F. F. Lang, I. E. McCutcheon, S. J. Hassenbusch, E. Holland *et al.*, "A multivariate analysis of 416 patients with glioblastoma multiforme: prognosis, extent of resection, and survival," *Journal of neurosurgery*, vol. 95, no. 2, pp. 190–198, 2001.

[10] J.-C. Tonn and W. Stummer, “Fluorescence-guided resection of malignant gliomas using 5-aminolevulinic acid: practical use, risks, and pitfalls,” *Clinical Neurosurgery*, vol. 55, no. 3, pp. 20–26, 2008.

[11] C. G. Hadjipanayis, G. Widhalm, and W. Stummer, “What is the surgical benefit of utilizing 5-aminolevulinic acid for fluorescence-guided surgery of malignant gliomas?” *Neurosurgery*, vol. 77, no. 5, pp. 663–673, 2015.

[12] M. Veiseh, P. Gabikian, S.-B. Bahrami, O. Veiseh, M. Zhang, R. C. Hackman, A. C. Ravanpay, M. R. Stroud, Y. Kusuma, S. J. Hansen *et al.*, “Tumor paint: a chlorotoxin: Cy5. 5 bioconjugate for intraoperative visualization of cancer foci,” *Cancer research*, vol. 67, no. 14, pp. 6882–6888, 2007.

[13] F. M. Baik, S. Hansen, S. E. Knoblaugh, D. Sahetya, R. M. Mitchell, C. Xu, J. M. Olson, J. Parrish-Novak, and E. Méndez, “Fluorescence identification of head and neck squamous cell carcinoma and high-risk oral dysplasia with blz-100, a chlorotoxin-indocyanine green conjugate,” *JAMA Otolaryngology–Head & Neck Surgery*, vol. 142, no. 4, pp. 330–338, 2016.

[14] B. Hannaford, J. Rosen, D. W. Friedman, H. King, P. Roan, L. Cheng, D. Glozman, J. Ma, S. N. Kosari, and L. White, “Raven-ii: an open platform for surgical robotics research,” *IEEE Transactions on Biomedical Engineering*, vol. 60, no. 4, pp. 954–959, 2013.

[15] C. M. Lee, C. J. Engelbrecht, T. D. Soper, F. Helmchen, and E. J. Seibel, “Scanning fiber endoscopy with highly flexible, 1-mm catheterscopes for wide-field, full-color imaging,” *Journal of biophotonics*, vol. 3, no. 5-6, p. 385, 2010.

[16] D. Hu, Y. Gong, B. Hannaford, and E. J. Seibel, “Semi-autonomous simulated brain tumor ablation with ravenii surgical robot using behavior tree,” in *IEEE International Conference on Robotics and Automation (ICRA)*. IEEE, 2015, pp. 3868–3875.

[17] P. Dario, B. Hannaford, and A. Menciassi, “Smart surgical tools and augmenting devices,” *IEEE transactions on robotics and automation*, vol. 19, no. 5, pp. 782–792, 2003.

[18] G. Moustris, S. Hiridis, K. Deliparaschos, and K. Konstantinidis, “Evolution of autonomous and semi-autonomous robotic surgical systems: a review of the literature,” *The International Journal of Medical Robotics and Computer Assisted Surgery*, vol. 7, no. 4, pp. 375–392, 2011.

[19] ROBODOC, "ROBODOC Pioneering robotic orthopedic products for over 20 years," http://www.robodoc.com/pro_about_history.html, 2015, [Online; accessed 11-May-2015].

[20] W. L. Bargar, A. Bauer, and M. Börner, "Primary and revision total hip replacement using the robodoc (r) system." *Clinical orthopaedics and related research*, vol. 354, pp. 82–91, 1998.

[21] Q. H. Li, L. Zamorano, A. Pandya, R. Perez, J. Gong, and F. Diaz, "The application accuracy of the neuromate robot?a quantitative comparison with frameless and frame-based surgical localization systems," *Computer Aided Surgery*, vol. 7, no. 2, pp. 90–98, 2002.

[22] T. Varma and P. Eldridge, "Use of the neuromate stereotactic robot in a frameless mode for functional neurosurgery," *The International Journal of Medical Robotics and Computer Assisted Surgery*, vol. 2, no. 2, pp. 107–113, 2006.

[23] J. R. Adler Jr, S. Chang, M. Murphy, J. Doty, P. Geis, and S. Hancock, "The cyberknife: a frameless robotic system for radiosurgery," *Stereotactic and functional neurosurgery*, vol. 69, no. 1-4, pp. 124–128, 1997.

[24] A. Wu, G. Lindner, A. Maitz, A. Kalend, L. Lunsford, J. Flickinger, and W. Bloomer, "Physics of gamma knife approach on convergent beams in stereotactic radiosurgery," *International Journal of Radiation Oncology* Biology* Physics*, vol. 18, no. 4, pp. 941–949, 1990.

[25] H. Mayer, F. Gomez, D. Wierstra, I. Nagy, A. Knoll, and J. Schmidhuber, "A system for robotic heart surgery that learns to tie knots using recurrent neural networks," *Advanced Robotics*, vol. 22, no. 13-14, pp. 1521–1537, 2008.

[26] J. Van Den Berg, S. Miller, D. Duckworth, H. Hu, A. Wan, X.-Y. Fu, K. Goldberg, and P. Abbeel, "Superhuman performance of surgical tasks by robots using iterative learning from human-guided demonstrations," in *IEEE International Conference on Robotics and Automation (ICRA).* IEEE, 2010, pp. 2074–2081.

[27] M. Bernardes, B. V. Adorno, P. Poignet, and G. Borges, "Robot-assisted automatic insertion of steerable needles with closed-loop imaging feedback and intraoperative trajectory replanning," *Mechatronics*, vol. 23, no. 6, pp. 630–645, 2013.

[28] S. Patil, J. Burgner, R. J. Webster, and R. Alterovitz, "Needle steering in 3-d via rapid replanning," *IEEE Transactions on Robotics*, vol. 30, no. 4, pp. 853–864, 2014.

[29] B. Kehoe, G. Kahn, J. Mahler, J. Kim, A. Lee, A. Lee, K. Nakagawa, S. Patil, W. D. Boyd, P. Abbeel *et al.*, "Autonomous multilateral debridement with the raven surgical robot," in *IEEE International Conference on Robotics and Automation (ICRA)*. IEEE, 2014, pp. 1432–1439.

[30] C. Coulson, R. Taylor, A. Reid, M. Griffiths, D. Proops, and P. Brett, "An autonomous surgical robot for drilling a cochleostomy: preliminary porcine trial," *Clinical Otolaryngology*, vol. 33, no. 4, pp. 343–347, 2008.

[31] A. Hussong, T. S. Rau, T. Ortmaier, B. Heimann, T. Lenarz, and O. Majdani, "An automated insertion tool for cochlear implants: another step towards atraumatic cochlear implant surgery," *International journal of computer assisted radiology and surgery*, vol. 5, no. 2, pp. 163–171, 2010.

[32] A. Shoulson, F. M. Garcia, M. Jones, R. Mead, and N. I. Badler, "Parameterizing behavior trees," in *Motion in Games*. Springer, 2011, pp. 144–155.

[33] A. J. Champandard, "Understanding the second-generation of behavior trees," http://aigamedev.com/insider/tutorial/second-generation-bt/, 2012, [Online; accessed 11-May-2015].

[34] M. Colledanchise and P. Ögren, "How behavior trees modularize robustness and safety in hybrid systems," in *IEEE/RSJ International Conference on Intelligent Robots and Systems (IROS),*. IEEE, 2014, pp. 1482–1488.

[35] A. J. Champandard, "Understanding behavior trees," http://aigamedev.com/open/article/bt-overview/, 2007, [Online; accessed 11-May-2015].

[36] D. Isla, "Building a better battle: The halo 3 ai objectives system," http://web.cs.wpi.edu/~rich/courses/imgd4000-d09/lectures/halo3.pdf, [Online; accessed 11-May-2015].

[37] C.-U. Lim, R. Baumgarten, and S. Colton, "Evolving behaviour trees for the commercial game defcon," in *Applications of evolutionary computation*. Springer, 2010, pp. 100–110.

[38] Y. Hoshino, T. Takagi, U. Di Profio, and M. Fujita, "Behavior description and control using behavior module for personal robot," in *IEEE International Conference on Robotics and Automation (ICRA)*, vol. 4. IEEE, 2004, pp. 4165–4171.

[39] J. A. Bagnell, F. Cavalcanti, L. Cui, T. Galluzzo, M. Hebert, M. Kazemi, M. Klingensmith, J. Libby, T. Y. Liu, N. Pollard *et al.*, "An integrated system for autonomous robotics manipulation," in *IEEE/RSJ International Conference on Intelligent Robots and Systems (IROS)*. IEEE, 2012, pp. 2955–2962.

[40] A. Marzinotto, M. Colledanchise, C. Smith, and P. Ögren, “Towards a unified behavior trees framework for robot control,” in *IEEE International Conference on Robotics and Automation (ICRA).* IEEE, 2014, pp. 5420–5427.

[41] P. Ögren, “Increasing modularity of uav control systems using computer game behavior trees,” in *AIAA Guidance, Navigation and Control Conference, Minneapolis, MN*, 2012.

[42] A. Klöckner, “Behavior trees for uav mission management.” in *GI-Jahrestagung*, 2013, pp. 57–68.

[43] D. Hu, Y. Gong, B. Hannaford, and E. J. Seibel, “Path planning for semi-automated simulated robotic neurosurgery,” in *IEEE/RSJ International Conference on Intelligent Robots and Systems (IROS).* IEEE, 2015, pp. 2639–2645.

[44] R. Alterovitz, A. Lim, K. Goldberg, G. S. Chirikjian, and A. M. Okamura, “Steering flexible needles under markov motion uncertainty,” in *IEEE/RSJ International Conference on Intelligent Robots and Systems (IROS).* IEEE, 2005, pp. 1570–1575.

[45] R. Alterovitz, T. Siméon, and K. Y. Goldberg, “The stochastic motion roadmap: A sampling framework for planning with markov motion uncertainty.” in *Robotics: Science and Systems*, vol. 3. Citeseer, 2007, pp. 233–241.

[46] V. Duindam, J. Xu, R. Alterovitz, S. Sastry, and K. Goldberg, “3d motion planning algorithms for steerable needles using inverse kinematics,” in *Algorithmic Foundation of Robotics VIII.* Springer, 2010, pp. 535–549.

[47] R. C. Jackson and M. C. Cavusoglu, “Needle path planning for autonomous robotic surgical suturing,” in *IEEE International Conference on Robotics and Automation (ICRA).* IEEE, 2013, pp. 1669–1675.

[48] L. Adhami and È. Coste-Manière, “Optimal planning for minimally invasive surgical robots,” *IEEE Transactions on Robotics and Automation*, vol. 19, no. 5, pp. 854–863, 2003.

[49] D. S. Paik, C. F. Beaulieu, R. B. Jeffrey, G. D. Rubin, and S. Napel, “Automated flight path planning for virtual endoscopy,” *Medical Physics*, vol. 25, no. 5, pp. 629–637, 1998.

[50] M. Bala and T.-C. Chang, “Automatic cutter selection and optimal cutter path generation for prismatic parts,” *The International Journal of Production Research*, vol. 29, no. 11, pp. 2163–2176, 1991.

[51] K. Tang, S.-Y. Chou, and L.-L. Chen, “An algorithm for reducing tool retractions in zigzag pocket machining,” *Computer-Aided Design*, vol. 30, no. 2, pp. 123–129, 1998.

[52] S. C. Park and B. K. Choi, “Tool-path planning for direction-parallel area milling,” *Computer-Aided Design*, vol. 32, no. 1, pp. 17–25, 2000.

[53] A. Zelinsky, R. A. Jarvis, J. Byrne, and S. Yuta, “Planning paths of complete coverage of an unstructured environment by a mobile robot,” in *Proceedings of international conference on advanced robotics*, vol. 13, 1993, pp. 533–538.

[54] Y. Gabriely and E. Rimon, “Spanning-tree based coverage of continuous areas by a mobile robot,” *Annals of Mathematics and Artificial Intelligence*, vol. 31, no. 1-4, pp. 77–98, 2001.

[55] S. X. Yang and C. Luo, “A neural network approach to complete coverage path planning,” *IEEE Transactions on Systems, Man, and Cybernetics, Part B: Cybernetics*, vol. 34, no. 1, pp. 718–724, 2004.

[56] H. Choset and P. Pignon, “Coverage path planning: The boustrophedon cellular decomposition,” in *Field and Service Robotics.* Springer, 1998, pp. 203–209.

[57] B. Sarkar and C.-H. Menq, “Smooth-surface approximation and reverse engineering,” *Computer-Aided Design*, vol. 23, no. 9, pp. 623–628, 1991.

[58] C. H. Bradley and G. W. Vickers, “Free-form surface reconstruction for machine vision rapid prototyping,” *Optical Engineering*, vol. 32, no. 9, pp. 2191–2200, 1993.

[59] T. Varady, R. R. Martin, and J. Cox, “Reverse engineering of geometric modelsan introduction,” *Computer-Aided Design*, vol. 29, no. 4, pp. 255–268, 1997.

[60] A. C. Lin and H.-T. Liu, “Automatic generation of nc cutter path from massive data points,” *Computer-Aided Design*, vol. 30, no. 1, pp. 77–90, 1998.

[61] K. Chui, W. Chiu, and K. Yu, “Direct 5-axis tool-path generation from point cloud input using 3d biarc fitting,” *Robotics and Computer-Integrated Manufacturing*, vol. 24, no. 2, pp. 270–286, 2008.

[62] D. Zhang, P. Yang, and X. Qian, “Adaptive nc path generation from massive point data with bounded error,” *Journal of Manufacturing Science and Engineering*, vol. 131, no. 1, p. 011001, 2009.

[63] http://www.pointclouds.org, [Online; accessed 11-May-2015].

[64] T. Pavlidis, “A review of algorithms for shape analysis,” *Computer graphics and image processing*, vol. 7, no. 2, pp. 243–258, 1978.

[65] S. Loncaric, “A survey of shape analysis techniques,” *Pattern recognition*, vol. 31, no. 8, pp. 983–1001, 1998.

[66] http://www.angusj.com/delphi/clipper/documentation/Docs/Overview/_Body.htm, [Online; accessed 11-May-2015].

[67] B. R. Vatti, “A generic solution to polygon clipping,” *Communications of the ACM*, vol. 35, no. 7, pp. 56–63, 1992.

[68] J. Kowalczuk, A. Meyer, J. Carlson, E. T. Psota, S. Buettner, L. C. Pérez, S. M. Farritor, and D. Oleynikov, “Real-time three-dimensional soft tissue reconstruction for laparoscopic surgery,” *Surgical endoscopy*, vol. 26, no. 12, pp. 3413–3417, 2012.

[69] R. Szeliski, “Image mosaicing for tele-reality applications,” in *Proceedings of the Second IEEE Workshop on Applications of Computer Vision.* IEEE, 1994, pp. 44–53.

[70] E. J. Seibel, R. E. Carroll, J. Dominitz, R. S. Johnston, C. D. Melville, C. M. Lee, S. M. Seitz, M. B. Kimmey *et al.*, “Tethered capsule endoscopy, a low-cost and high-performance alternative technology for the screening of esophageal cancer and barrett’s esophagus,” *IEEE Transactions on Biomedical Engineering*, vol. 55, no. 3, pp. 1032–1042, 2008.

[71] T. D. Soper, M. P. Porter, and E. J. Seibel, “Surface mosaics of the bladder reconstructed from endoscopic video for automated surveillance,” *IEEE Transactions on Biomedical Engineering*, vol. 59, no. 6, pp. 1670–1680, 2012.

[72] S. Röhl, S. Bodenstedt, S. Suwelack, H. Kenngott, B. P. Müller-Stich, R. Dillmann, and S. Speidel, “Dense gpu-enhanced surface reconstruction from stereo endoscopic images for intraoperative registration,” *Medical physics*, vol. 39, no. 3, pp. 1632–1645, 2012.

[73] R. Johnson, L. Szymanski, and S. Mills, “Hierarchical structure from motion optical flow algorithms to harvest three-dimensional features from two-dimensional neuro-endoscopic images,” *Journal of Clinical Neuroscience*, vol. 22, no. 2, pp. 378–382, 2015.

[74] Y. Gong, D. Hu, B. Hannaford, and E. J. Seibel, “Accurate three-dimensional virtual reconstruction of surgical field using calibrated trajectories of an image-guided medical robot,” *Journal of Medical Imaging*, vol. 1, no. 3, 2014.

[75] A. Telea, "An image inpainting technique based on the fast marching method," *Journal of graphics tools*, vol. 9, no. 1, pp. 23–34, 2004.

[76] "Opencv," http://www.opencv.org/, accessed: 15-November-2015.

[77] C. Zach, "Robust bundle adjustment revisited," in *Computer Vision–ECCV 2014*. Springer, 2014, pp. 772–787.

[78] E. Rublee, V. Rabaud, K. Konolige, and G. Bradski, "Orb: an efficient alternative to sift or surf," in *IEEE International Conference on Computer Vision (ICCV)*. IEEE, 2011, pp. 2564–2571.

[79] D. Hu, Y. Jiang, E. Belykh, Y. Gong, M. C. Preul, B. Hannaford, and E. J. Seibel, "Toward real-time tumor margin identification in image-guided tobotic brain tumor resection," in *SPIE Medical Imaging*. International Society for Optics and Photonics, 2017, pp. 101 350D–101 350D.

[80] S. Gioux, H. S. Choi, and J. V. Frangioni, "Image-guided surgery using invisible near-infrared light: fundamentals of clinical translation," *Molecular imaging*, vol. 9, no. 5, p. 237, 2010.

[81] E. Belykh, N. L. Martirosyan, K. Yagmurlu, E. J. Miller, J. M. Eschbacher, M. Izadyyazdanabadi, L. A. Bardonova, V. A. Byvaltsev, P. Nakaji, and M. C. Preul, "Intraoperative fluorescence imaging for personalized brain tumor resection: Current state and future directions," *Frontiers in Surgery*, vol. 3, 2016.

[82] W. Stummer, U. Pichlmeier, T. Meinel, O. D. Wiestler, F. Zanella, H.-J. Reulen, A.-G. S. Group *et al.*, "Fluorescence-guided surgery with 5-aminolevulinic acid for resection of malignant glioma: a randomised controlled multicentre phase iii trial," *The lancet oncology*, vol. 7, no. 5, pp. 392–401, 2006.

[83] P. Schucht, S. Knittel, J. Slotboom, K. Seidel, M. Murek, A. Jilch, A. Raabe, and J. Beck, "5-ala complete resections go beyond mr contrast enhancement: shift corrected volumetric analysis of the extent of resection in surgery for glioblastoma," *Acta neurochirurgica*, vol. 156, no. 2, pp. 305–312, 2014.

[84] N. L. Martirosyan, D. D. Cavalcanti, J. M. Eschbacher, P. M. Delaney, A. C. Scheck, M. G. Abdelwahab, P. Nakaji, R. F. Spetzler, and M. C. Preul, "Use of in vivo near-infrared laser confocal endomicroscopy with indocyanine green to detect the boundary of infiltrative tumor: Laboratory investigation," *Journal of neurosurgery*, vol. 115, no. 6, pp. 1131–1138, 2011.

[85] C. Yang, V. W. Hou, E. J. Girard, L. Y. Nelson, and E. J. Seibel, “Target-to-background enhancement in multispectral endoscopy with background autofluorescence mitigation for quantitative molecular imaging,” *Journal of biomedical optics*, vol. 19, no. 7, pp. 076 014–076 014, 2014.

[86] M. A. Balafar, A. R. Ramli, M. I. Saripan, and S. Mashohor, “Review of brain mri image segmentation methods,” *Artificial Intelligence Review*, vol. 33, no. 3, pp. 261–274, 2010.

[87] T. H. Lee, M. F. A. Fauzi, and R. Komiya, “Segmentation of ct brain images using unsupervised clusterings,” *Journal of visualization*, vol. 12, no. 2, pp. 131–138, 2009.

[88] T. F. Chan and L. A. Vese, “Active contours without edges,” *IEEE Transactions on image processing*, vol. 10, no. 2, pp. 266–277, 2001.

[89] D. Mumford and J. Shah, “Optimal approximations by piecewise smooth functions and associated variational problems,” *Communications on pure and applied mathematics*, vol. 42, no. 5, pp. 577–685, 1989.

[90] J.-M. Morel and S. Solimini, *Variational methods in image segmentation: with seven image processing experiments.* Springer Science & Business Media, 2012, vol. 14.

[91] S. Osher and J. A. Sethian, “Fronts propagating with curvature-dependent speed: algorithms based on hamilton-jacobi formulations,” *Journal of computational physics*, vol. 79, no. 1, pp. 12–49, 1988.

[92] B. P. Joshi, X. Duan, R. S. Kwon, C. Piraka, B. J. Elmunzer, S. Lu, E. F. Rabinsky, D. G. Beer, H. D. Appelman, S. R. Owens *et al.*, “Multimodal endoscope can quantify wide-field fluorescence detection of barretts neoplasia,” *Endoscopy*, vol. 48, no. 02, pp. A1–A13, 2016.

[93] K. I. Swanson, P. A. Clark, R. R. Zhang, I. K. Kandela, M. Farhoud, J. P. Weichert, and J. S. Kuo, “Fluorescent cancer-selective alkylphosphocholine analogs for intraoperative glioma detection,” *Neurosurgery*, vol. 76, no. 2, p. 115, 2015.

[94] P. A. V. QUEVEDO, “5-aminolevulinic-induced protoporphyrin ix fluorescence as an intraoperative biomarker for brain tumors: Detection methods and biological correlates,” Ph.D. dissertation, Dartmouth College Hanover, New Hampshire, 2011.

[95] F. L. Bookstein, “Principal warps: Thin-plate splines and the decomposition of deformations,” *IEEE Transactions on Pattern Analysis & Machine Intelligence*, no. 6, pp. 567–585, 1989.

[96] S. Roberts and L. Stals, "Discrete thin plate spline smoothing in 3d," *ANZIAM Journal*, vol. 45, pp. 646–659, 2004.

[97] S. N. Wood, "Thin plate regression splines," *Journal of the Royal Statistical Society: Series B (Statistical Methodology)*, vol. 65, no. 1, pp. 95–114, 2003.

[98] "Eigen," http://eigen.tuxfamily.org/, accessed: 15-November-2015.

[99] "Robot operating system," http://www.ros.org/, accessed: 15-November-2015.

[100] I. L. Yeoh, P. G. Reinhall, M. C. Berg, H. J. Chizeck, and E. J. Seibel, "Electromechanical modeling and adaptive feedforward control of a self-sensing scanning fiber endoscope," *Journal of Dynamic Systems, Measurement, and Control*, vol. 138, no. 10, p. 101006, 2016.

[101] L. Zhang, A. S. Kim, J. S. Ridge, L. Y. Nelson, J. H. Berg, and E. J. Seibel, "Trimodal detection of early childhood caries using laser light scanning and fluorescence spectroscopy: clinical prototype," *Journal of biomedical optics*, vol. 18, no. 11, pp. 111 412–111 412, 2013.

[102] I. N. Figueiredo, S. Kumar, C. Leal, and P. N. Figueiredo, "An automatic blood detection algorithm for wireless capsule endoscopy images," *Computational Vision and Medical Image Processing IV: VIPIMAGE*, vol. 2013, pp. 237–241, 2013.

[103] V. Duindam and S. Sastry, "Geometric motion estimation and control for robotic-assisted beating-heart surgery," in *IEEE/RSJ International Conference on Intelligent Robots and Systems (IROS)*. IEEE, 2007, pp. 871–876.

[104] S. G. Yuen, D. T. Kettler, P. M. Novotny, R. D. Plowes, and R. D. Howe, "Robotic motion compensation for beating heart intracardiac surgery," *The International journal of robotics research*, vol. 28, no. 10, pp. 1355–1372, 2009.

[105] G. C. Sharp, S. B. Jiang, S. Shimizu, and H. Shirato, "Prediction of respiratory tumour motion for real-time image-guided radiotherapy," *Physics in medicine and biology*, vol. 49, no. 3, p. 425, 2004.

[106] J. Czajkowska, B. Pycinski, and E. Pietka, "Hog feature based detection of tissue deformations in ultrasound data," in *2015 37th Annual International Conference of the IEEE Engineering in Medicine and Biology Society (EMBC)*. IEEE, 2015, pp. 6326–6329.

[107] C. Otte, G. Hüttmann, and A. Schlaefer, “Feasibiliy of optical detection of soft tissue deformation during needle insertion,” in *SPIE Medical Imaging*. International Society for Optics and Photonics, 2012, pp. 83 160V–83 160V.

[108] H. Courtecuisse, H. Jung, J. Allard, C. Duriez, D. Y. Lee, and S. Cotin, “Gpu-based real-time soft tissue deformation with cutting and haptic feedback,” *Progress in biophysics and molecular biology*, vol. 103, no. 2, pp. 159–168, 2010.

[109] M. Stamatelatos, “Probabilistic Risk Assessment: What Is It And Why Is It Worth Performing It?” https://www.hq.nasa.gov/office/codeq/qnews/pra.pdf, 2000, [Online; accessed 11-May-2017].

[110] J. Wreathall and C. Nemeth, “Assessing risk: the role of probabilistic risk assessment (pra) in patient safety improvement,” *Quality and Safety in Health Care*, vol. 13, no. 3, pp. 206–212, 2004.

[111] W. Korb, M. Kornfeld, W. Birkfellner, R. Boesecke, M. Figl, M. Fuerst, J. Kettenbach, A. Vogler, S. Hassfeld, and G. Kornreif, “Risk analysis and safety assessment in surgical robotics: A case study on a biopsy robot,” *Minimally Invasive Therapy & Allied Technologies*, vol. 14, no. 1, pp. 23–31, 2005.

[112] B. Hannaford, D. Hu, D. Zhang, and Y. Li, “Simulation results on selector adaptation in behavior trees,” *arXiv preprint arXiv:1606.09219*, 2016.

[113] J. J. Abbott, P. Marayong, and A. M. Okamura, “Haptic virtual fixtures for robot-assisted manipulation,” in *Robotics research*. Springer, 2007, pp. 49–64.

[114] T. Yamamoto, N. Abolhassani, S. Jung, A. M. Okamura, and T. N. Judkins, “Augmented reality and haptic interfaces for robot-assisted surgery,” *The International Journal of Medical Robotics and Computer Assisted Surgery*, vol. 8, no. 1, pp. 45–56, 2012.

[115] Y. Kobayashi, P. Moreira, C. Liu, P. Poignet, N. Zemiti, and M. G. Fujie, “Haptic feedback control in medical robots through fractional viscoelastic tissue model,” in *Engineering in Medicine and Biology Society, EMBC, 2011 Annual International Conference of the IEEE*. IEEE, 2011, pp. 6704–6708.

[116] K. Sangpradit, H. Liu, P. Dasgupta, K. Althoefer, and L. D. Seneviratne, “Finite-element modeling of soft tissue rolling indentation,” *IEEE Transactions on Biomedical Engineering*, vol. 58, no. 12, pp. 3319–3327, 2011.

[117] M. Beccani, C. Di Natali, L. J. Sliker, J. A. Schoen, M. E. Rentschler, and P. Valdastri, "Wireless tissue palpation for intraoperative detection of lumps in the soft tissue," *IEEE Transactions on Biomedical Engineering*, vol. 61, no. 2, pp. 353–361, 2014.

[118] D.-H. Lee, U. Kim, T. Gulrez, W. J. Yoon, B. Hannaford, and H. R. Choi, "A laparoscopic grasping tool with force sensing capability," *IEEE/ASME Transactions on Mechatronics*, vol. 21, no. 1, pp. 130–141, 2016.

[119] F. E. Shelton IV, J. N. Ouwerkerk, J. R. Morgan, and J. S. Swayze, "Surgical instrument with force-feedback capabilities," Apr. 17 2012, uS Patent 8,157,153.

[120] K. G. Baum, M. Helguera, J. P. Hornak, J. P. Kerekes, E. D. Montag, M. Z. Unlu, D. H. Feiglin, and A. Krol, "Techniques for fusion of multimodal images: Application to breast imaging," in *Image Processing, 2006 IEEE International Conference on.* IEEE, 2006, pp. 2521–2524.

[121] T. Bonaci, J. Herron, T. Yusuf, J. Yan, T. Kohno, and H. J. Chizeck, "To make a robot secure: An experimental analysis of cyber security threats against teleoperated surgical robots," *arXiv preprint arXiv:1504.04339*, 2015.

[122] A. P. James and B. V. Dasarathy, "Medical image fusion: A survey of the state of the art," *Information Fusion*, vol. 19, pp. 4–19, 2014.

Appendix A

AREA OF POLYGONS FROM GREEN'S THEOREM

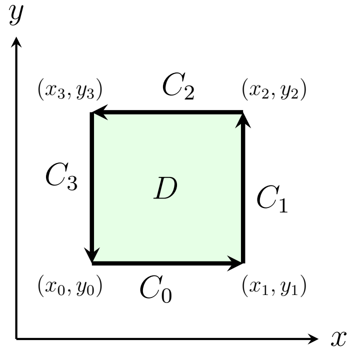

Figure A.1: Example of a polygon on a plane (number of vertices n = 4)

Let C be a count-clockwise oriented, piecewise smooth, simple closed curve in a plane, and let D be the region bounded by C (see Figure A.1), Green's Theorem gives the relationship between a line integral around C and a double integral over D as below:

$$\oint_{\boldsymbol{C}} L\,dx + M\,dy = \iint_{\boldsymbol{D}} (\frac{\partial M}{\partial x} - \frac{\partial L}{\partial y})\,dx\,dy \tag{A.1}$$

where the path of integration along C is counter-clockwise. L and M are functions of (x, y) defined in the region D and have continuous partial derivatives there.

Green's theorem can be used to calculate the area of region D by letting $\frac{\partial L}{\partial y} - \frac{\partial M}{\partial x} = 1$, as given in Equation A.2.

$$A = \iint_{\boldsymbol{D}} dx\,dy = \oint_{\boldsymbol{C}} L\,dx + M\,dy \tag{A.2}$$

such function L and M can be chosen as $L = 0$, and $M = x$. Equation A.2 can be further simplified as:

$$A = \oint_{\boldsymbol{C}} M\,dy = \oint_{\boldsymbol{C}} x\,dy = \int_{\boldsymbol{C_0}} x\,dy + \int_{\boldsymbol{C_1}} x\,dy + ... + \int_{\boldsymbol{C_{n-1}}} x\,dy \tag{A.3}$$

where $C = C_0 \cup C_1 \cup ... \cup C_{n-1}$.

Considering a polygon consisting of a set of 2D points in form $[(x_0, y_0), ..., (x_k, y_k), ..., (x_{n-1}, y_{n-1})]$, the line function C_k is defined as:

$$C_k = ((x_{k+1} - x_k)t + x_k, (y_{k+1} - y_k)t + y_k), \quad 0 \leq t \leq 1 \tag{A.4}$$

Therefore,

$$\int_{\boldsymbol{C_k}} x\,dy = \int_0^1 ((x_{k+1} - x_k)t + x_k)(y_{k+1} - y_k)\,dt = \frac{1}{2}(x_{k+1} + x_k)(y_{k+1} - y_k) \tag{A.5}$$

Substituting Equation A.5 into Equation A.3. we get the area of polygon D as:

$$A = \sum_{k=0}^{n-1} \frac{(x_{k+1} + x_k)(y_{k+1} - y_k)}{2} \tag{A.6}$$

VITA

Danying Hu was born and raised in Ningbo, China. She earned her B.Eng. degree in Mechatronics from Tongji University, Shanghai, China in 2008 and her M.Sc. degree in Mechanical Engineering from RWTH Aachen University, Germany in 2012. In Autumn 2012, she joined the BioRobotics Laboratory at the University of Washington, where she was advised by Prof. Blake Hannaford. In 2017 she earned a Ph.D. degree in Electrical Engineering from the University of Washington.